学位論文

Irradiation processes in the early solar system:
A multiple isotope study on early solar system solids

（太陽系初期の固体物質に対するマルチ同位体分析から読み解く初期太陽系における宇宙線照射過程）

平成 29 年 12 月博士（理学）申請

東京大学大学院理学系研究科

地球惑星科学専攻

福田航平

Abstract

In the present work, I conducted isotopic studies on early solar system solids, Calcium-Aluminum-rich Inclusions (CAIs) and chondrules, in primitive meteorites and discussed the earliest history of the solar system formation. In particular, my study focused on the origin and distribution of a short-lived radionuclide ^{10}Be in the early solar system.

Berrylium-10 is a unique short-lived radionuclide because it cannot be produced by thermonuclear reactions in stars, but by spallation reactions of the solar system materials with energetic particles. The stable isotopes of Li, Be, and B are also made by spallation processes, and the isotopic compositions of these elements are strongly energy dependent. Therefore, Li-Be-B isotopic systematics of meteoritic components would provide important constraints on the spallation-related processes in the early solar system.

Up to now, however, the origin of ^{10}Be in the early solar system is not well understood. A plausible candidate for the origin of ^{10}Be is irradiation by cosmic rays from the early active Sun. This is because the available ^{10}Be abundances recorded in CAIs, which are the oldest known solids in our solar system, appear to show some heterogeneities. The variation in ^{10}Be abundances in CAIs may reflect various irradiation conditions, such as irradiation target compositions, energetic particle fluxes, irradiation time, irradiation distance from the proto-Sun. However, an accurate measurement of ^{10}Be abundances by Secondary Ion Mass Spectrometry (SIMS) is difficult without a suitable and matrix-matched standard materials for the Be/B analysis. Most of previous studies used silica-rich glasses for the Be-B measurements of melilite in CAIs, because suitable standards for melilite are not available in natural terrestrial environments. This could lead to systematic errors on ^{9}Be/^{11}B ratios of melilite and their ^{10}Be abundances. Thus, variations in ^{10}Be/^{9}Be ratios of CAIs may come from analytical artifacts by SIMS measurements. Furthermore, most of Be-B data thus far have been from the relatively

large CAIs in CV chondrites. To discuss the origin and distribution of ^{10}Be, it is important to investigate Be-B systematics in various types of meteoritic components, including small CAIs and chondrules in various types of meteorites.

Chondrules are the dominant constituent of most primitive meteorites, which also formed at the earliest stage of the solar system formation. Because chondrules show different textual, chemical, and isotopic compositions from those of CAIs, they would have information about different time and/or location in the solar protoplanetary disk. Thus, investigations of ^{10}Be abundances in chondrules would shed light on the distribution of ^{10}Be in the early solar system. Up to now, however, because sizes of minerals composed of chondrules are relatively small, it has not been successful to conduct the Be-B isotope measurements for chondrules.

To overcome this problem, I developed a protocol for high-spatial-resolution Be-B measurement using a NanoSIMS 50. In addition, I synthesized melilitic and anorthitic glass-standards doped with Be and B, and investigate Be/B relative sensitivity factors for different matrix compositions. Using the high-spatial and high-accuracy SIMS technique, I have performed the Be-B analyses of CAIs in four carbonaceous chondrites, Y81020 (CO3.05), Y82094 (ungrouped C3.2), SaU290 (CH3) and Isheyevo (CH/CBb) with a NanoSIMS 50. The CAIs in various types of chondrites studied here show high and variable initial ^{10}Be/^{9}Be ratios ((~1.7 to 40.5) × 10^{-4}) than previously thought. This result strongly suggests that ^{10}Be was produced by protosolar cosmic ray irradiation. I also measured Li isotopic compositions of these CAIs and found that the Li isotopic compositions of these CAIs are nearly chondritic independent of their ^{10}Be/^{9}Be ratios. This can be best explained if the targets of cosmic ray irradiation had the chondritic compositions: in other words, targets were most likely not CAI themselves, but their precursors of solar gases. Several astronomical observations of solar analogs demonstrated that X-ray emissions from protostars with the earliest evolutional stage are high and variable. The variable ^{10}Be/^{9}Be ratios observed in this study may reflect the

variable and extreme irradiation by cosmic rays from the earliest evolutional stage of the proto-Sun. Further, I have investigated Al-Mg systematics on CH CAIs with high and variable $^{10}Be/^{9}Be$ ratios. All CAIs studied here show no resolvable excesses in ^{26}Mg. Considering the degree of variations in $^{10}Be/^{9}Be$ between CV CAIs and CH CAIs, the incorporation of ^{26}Al in the early solar system would occur within ~1 Myr at the birth of our solar system.

Then I have expanded the Be-B study to chondrules in the Y82094 carbonaceous chondrite. I found evidence for live ^{10}Be at the time of chondrule formation, strongly suggesting the widespread distribution of ^{10}Be in the solar protoplanetary disk. The inferred initial $^{10}Be/^{9}Be$ ratio is $(1.92 \pm 0.45) \times 10^{-3}$ (2σ), which is higher than those of CAIs in CV chondrites ($< 1.2 \times 10^{-3}$). This result can be interpreted as further evidence that ^{10}Be was produced by solar cosmic ray irradiation. Initial $^{10}B/^{11}B$ ratio and Li isotopic ratios of the chondrules are similar to the chondritic compositions, suggesting that ^{10}Be was produced by irradiation of a solar nebular gas. The high $^{10}Be/^{9}Be$ ratio observed in chondrules indicates that Y82094 chondrules might have formed very early, before significant decay of ^{10}Be, possibly contemporaneously with CAIs.

Acknowledgements

I wish to appreciate associate Prof. H. Hiyagon, my supervisor of the University of Tokyo, and research associate W. Fujiya of Ibaraki University for their supports during my doctoral course. Without their exact advices, suggestions and patient helps, I could not achieve the doctoral dissertation.

I am grateful to Prof. Y. Sano, research associates N. Takahata and T. Kagoshima of Atmosphere and Ocean Research Institute, The University of Tokyo for their assistance in NanoSIMS analyses and important comments.

I sincerely thank associate Prof. T. Mikouchi and associate Prof. T. Iizuka of The University of Tokyo for significant discussions in our cosmic and earth material science seminar. I am also thank their kind supports for my mental side. When my research was not going well, they always encouraged me.

I wish to appreciate K. Ichimura for production of analytical standards necessary for the present work, and his assistance in FE-EPMA observations. I thank H. Yoshida for his assistance in FE-EPMA analyses.

I thank A. Takenouchi and M. Koike, my colleagues for their emotional assistance and friendship. I am also grateful H. Hasegawa, A. Hayakawa, and H. Ohno, my junior colleagues for their friendship.

Finally, I deeply thank my father, Koichi, my mother, Fumiyo, my sisters, Nana and Mei, and my fiancée, Makiko. Their sincere supports have always encouraged me.

CONTENTS

CHAPTER 1: General introduction

The present study focuses on the origin of the short-lived radionuclide ^{10}Be in the early solar system and earliest evolution of the solar protoplanetary disk. In particular, I investigated distribution of the short-lived radionuclide ^{10}Be in the early solar system by use of the ^{10}Be-^{10}B system for CAIs and chondrules, and discuss plausible origins of ^{10}Be in the early solar system from Li-Be-B and Al-Mg systematics of CAIs and chondrules. As the general introduction, here I briefly review the evolutional time scale of the protoplanetary disk. I also introduce the current view of the distribution of ^{26}Al and ^{10}Be in the early solar system based on information derived from meteoritic studies. In addition, I point out the problems in ^{10}Be-^{10}B measurements for meteoritic components, which will be discussed in more detail in the following chapters.

1.1. Formation and evolution of the protoplanetary disk

A planetary system, a central star-protoplanetary disk system, forms in the interstellar medium from gravitational collapse of a dense fragment of a (giant) molecular cloud. The central star started to shine due to release of the gravitational energy, and then due to release of the nuclear energy in the Main Sequence of the star evolution. The protoplanetary disk consists of gas and fine dust grains, where these components eventually evolve to planets. Our solar system is now thought to be born and evolved through the following processes. In this case, understanding of the evolution of the protoplanetary disk is highly important to reveal the origin and evolution of planets in our solar system

Recent astronomical observations of young stellar objects (YSOs) revealed a time scale of the evolution of the planetary system. According to the spectral energy distribution (SED), YSOs are classified into four stages (class 0/I/II/III) that reflect conditions of infalling clouds and circumstellar disk (e.g., Boss and Ciesla, 2014). Class 0 corresponds to a protostar deeply embedded in the circumstellar material and envelope. Class I corresponds to a protostar, which has a more diffuse circumstellar envelope and a slower infall rate. Class II corresponds to classical T Tauri stars, which are surrounded by an accretion disk consisting of gases and fine dust grains. Class III is characterized by the dissipation of the disk essentially due to the winds emitted from the forming star and planetary growth. Evans et al. (2009) estimated the lifetime of individual classes of YSOs, based on observations of five large molecular clouds. They proposed that the class 0, class I, and class II stages last roughly 0.04-0.3 Myr, 0.2-0.6 Myr, and 0.6-3 Myr, respectively. Considering that a duration of the class III stage is on the order of a few Myr (Winston et al., 2009), a time scale of the evolution of the planetary system would be ~10 Myr, which is dramatically shorter than the age of our solar system (~4.6 Ga: Amelin et al., 2010).

1.2. Properties of the first solids in the solar system

Meteorites are extraterrestrial rocks, which are thought to be fragments resulting from collisions of various solar system objects. Based on their bulk compositions and textures, meteorites can be divided into two major categories, chondrites and non-chondritic meteorites (Scott and Krot, 2014). The former are thought to be asteroidal sediments made of components with very different origins (from high temperature minerals to volatile element-rich low temperature minerals) and their parent bodies have not undergone melting nor differentiation after their accretion. Therefore, chondritic components should preserve physicochemical processes in the solar protoplanetary disk (hereafter protosolar disk) before the accretion into their parent bodies.

Chondrites consist of four major components: refractory inclusions (Ca-Al-rich inclusions (CAIs) and amoeboid olivine aggregates (AOAs)), chondrules, FeNi-metal (with some sulfide grains), and fine-grained matrix material. CAIs are the oldest known solids in our solar system as indicated by their absolute radiometric U-Pb ages (Amelin et al., 2010). Non-altered CAIs are composed of corundum (Al_2O_3), hibonite ($CaAl_{12}O_{19}$), grossite ($CaAl_4O_7$), perovskite ($CaTiO_3$), melilite ($Ca_2(Al_2, MgSi)SiO_7$), spinel ($FeMg(Cr, Al, Ti)_3O_4$), anorthite ($CaAl_2Si_2O_8$), etc., that are rich in Ca and Al (MacPerson, 2014 and reference therein). Such minerals compositions well match with what is predicted for the earliest condensates from a cooling gas of solar composition at temperatures > 1300 K and total pressure of 10^{-5} to 10^{-3} bars (e.g., Ebel and Grossman, 2000). This is consistent with the fact that CAIs show the oldest ages among the solar system materials. Some CAIs are thought to be condensates because they have irregular shapes, fluffy textures, and group II rare earth element patterns that can be produced by a condensation from fractionated solar gas (e.g., Grossman, 1975; Simon et al., 2002; Hiyagon et al., 2011). On the other hand, other CAIs have been thermally processed and were probably once molten. Thus, it should be considered that their chemical and isotopic signatures

correspond to information when and/or where the CAIs formed in the protosolar disk. Although CAIs might have experienced much more complicated histories (condensation and/or evaporation), understanding of their formation conditions is a key to unravel the astrophysical conditions in the nascent solar system.

Chondrules are the major constituents of most of primitive meteorites, chondrites. They are submillimeter to millimeter-sized igneous spherules and are mostly composed of olivine, pyroxene, mesostasis, and/or opaque assemblages (Fe, Ni-metal, sulfides). Pb-Pb isotopic measurements of individual chondrules demonstrated that chondrule formation started contemporaneously with the CV CAIs at 4567.61 ± 0.54 My and lasted for ~4 My (Connelly et al., 2012; Bollard et al., 2017). Chondrules show a wide variety of textures (porphyritic, granular, barred, radial, cryptocrystalline) and chemical compositions (FeO-poor, FeO-rich, and Al-rich), which provide important constraints on the earliest transient heating events that melted solids in the protosolar disk (e.g., Jones, 2012). Despite their ubiquity, their formation process, certainly an important astrophysical process in the early solar system, is still largely shrouded in mystery. Candidate mechanisms, such as gas-liquid condensation (e.g., Blander et al., 2004), radiative heating and melting of dustballs brought by disk accretion to the inner edge of the disk (X-wind model: Shu et al., 1997), shock waves in the protoplanetary disk with different scale and nature (e.g., Desch et al., 2005), magnetized turbulence in the protoplanetary disk (McNally et al., 2013), and collisions between primitive or differentiated planetesimals (e.g., Krot et al., 2005; Asphaug et al., 2011: Johnson et al., 2015) are actively debated.

Regarding textural characteristics, chondrules are divided into two types: porphyritic, which have large crystals of olivine and/or pyroxene in a fine-grained or glassy mesostasis, and non-porphyritic, which include those with cryptocrystalline, radial pyroxene, and barred-olivine textures (see detailed in Scott and Krot, 2014). Porphyritic chondrules are classified into type I, which are FeO-poor, and Type II, which are FeO-

rich. Type I chondrules consist of large (20-150 μm) FeO-poor olivine crystals embedded in mesostasis or poikilitically enclosed in large euhedral low-Ca pyroxene phenocrysts. These differences in chemical composition may reflect different formation conditions, such as precursor materials and oxygen fugacity of their formation region (e.g., Tenner et al., 2015). Recent high precision O, Mg, Ti, and Cr isotopic measurements of chondrules revealed that chondrules show distinct isotopic signatures among their host chondrite groups (Kita et al., 2016; Olsen et al., 2016; Van Kooten et al., 2016; Gerber et al., 2017). These textural, chemical, and isotopic variations among chondrules strongly suggest that they are samples from various regions in the protosolar disk. In other words, chondrules should record physicochemical information about various regions in the protosolar disk.

1.3. Short-lived radionuclides in the early solar system

Meteorites and their components show evidence for the presence of now-extinct short-lived radionuclides (e.g., ^{10}Be, ^{26}Al, ^{41}Ca, ^{53}Mn, ^{60}Fe, ^{129}I, and ^{182}Hf) during the earliest stage of the solar system evolution. Because these nuclides can be synthesized under limited astrophysical environments, the presence of short-lived radionuclides (hereafter SLRs) would provide important constraints on the environment of the solar system formation. However, the origins of SLRs in the early solar system still remain controversial. From theoretical viewpoints, most of SLRs are believed to be originated from stellar processes and were either inherited from the ambient interstellar medium or injected into the protosolar disk (Davis and McKeegan, 2014 and reference therein). Another possibility is that they are produced by nuclear reactions induced by energetic charged particles bombarding ambient gas or dust near the proto-Sun (e.g., Lee et al., 1998; Gounelle et al., 2001, 2006).

Because of their short half-lives (< 100Myr), SLRs potentially serve as

chronometers with high time resolution capable of distinguishing the short time differences between events in the earliest solar system. It should be noted, however, that the applicability of SLRs for the early solar system chronology relies on the homogeneous distribution of both parent and daughter isotopes in the protosolar disk. The extent of the isotopic homogeneity depends on the origin of these SLRs. Thus, it is important to understand the origin of SLRs in the early solar system for using SLRs as a chronometer.

1.4. Al-Mg isotopic compositions of CAIs and chondrules

The ^{26}Al-^{26}Mg decay system with a half-life of 0.705 Ma (Nishiizumi, 2004) is the most widely studied chronometer for understanding the formation and evolution of the protosolar disk (Kita et al., 2013 and reference therein). From theoretical viewpoints, ^{26}Al could come into the forming solar system as a stellar product from a dying star, such as supernova, asymptotic giant branch star, or Wolf-Rayet star (Huss et al., 2009; Wasserburg et al., 2006; Arnould et al., 2006). Jacobsen et al. (2008) conducted high precision Al-Mg isotopic analyses of CAIs in CV chondrites and determined the initial ^{26}Al/^{27}Al ratio for bulk CAIs (^{26}Al/^{27}Al = 5.23 × 10^{-5}). As mentioned above, CAIs show the oldest age among the solar system materials (4567.18 ± 0.50 Ma: Amelin et al., 2010). Thus, the ^{26}Al/^{27}Al ratio of CV CAIs is thought to be the initial ratio at the birth of the solar system (so-called 'canonical value'). MacPherson et al. (2012, 2017) reported initial ^{26}Al/^{27}Al ratios of CV CAIs (^{26}Al/^{27}Al = 4.17 to 5.3 × 10^{-5}) defined by internal isochrons and revealed that CV CAIs continued to be reprocessed over ~ 0.7 Ma. CAIs in other primitive chondrites (Yamato 81020 (CO3.05) and Acfer 094 (ungrouped C3.0)) also show nearly canonical ^{26}Al/^{27}Al ratios (^{26}Al/^{27}Al = 4.08 to 5.32 × 10^{-5}; Ushikubo et al., 2017), indicating their short formation duration of less than 1My after the birth of the solar system.

In contrast to the results of CAIs in CV, CO, and ungrouped C chondrites, CAIs in CH chondrites do not show resolvable excesses in ^{26}Mg (Kimura et al., 1992; Weber et al., 1995; Krot et al., 2008a). As will be described in chapter 3, CH CAIs composed mainly of grossite, hibonite, and gehlenitic melilite, which are condensed from the solar nebular at relatively high temperatures (1400 to 1800 K). Because of their highly refractory nature, Krot et al. (2008a) suggests that ^{26}Al-poor CH CAIs formed prior to incorporation and homogenization of ^{26}Al into the solar system. In addition, hibonite-rich inclusions with large isotopic anomalies in ^{48}Ca (and ^{50}Ti) in CM chondrites also show no resolvable excesses in ^{26}Mg (e.g., Fahey et al., 1987; Ireland, 1988; Liu et al., 2009; Kööp et al., 2016). Generally speaking, the degree of isotopic heterogeneity in the protosolar disk would become suppressed in the evolved disk due to thermal processing within the disk. If this is the case, the correlation between lack of resolvable excesses in ^{26}Mg and large isotopic anomalies suggests that ^{26}Al-poor CAIs formed at the earliest stage of the protosolar disk evolution.

There is a minor group of CAIs, which are distinguished from 'normal' CAIs solely by their isotopic characteristics. They are so called FUN (*F*ractionation and *U*nidentified *N*uclear effects) CAIs, which show large mass-dependent fractionation in O, Mg, and Si preferring heavier isotopes (*F*-signature) and mass-independent isotopic anomalies, especially, positive or negative anomalies in ^{48}Ca, ^{50}Ti, and ^{54}Cr (*UN*-signature) (Krot et al., 2014 and reference therein). It is also known that excesses in ^{26}Mg from the decay of ^{26}Al are significantly lower in FUN CAIs than those of normal CAIs (Park et al., 2017 and reference therein). Therefore, as mentioned in the case of hibonite-rich inclusions, these observations also suggest that ^{26}Al-poor CAIs formed before completion of isotopic homogenization in the protosolar disk, possibly during the earliest stage of the evolution of the protosolar disk (e.g., Sahijpal and Goswami, 1998; Sahijpal et al., 2000; Krot et al., 2009; Kööp et al., 2017; Park et al., 2017). Hence, from the viewpoint of Al-Mg systematics with stable isotopic compositions in CAIs, there may be

multiple generations of CAIs formed in the protosolar disk.

Evidence for live ^{26}Al has been also observed in chondrules (e.g., Kita et al., 2000) and differentiated meteorites (e.g., Srinivasan et al., 1999; Schiller et al., 2015), suggesting that ^{26}Al was widely distributed in the protosolar disk. Initial ^{26}Al/^{27}Al ratios of chondrules are more than a few times lower than those of the canonical value (^{26}Al/^{27}Al = 5.23×10^{-5}). As discussed by Kita and Ushikubo (2012) and Nagashima et al. (2017), there is a spread in the initial ^{26}Al/^{27}Al ratios among chondrite groups as well as within each chondrite group (Fig. 1.1). These datasets show that initial ^{26}Al/^{27}Al ratios of chondrules in ordinary, CO, CV, and ungrouped C3.0 (Acfer 094) are systematically higher than those of chondrules in CR and CH chondrules. The differences in initial ^{26}Al/^{27}Al ratios of chondrules among various chondrite groups suggest that there are samples that have originated from various formation times and/or formation regions in the protosolar disk.

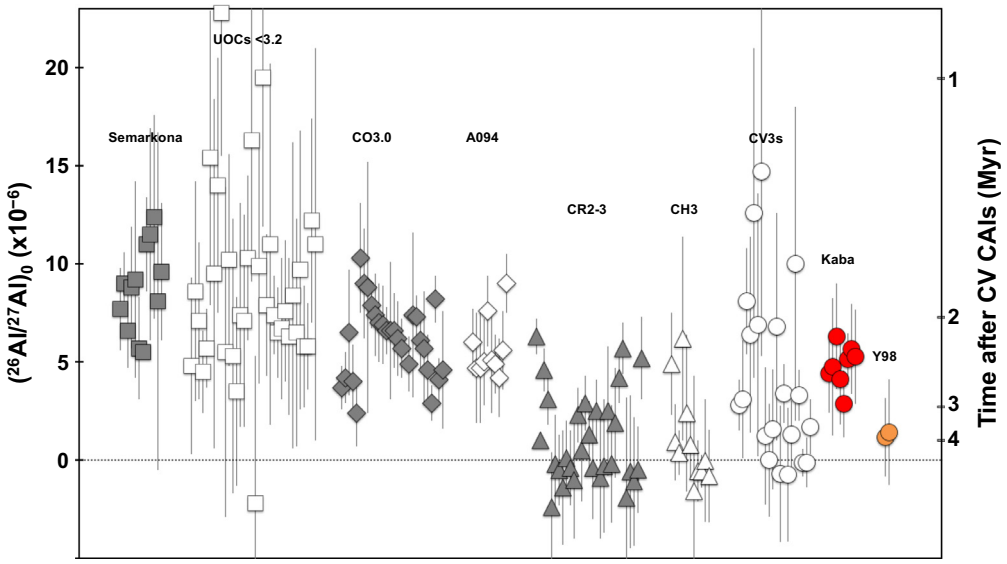

Fig. 1.1. $(^{26}Al/^{27}Al)_0$ in chondrules from unequilibrated ordinary chondrites (UOCs) and carbonaceous chondrites. Also shown are ages of the chondrules relative to that of the CV CAIs calculated by assuming the homogenous distribution of ^{26}Al in the protosolar disk. After Nagashima et al. (2017).

1.5. Be-B isotopic compositions of CAIs and chondrules

Berrylium-10, which decays to ^{10}B with a half-life of 1.39 Myr (Korschinek et al., 2010), is a unique SLR because it cannot be produced by thermonuclear reactions in stars, but by energetic particle spallation reactions (e.g., Fowler et al., 1961). The existence of ^{10}Be in the early solar system was first demonstrated by McKeegan et al. (2000). They investigated Be-B isotope systematics in CAIs in CV chondrites using secondary ion mass spectrometry (SIMS) and found a linear correlation between excesses in ^{10}B and $^{9}Be/^{11}B$ ratios in melilite crystals (Fig. 1.2). The initial $^{10}Be/^{9}Be$ ratio was found to be 9.5×10^{-4}. After the discovery, several workers have investigated Be-B systematics in CV CAIs and found the existence of variations in $^{10}Be/^{9}Be$ ratio between 1.1×10^{-4} to 12.0×10^{-4} (Sugiura et al., 2001; MacPherson et al., 2003; Chaussidon et al., 2006; Wielandt et al., 2012; Srinivasan and Chaussidon, 2013; Dunham et al., 2016, 2017; Liu et al., 2018). Up to now, very few data on ^{10}Be abundances have been reported for CAIs in other types of chondrites. Liu et al. (2010) conducted Li-Be-B isotopic measurements on hibonite grains from the CM chondrite. The initial $^{10}Be/^{9}Be$ ratio inferred from a bulk isochron is found to be $\sim 5 \times 10^{-4}$, which is in the range of initial $^{10}Be/^{9}Be$ ratios of CV CAIs. Recently, Gounelle et al. (2013) found an extremely high $^{10}Be/^{9}Be$ ratio ($^{10}Be/^{9}Be = 100 \times 10^{-4}$) recorded in the CAI 411 in Isheyevo (CH/CBb) chondrite. These observations suggest that CAIs record the variations in $^{10}Be/^{9}Be$ by as much as a factor of 100 (or a factor of 10 if the extremely high value from Gounelle et al. (2013) is excluded).

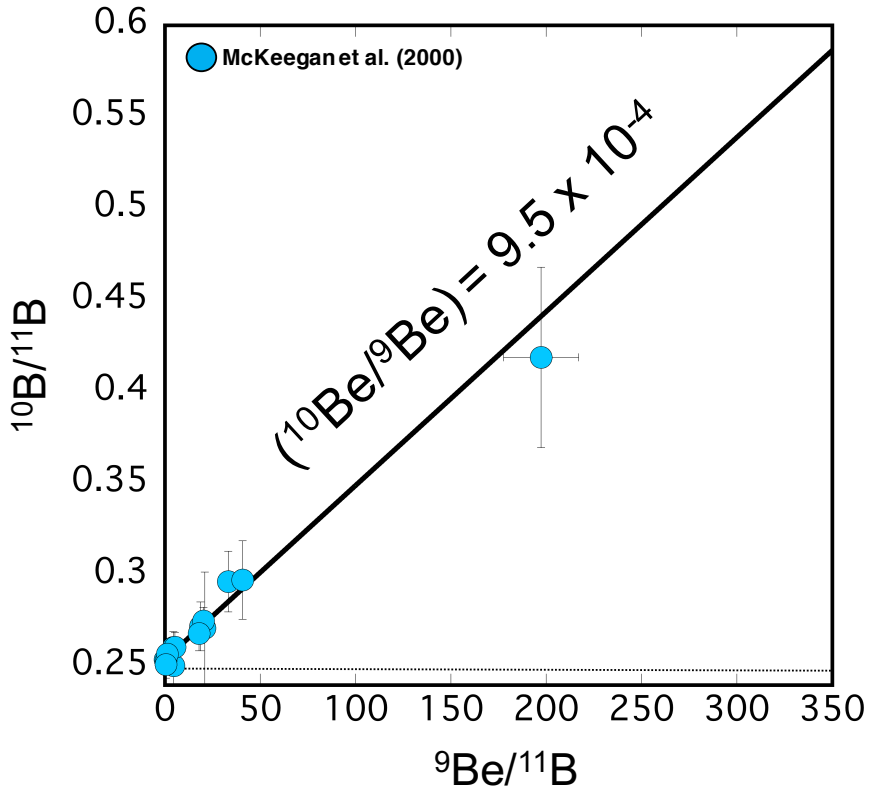

Fig. 1.2. $^{10}B/^{11}B$ vs. $^{9}Be/^{11}B$ isochron diagram for the CAIs in Allende (CV3) meteorite. Error bars are 2σ. The dashed line represents the chondritic composition ($^{10}B/^{11}B$ = 0.2481; Zhai et al., 1996). The $^{10}B/^{11}B$ values from various spots of CAIs show ^{10}B excesses that are correlated with the Be/B ratio, indicative of the in situ decay of ^{10}Be in CAIs. The solid line shows the weighted fit to the data which corresponds to an initial $^{10}Be/^{9}Be$ ratio of $(9.5 \pm 1.9) \times 10^{-4}$ (2σ) at the time of crystallization of the CAI 3529-41.

Searching for ^{10}Be in chondrules has been conducted by Sugiura (2001), but chondrules with sufficiently high $^{9}Be/^{11}B$ ratios to resolve ^{10}B excesses appear to be rare. Sugiura (2001) analyzed anorthites in chondrules from the Y82094 (ungrouped C3.2) chondrite and showed a hint for the existence of live ^{10}Be at the time chondrule formation. However, no resolvable excesses in ^{10}B at the 2σ revel were found. To really determine the ^{10}Be abundances recorded in chondrules, much higher accuracy and higher precision

are required.

Several mechanisms have been proposed for the origin of ^{10}Be in the early solar system. Desch et al. (2004) proposed the trapped galactic cosmic ray (GCR) components by presolar molecular cloud. Given a high abundance of ^{10}Be nuclei in GCRs (Be is present at levels 10^6 times solar), they consider that GCR ^{10}Be nuclei trapped in a molecular cloud could contribute significantly to the ^{10}Be abundances in meteoritic components. They suggest ^{10}Be/^{9}Be ratios of up to ~ 10×10^{-4} at the time of protostar formation, which is comparable to the highest ^{10}Be/^{9}Be ratio in CV CAIs.

Another model involving the protosolar molecular cloud was proposed by Tatischeff et al. (2014), although the details are largely different from those in Desch et al. (2004). They found that: (1) trapped GCR in the collapsing presolar molecular cloud core induced negligible ^{10}Be contamination to the protosolar nebula, (2) irradiation of the presolar molecular cloud by background GCRs produced a steady-state ^{10}Be/^{9}Be ratio $\leq$ 1.3×10^{-4} at the time of the solar system formation. They also considered irradiation of the presolar molecular cloud by freshly accelerated cosmic rays escaped from an isolated supernova remnant. This model could produce the ^{10}Be/^{9}Be ratio at a level of 3×10^{-4}, which is comparable to those recorded in FUN CAIs in the CV chondrites (Wielandt et al., 2012). Note that because the spatial scale of the molecular cloud is so much larger than that of the protosolar disk, these models predict that ^{10}Be was homogeneously distributed in the protosolar disk, which would allow ^{10}Be to be used for chronometry.

Recently, Banerjee et al. (2016) proposed that ^{10}Be was produced by a neutrino spallation process in core-collapse supernovae (CCSNe). They showed that the neutrino spallation process occurred with low-mass CCSNe can produce ^{10}Be at a level of ^{10}Be/^{9}Be ~5.2-6.4 $\times 10^{-4}$. If combining ^{10}Be produced by the neutrino spallation process and ^{10}Be produced by background GCRs (1.3×10^{-4}: Tatischeff et al., 2014), the inferred ^{10}Be/^{9}Be ~6.5-7.7 $\times 10^{-4}$ would become broadly comparable with those of CV CAIs.

McKeegan et al. (2000) proposed protosolar cosmic ray irradiation model for the

origin of ^{10}Be in the early solar system. In this model, the ^{10}Be production rate depends on different irradiation conditions, such as target compositions, energetic particle fluxes, irradiation time, and irradiation distance from the proto-Sun (see chapter 3). Thus, this model can in principle explain the high and variable ^{10}Be/^{9}Be ratios recorded in CAIs.

It should be noted, however, that the accuracies of ^{10}Be/^{9}Be ratios depend largely on accurate determinations of both ^{10}B/^{11}B and ^{9}Be/^{11}B ratios. Because of relatively high ^{9}Be/^{11}B ratios, the Be-B measurements were mainly performed for melilite in CAIs. Accurate ^{9}Be/^{11}B measurements of melilite in CAIs require a melilite standard with a known chemical composition (i.e., ^{9}Be/^{11}B atomic ratio), because the sensitivities of Be and B in SIMS strongly depend on chemical compositions (so-called 'matrix effect'), and hence, the data obtained for unknown samples should be calibrated using proper standards. However, because of the lack of a suitable melilite standard available in natural terrestrial environments, previous studies have used non-matrix-matched standards, such as silica-rich glasses and basaltic glasses (McKeegan et al., 2000; Sugiura et al., 2001; MacPherson et al., 2003; Chaussidon et al., 2006; Wielandt et al., 2012; Srinivasan and Chaussidon, 2013; Dunham et al., 2016, 2017; Sossi et al., 2017). The use of such standards possibly has led to systematic errors on the ^{9}Be/^{11}B ratios of melilite in CAIs and their initial ^{10}Be/^{9}Be ratios.

Furthermore, in contrast to the case of ^{26}Al, very few data on ^{10}Be abundances have been reported for different meteoritic components; most of the previously obtained Be-B data are from the CAIs in CV chondrites. This is because sizes of CV CAIs are larger than those of CAIs in other types of chondrites so that it is possible to measure Be-B isotopic compositions by conventional SIMS techniques. In order to reveal the origin and distribution of ^{10}Be in the early solar system, much more extensive investigations of ^{10}Be abundances for various types of meteoritic components are important.

1.6. Purpose of the present work

As mentioned above, spectroscopic and theoretical studies of the YSOs revealed the time scale of the evolution of the protoplanetary disk. However, in the case of our solar system, the evolutional time scale of the protosolar disk is not well known. In order to further understand the evolutional history of the protosolar disk, it is important to reveal the material formation stages in the evolution of the protosolar disk and also to relate the observational and theoretical understandings with outcomes from meteoritical studies.

Revealing the origin of SLRs in the early solar system is a key for understanding the formation stages of meteoritic components. In particular, ^{10}Be is a unique nuclide among SLRs because it cannot be produced by thermonuclear reactions in stars, which would provide new insights into the formation conditions of solar system materials. Variable initial ^{10}Be/^{9}Be ratios reported for CV CAIs suggest that ^{10}Be was heterogeneously produced by solar cosmic ray irradiation processes. In previous studies, however, non-matrix matched standards were used for determinations of the ^{10}Be abundances in CAIs. Therefore, there is a possibility that variations in ^{10}Be/^{9}Be may come from analytical artifacts by SIMS measurements. Furthermore, most of the Be-B data thus far have been from relatively large CAIs in CV chondrites. In order to discuss the origin and distribution of ^{10}Be, investigations of Be-B systematics in various types of meteoritic components are important.

In the present work, in order to overcome this problem, I developed a protocol of high spatial resolution Be-B analysis using a CAMECA NanoSIMS 50. In addition, I synthesized melilitic and anorthitic glasses doped with Be and B for matrix-matched standards for melilite and anorthite, respectively, and investigated matrix effects on Be-B measurements by SIMS. I also applied the developed technique for CAIs in various types of chondrites (CH, CH/CBb, CO, and CO-like (ungrouped C) chondrites) and chondrules in the Y82094 carbonaceous chondrite, and discussed the origin and

distribution of ^{10}Be in the early solar system.

This doctoral thesis consists of 5 chapters. In chapter 2, I report Be/B relative sensitivities for synthetic melilitic glasses and a silica-rich glass (NIST SRM 610) measured with a NanoSIMS 50. In chapter 3, I report the initial ^{10}Be/^{9}Be ratios of CAIs in Y81020 (CO3.05), Y82094 (ungrouped C3.2), SaU290 (CH3), and Isheyevo (CH/CBb) chondrites using the developed methods described in chapter 2. In chapter 4, I report Be/B relative sensitivities for synthetic anorthitic glasses and a silica-rich glass (NIST SRM 610) and the initial ^{10}Be/^{9}Be ratios of chondrules in the Y82094 (ungrouped C3.2) chondrite. In chapter 5, I summarize the achievements of the present work.

CHAPTER 2: Beryllium-boron relative sensitivity factors for melilitic glasses measured with a NanoSIMS ion microprobe

In this chapter, I report Be/B relative sensitivities for synthetic melilitic glasses and silica-rich NIST SRM 610 glass measured with a NanoSIMS ion microprobe. I found that the Be/B relative sensitivities for melilitic glasses are identical to that of the NIST 610 glass within uncertainties, which suggests that the matrix effects, at least between the NIST 610 glass and melilite, are not significant with respect to Be–B measurements. The present results confirm that the observed variations in the $^{10}Be/^{9}Be$ ratios for CV calcium-aluminum-rich inclusions (CAIs) are not analytical artifact and the origin of ^{10}Be should be attributed to irradiation by the active early sun. It is also inferred that the $^{10}Be/^{9}Be$ ratios of *F*ractionation and *U*nidentified *N*uclear effect (FUN) CV CAIs are not significantly lower than those for normal (non-FUN) CV CAIs, consistent with the irradiation origin. The major part of this chapter has been published in Geochemical Journal (Fukuda et al., 2018).

2.1. Introduction

Beryllium-10, which decays to ^{10}B with a half-life of 1.4 Myr (Korschinek et al., 2010), cannot be produced by thermonuclear reactions in stars but by spallation reactions induced by galactic and/or stellar cosmic rays (e.g., McKeegan et al., 2000; Desch et al., 2004). Previous Be–B measurements on calcium–aluminum-rich inclusions (CAIs), which are believed to be the earliest solids in the early solar system (e.g., Amelin et al., 2010), have demonstrated that this short-lived radionuclide was present in the early solar system with initial $^{10}Be/^{9}Be$ ratios ranging from 1.3×10^{-4} to 1.0×10^{-2} (McKeegan et al., 2000; Sugiura et al., 2001; MacPherson et al., 2003; Chaussidon et al., 2006; Liu et al., 2010; Wielandt et al., 2012; Srinivasan and Chaussidon, 2013; Gounelle et al., 2013; Dunham et al., 2016, 2017; Sossi et al., 2017). However, the origin of ^{10}Be in the early solar system is unknown. As described in chapter 1, several mechanisms have been suggested for the origin of ^{10}Be including enhanced trapping of galactic cosmic rays (GCRs) in the collapsing cloud core (Desch et al., 2004), solar cosmic ray irradiation (e.g., McKeegan et al., 2000), and stellar processes with neutrino reactions in a relatively low-mass supernova (Banerjee et al., 2016). Varying initial ^{10}Be abundances in CAIs indicate heterogeneous production and/or distribution of ^{10}Be in the early solar system, preferring local production of ^{10}Be near the proto-Sun.

Most of the Be–B measurements using secondary ion mass spectrometry (SIMS) have been performed on melilite (solid solution between gehlenite, $Ca_2Al_2SiO_7$, and åkermanite, $Ca_2MgSi_2O_7$) in CAIs into which Be preferentially partitions (Lauretta and Lodders, 1997). With respect to SIMS measurements, the $^{9}Be/^{11}B$ relative sensitivity factor [RSF: defined by $(^{9}Be^{+}/^{11}B^{+})_{SIMS}/(^{9}Be/^{11}B)_{TRUE}$] of melilite is necessary to calculate the Be/B ratios using $^{10}B/^{11}B$ vs. $^{9}Be/^{11}B$ (isochron) diagrams. In previous studies, the RSF for melilite has been assumed to be the same as that of silica-rich glasses such as the NIST SRM 610 glass (e.g., MacPherson et al., 2003). However, the chemical

compositions of these standards are considerably different from that of melilite and the above-mentioned assumption might therefore be invalid. Thus, previously reported initial $^{10}Be/^{9}Be$ ratios may include serious systematic errors. For example, a significant difference in the Mn/Cr RSF was observed between silicates and carbonates, which resulted in significant errors in the Mn–Cr ages for carbonates (Sugiura et al., 2010; Fujiya et al., 2012; Steele et al., 2017). In this study, to overcome this problem, I synthesized five melilitic glasses doped with Be and B and evaluated RSFs for these glasses using a NanoSIMS 50 (for Be^{+}/B^{+} intensity ratios) and a laser ablation-inductively coupled plasma-mass spectrometer (LA-ICP-MS; for Be/B elemental ratios) which is known to be less sensitive to that of the matrix effect. In this chapter, I report the newly determined RSFs, which are essential for the determination of accurate initial abundances of ^{10}Be and to discuss its origin in the early solar system.

2.2. Experimental

2.2.1. Production of Be- and B-bearing melilitic glasses

I synthesized five glasses with approximate melilitic compositions and åkermanite numbers (Åk#s; see Table 2.2 for the definition) ranging from 24 to 63 that were doped with trace amounts of Be and B with varying Be/B ratios (Table 2.3). The glasses were prepared by melting mixtures of oxide and acid powders. First, appropriate amounts of reagents of SiO_2, Al_2O_3, MgO, $CaCO_3$, and BeO were mixed according to the desired compositions of the standards. Second, I prepared a 1 wt.% 1% H_3BO_4 solution and added to the oxide mixtures to dope B with desired concentrations. I used H_3BO_4 solution instead of solid H_3BO_4, because weighing the appropriate amount of H_3BO_4 in solid form was very difficult due to its small size. The total weight of the mixtures was ~5 g. The

mixtures were dried, homogenized using agate mortar, and used for synthesis of the glass standards. About 0.3 g each of the homogenized mixtures was wrapped in Pt-foil, heated, melted with a blowtorch, and quenched by dropping them into Milli-Q water. The synthesized glasses (~500 × 500 μm^2) were embedded in epoxy together with a NIST SRM 610 glass standard and then polished. The sample mount was cleaned with Mill-Q water and ethanol to remove surface contamination. The sample was coated with carbon after drying to prevent surface charge during subsequent electron microprobe and SIMS analyses. A representative BEI of synthetic glasses is shown in Fig. 2.1.

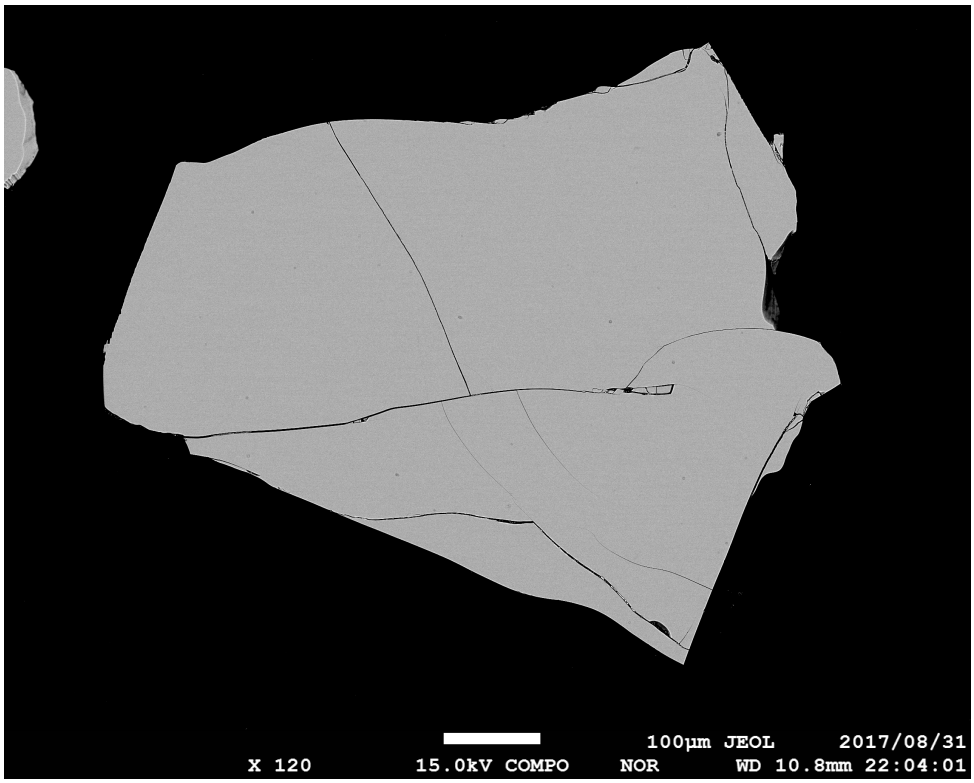

Fig. 2.1. A representative backscattered electron image of a synthetic Be- and B-bearing melilitic glass.

The major element concentrations of the synthetic glasses were determined with a JXA-8530F field-emission gun electron microprobe installed at the University of Tokyo using a 15 keV accelerating voltage, 12 nA beam current, ~1 μm focused beam, and wavelength-dispersive X-ray spectroscopy (WDS). Matrix effects were corrected using the ZAF method. The concentrations of major elements in the synthesized glasses are listed in Table 2.2. The major element concentrations are consistent with expected concentrations from the weighing of oxide powders. The approximate Åk#s and Be and B concentrations measured with LA-ICP-MS (see below) are also shown.

2.2.2. Determination of the RSF

The ion intensities of Be and B were determined with a NanoSIMS 50 ion probe at the Atmosphere and Ocean Research Institute (AORI) of the University of Tokyo. The NanoSIMS measurements were performed in multi-collection mode. A $^{16}O^-$ primary ion beam (~1 nA intensity and ~5 μm in diameter) was rastered over 10 × 10 μm^2 areas (32 × 32 pixels with a dwell time of 200 μs/pixel) to stabilize the secondary ion intensities. To remove the carbon coating and surface contamination before each analysis, a ~1 nA primary ion beam was rastered over 10 × 10 μm^2 areas for ~10 min. Secondary ions of $^9Be^+$, $^{10}B^+$, $^{11}B^+$, and $^{30}Si^+$ were then detected simultaneously with secondary electron multipliers (EMs). The measurements were performed with a mass resolving power (MRP) of 1500 at a peak height of 1%. This MRP is high enough to separate major interfering ion peaks: $^9B^1H^+$ on $^{10}B^+$ (~1400) and $^{10}B^1H^+$ on $^{11}B^+$ (~960), where MRP required for separation is given in the parenthesis. The intensities of $^9Be^+$, $^{11}B^+$, and $^{30}Si^+$ were (2.1–3.8) × 10^4 cps, (0.3–6.0) × 10^3 cps, and (0.1–1.7) × 10^5 cps, respectively. An electronic beam blanking mode was applied such that only signals from the central 24 × 24 pixel area were collected. This blanking helped to avoid contributions from scattered

ions from the surroundings. The relative sensitivities between the EMs used for the Be and B measurements were checked after the measurement and corrected to calculate RSFs. The dead time (~44 ns) of the counting system was also corrected. The EM background (much lower than ~0.05 cps) was not corrected because it was negligible compared with the count rates of ^{9}Be and ^{11}B for the samples. Measurements on synthetic melilitic glasses were conducted only near the center of the individual glasses.

After the NanoSIMS analyses, the Be and B concentrations near NanoSIMS analysis spots on the same glasses were determined using a LA-ICP-MS. Laser ablation was performed with an in-house laser ablation system (Cyber Probe) combined with a titanium–sapphire (Ti:S) femtosecond laser (IFRIT, Cyber Laser, Japan) and galvano metric fast scanning laser system (Yokoyama et al., 2011). A single quadrupole mass spectrometer (iCAP Qc, Thermo Fisher Scientific, USA) was utilized. The LA-ICP-MS measurements were performed in spot analysis mode. We obtained ion intensities for $^{7}Li^{+}$, $^{9}Be^{+}$, $^{10}B^{+}$, $^{11}B^{+}$, $^{24}Mg^{+}$, $^{29}Si^{+}$, and $^{43}Ca^{+}$. Ablation pits of ~25 μm in diameter were produced by fast circular scanning of a laser beam with a diameter of 10 μm. The scanning repetition rate and laser fluence were optimized to obtain maximum signal intensities for ^{238}U and ^{11}B using NIST SRM 610 as a standard. The NIST 610 glass was also used as reference for the correction of the relative sensitivities of Be, B, and Ca. The Be and B concentrations were determined using the observed $^{9}Be^{+}/^{43}Ca^{+}$ and $^{11}B^{+}/^{43}Ca^{+}$ intensity ratios and ^{43}Ca concentrations (calculated from total Ca concentrations assuming normal isotopic ratios) of the samples. The NIST SRM 612 and BCR-2G glasses were measured as secondary standards. The instrumentation and detailed analytical conditions are summarized in Table 2.1.

Table 2.1. Instrumentations and operational conditions of LA-ICP-MS

1. ICP-Mass spectrometer	
Instrument	iCAP Qc (Thermo Fisher Scientific, Massachusetts, USA)
ICP RF incident power	1550 W
Plasma gas flow rate	14.0 L min^{-1}
Auxiliary gas	0.8 L min^{-1}
He flow rate	0.60 L min^{-1}
Ar makeup flow rate	1.05 L min^{-1}
Monitored isotope	^{7}Li, ^{9}Be, ^{10}B, ^{11}B, ^{24}Mg, ^{29}Si, ^{43}Ca
Date acquisition mode	Time resolved analysis (TRA)
Dwell time	0.01 s
Detector	EM (Pulse counting)
2. Laser ablation system	
Instrument	CyberProbe UV
Laser	Ti:S femtosecond laser
Pulse duration	227 fs
Wavelength	260 nm (THG)
Objective lens	f-theta lens (f=100mm)
Repetition rate	50, 100, 250 Hz
Fluence	6.5 ~ 9.8 J s^{-1}
Ablation pit size	20 ~ 30 μm
Stabilizer	Baffle type (Tunheng and Hirata, 2004)
3. Standardization	
Calibration standard	Glass standard reference material (NIST SRM610)
Secandary standard	Glass standard reference material (NIST SRM612 and BCR-2G)

2.3. Results

The Be and B concentrations in the melilitic glasses obtained from LA-ICP-MS analyses are listed in Table 2.2. The measured Be concentrations are slightly lower (3-9%), and the measured B concentrations are systematically higher (27-33%) than expected concentrations from weighing of the BeO and H_3BO_4 powders. I cannot find the cause for the discrepancies, but one candidate is a preparation process of the starting materials because B was doped separately in the form of diluted solutions. To verify the accuracy of the Be and B concentrations in the melilitic glasses using LA-ICP-MS, I also measured NIST 612 and BCR-2G glasses as secondary standards under the same analytical conditions. The Be and B concentrations of the NIST 612 and BCR-2G glasses are consistent with literature values (Jochum et al., 2011; Jacob, 2006), which justifies the current LA-ICP-MS analysis (see Table 2.2).

Table 2.2. Major element compositions, and Be and B concentrations in synthetic melilitic glasses and NIST 610 glass

Sample	Åk# [*1]	MgO	2SD	Al_2O_3	2SD	SiO_2	2SD	CaO	2SD	Na_2O	total	No. of analyses
		wt %										
20-1B	25	3.49	± 0.15	26.78	± 1.46	28.22	± 1.29	40.90	± 0.48	-	99.38	20
30-1B	24	3.16	± 0.23	25.85	± 3.50	29.39	± 3.12	41.24	± 1.55	-	99.64	20
60-1A	25	3.48	± 0.15	26.07	± 0.44	28.72	± 0.51	40.84	± 0.47	-	99.11	20
50-1C	43	5.36	± 0.12	18.27	± 0.68	34.07	± 0.59	41.23	± 0.61	-	98.93	20
70-2A	63	6.74	± 0.16	10.03	± 1.03	41.34	± 1.07	41.52	± 0.64	-	99.63	20
BCR-2G [*2]		3.59		13.8		54.3		7.22		3.3		
NIST 612 [*3]		-		2.06		71.7		11.93		14.0		
NIST 610 [*4]		0.0057		1.98		69.4		11.59		13.6		

Sample	Be (ppm)	2SD [*5]	B (ppm)	2SD [*5]	No. of analyses
20-1B	912	± 34	79	± 3	7
30-1B	901	± 69	58	± 6	10
60-1A	2204	± 205	69	± 10	3
50-1C	1547	± 107	58	± 10	4
70-2A	2188	± 122	58	± 6	5
BCR-2G [*2]	2.1	± 0.5	7.2	± 1	1
NIST 612 [*3]	39	± 3	35	± 3	5
NIST 610 [*4]	476		350		

[*1] Åk#: approximate åkermanite numbers, calculated from Mg(cation)/(Mg(cation)+Al(cation)/2).

[*2] Major element concentrations from Jochum et al. (2005).

[*3] Major element concentrations from Jochum et al. (2011).

[*4] Major elements, Be, and B concentrations from Jochum et al. (2011).

[*5] Errors of BCR-2G are counting errors (2 σ) because the sample was measured only 1 spot.

The $^{9}Be/^{11}B$ atomic ratios (calculated from the Be and B concentrations in Table 2.2), $^{9}Be^{+}/^{11}B^{+}$ ion intensity ratios measured with the NanoSIMS, and corresponding Be/B RSFs calculated for individual glasses are listed in Table 2.3. Figure 2.1a shows the $^{9}Be^{+}/^{11}B^{+}$ intensity ratios as a function of atomic $^{9}Be/^{11}B$ ratios. The $^{9}Be^{+}/^{11}B^{+}$ intensity ratios and atomic $^{9}Be/^{11}B$ ratios of the synthesized glasses correlate well. The RSFs calculated for individual glasses are identical within uncertainties (2.47 ± 0.21 to 2.82 ± 0.43). Note that five glasses have different chemical compositions, with Åk# ranging from 24 to 63. The obtained RSFs are independent of the åkermanite numbers. Therefore, I used the weighted mean of the five datapoints and obtained the RSF of 2.55 ± 0.11 (2σ). I also determined the Be/B RSF for NIST SRM 610 under the same analytical conditions. The RSF shows a small day-to-day variation from 2.44 ± 0.12 (2 standard deviations, SD) to 2.68± 0.05 (2 SD), but the RSF of our melilitic glasses obtained during the analytical period is 2.44 ± 0.12 (2 SD). The present results demonstrate that the Be/B RSF of the synthetic melilitic glasses is identical to that of NIST SRM 610, within uncertainties.

I also determined the RSFs of $^{9}Be/^{30}Si$ and $^{11}B/^{30}Si$ for melilitic glasses and NIST 610. The Be/Si and B/Si RSFs obtained for melilitic glasses are slightly higher than or almost comparable to those of the NIST 610 glass (see Fig. 2.2b and 2.2c). These observations suggest matrix effects between melilitic glasses and NIST 610 glass, at least for some elements. Therefore, it may be fortuitous that the Be/B RSF does not show noticeable matrix effects between melilitic glasses and NIST 610 glass. The $^{9}Be/^{30}Si$ and $^{11}B/^{30}Si$ atomic ratios (calculated from the Be, B, and SiO_2 concentrations in Table 2.2), $^{9}Be^{+}/^{30}Si^{+}$ and $^{11}B^{+}/^{30}Si^{+}$ ion intensity ratios measured with the NanoSIMS, and corresponding Be/Si and B/Si RSFs calculated for individual glasses are listed in Table 2.4 and 2.5, respectively.

Table 2.3. Be/B atomic and ion intensity ratios, and the calculated relative sensitivity factors

Sample	Åk#	$^{9}Be/^{11}B$ atomic ratios (atomic ratio) *2	No. of Analyses	$^{9}Be^{+}/^{11}B^{+}$ ion intensity ratio) *3	No. of Analyses	RSF *1
20-1B	25	17.3 ± 0.6	7	44.3 ± 2.2	4	2.57 ± 0.16
30-1B	24	23.3 ± 1.6	10	57.6 ± 2.9	4	2.47 ± 0.21
60-1A	25	48.2 ± 6.9	3	135.9 ± 6.9	3	2.82 ± 0.43
50-1C	43	40.4 ± 4.8	4	100.0 ± 11.3	4	2.48 ± 0.40
70-2A	63	56.4 ± 4.6	5	145.9 ± 11.5	4	2.59 ± 0.30
weighted mean						***2.55 ± 0.11***
NIST 610		2.03		4.98 ± 0.25	11	2.44 ± 0.12

*1 relative sensitivity factor: $(^{9}Be^{+}/^{11}B^{+})_{NanoSIMS}$ $/(^{9}Be/^{11}B)_{atomic}$. Errors are 2 σ. *2 calculated from Be and B concentrations in Table 1

*2 calculated from Be and B concentrations in Table 1 assuming terrestrial isotopic ratios. Errors are 2 σ.

*3 Errors are 2 Standard Deviation (2SD). If 2SD errors are smaller than the reproducibility of NIST 610 (2SD), the latter was adopted.

Table 2.4. Be/Si atomic and ion intensity ratios, and the calculated relative sensitivity factors

Sample	Åk#	$^{9}Be/^{30}Si$ (atomic ratio) *2	$^{9}Be^{+}/^{30}Si^{+}$ (ion intensity ratio) *3	$^{9}Be/^{30}Si$ RSF *1
20-1B	25	0.698 ± 0.041	0.764 ± 0.033	1.096 ± 0.080
30-1B	24	0.661 ± 0.087	0.703 ± 0.094	1.063 ± 0.199
60-1A	25	1.656 ± 0.157	1.736 ± 0.066	1.048 ± 0.107
50-1C	43	0.980 ± 0.070	0.998 ± 0.051	1.019 ± 0.089
70-2A	63	1.142 ± 0.070	1.216 ± 0.046	1.065 ± 0.077
weighted mean				***1.058 ± 0.049***
NIST 610		0.148	0.138 ± 0.005	0.929 ± 0.035

Table 2.5. B/Si atomic and ion intensity ratios, and the calculated relative sensitivity factors

Sample	Åk#	$^{11}B/^{30}Si$ (atomic ratio) *2	$^{11}B^{+}/^{30}Si^{+}$ (ion intensity ratio) *3	$^{11}B/^{30}Si$ RSF *1
20-1B	25	0.0404 ± 0.002	0.0227 ± 0.0013	0.562 ± 0.045
30-1B	24	0.0284 ± 0.004	0.0161 ± 0.0022	0.565 ± 0.114
60-1A	25	0.0344 ± 0.005	0.0168 ± 0.0003	0.489 ± 0.071
50-1C	43	0.0243 ± 0.004	0.0131 ± 0.0013	0.539 ± 0.110
70-2A	63	0.0203 ± 0.002	0.0110 ± 0.0014	0.541 ± 0.089
weighted mean				***0.543 ± 0.032***
NIST 610		0.0727	0.0364 ± 0.0006	0.500 ± 0.009

*1 relative sensitivity factor: $(^{9}Be^{+}(or^{11}B^{+})/^{30}Si^{+})_{NanoSIMS}/(^{9}Be\ (or^{11}B)/^{30}Si)_{atomic}$. Errors are 2 σ.
Note that RSFs are not absolute values because relative sensitivities between the EMs used for Be and Si (B and Si) were not checked.

*2 calculated from SiO_2, Be, and B concentrations in Table 1 assuming terrestrial isotopic ratios. Errors are 2 σ.

*3 Errors are 2 Standard Deviation (2SD).

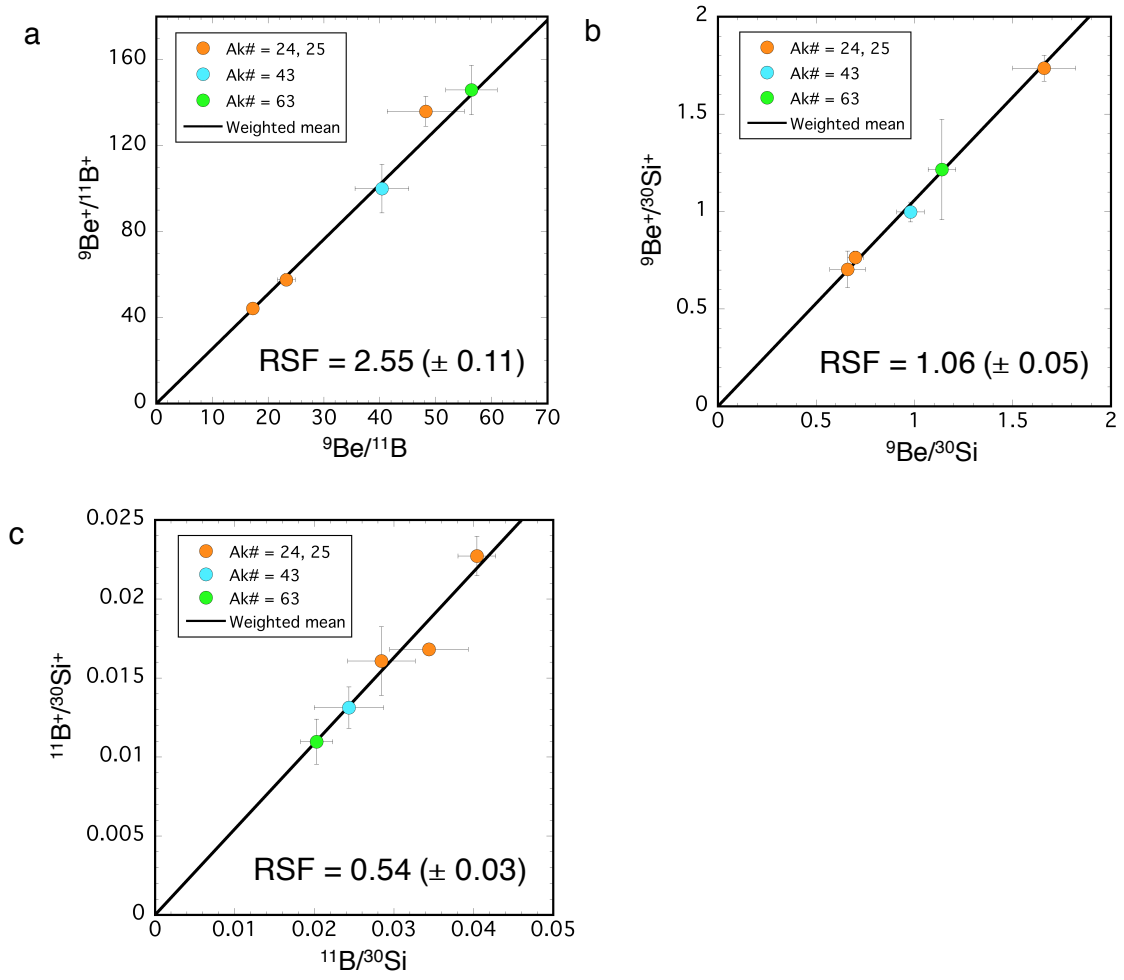

Fig. 2.2. Ion intensity ratios as a function of atomic ratios determined on five synthetic melilitic glasses. The error bars represent 2 standard deviations (SD) evaluated from repeated measurements of individual glasses. The slope defines the weighted mean value of the relative sensitivity of five glasses. (a) $^{9}Be^{+}/^{11}B^{+}$ ratios as a function of Be/B atomic ratios. The sensitivity difference between the electron multipliers (EMs) for $^{9}Be^{+}$ and $^{11}B^{+}$ was corrected. (b) $^{9}Be^{+}/^{30}Si^{+}$ ratios as a function of Be/Si atomic ratios determined for five synthetic melilitic glasses. (c) $^{11}B^{+}/^{30}Si^{+}$ ratios as a function of B/Si atomic ratios determined for five synthetic melilitic glasses. Note that RSFs of (b) and (c) are not absolute values because sensitivity differences between EMs for $^{9}Be^{+}$ (or $^{11}B^{+}$) and $^{30}Si^{+}$ were not corrected.

2.4. Discussion

2.4.1. Homogeneity of major elements, Be, and B in the synthetic glasses

In order to check a homogeneity of major element concentrations, I conducted repeated measurements using FE-EPMA (N = 20: see Table. 2.1). The deviations of each oxide concentrations were ~5% (2SD), except for 30-1B. On the other hand, the deviations of major element concentrations in 30-1B are systematically higher (~14%) than those of other melilitic glasses, suggesting some degrees of heterogeneity existed in 30-1B.

I also conducted repeated measurements of Be and B using LA-ICP-MS (N = ~ 10: see Table. 2.2). The deviations of Be and B concentrations of individual melilitic glasses were 4-16% (2 SD), which are larger than that of NIST 610 (~3% (2SD): N = 11). The results suggest that some degrees of heterogeneity existed in Be and B concentrations of melilitic glasses. Therefore, I propagated the uncertainties thus estimated to calculate RSFs. However, as previously mentioned, I measured the Be and B concentrations of melilitic glasses near NanoSIMS analysis spots on the same glasses. This would help to minimize the effect of some heterogeneities for an accuracy of calculated RSFs.

I conducted only three or four NanoSIMS measurements for each glass (see Table. 2.3). Although these measurements numbers would be insufficient for evaluating of homogeneity, the deviations of $^{9}Be^{+}/^{11}B^{+}$ ratios were ~11% (2SD), which are comparable to those of Be and B concentrations determined by LA-ICP-MS. Therefore, the differences of measurement sizes between LA-ICP-MS (25 ×25 μm^2) and NanoSIMS (10 × 10 μm^2) may not be significant for determinations of RSFs.

2.4.2. The similarity and difference between the RSF of melilite, pyroxene, and silica-rich glasses and their inferences for the origin of ^{10}Be in the early solar system

The present results demonstrate that sample matrix does not significantly (~6%) affect the relative ionization efficiencies of Be and B of the melilitic glasses and NIST 610 glass standard. Hence, the NIST 610 (and 612) glass can be used as a proper standard for accurate Be-B SIMS measurements on melilite in CAIs. Below, I will compare Be-B data previously reported for CV CAIs that were obtained using different standards. If necessary, I will apply appropriate corrections based on the present results. Note that the Be and B concentrations of CV CAIs (several hundreds and several tens ppb, respectively) are about 3 orders of magnitude lower than those of the present synthetic melilitic glasses. Thus, linearity must be checked when I apply the obtained Be/B RSFs for the natural CAIs. In the $^{9}Be/^{30}Si$ *vs* $^{9}Be^{+}/^{30}Si^{+}$ (Fig. 2.2b) and $^{11}B/^{30}Si$ *vs* $^{11}B^{+}/^{30}Si^{+}$ diagram (Fig. 2.2c), the regression lines pass through the origin within uncertainties (intercepts of Y axis are 0.06 ± 0.14 (2σ) and -0.001 ± 0.004 (2σ), respectively). This may indicate that linearity of the Be/B relative sensitivities hold up to the Be and B concentrations of the melilitic glass standards, justifying the use of the obtained RSFs to the natural melilite in CAIs.

MacPherson et al. (2003) and Dunham et al. (2016, 2017) used the NIST (NBS) 610 and 612 standards to determine the Be/B RSF and reported initial $^{10}Be/^{9}Be$ ratios of CV CAIs including a few *F*ractionation and *U*nidentified *N*uclear effect (FUN) CAIs. The initial $^{10}Be/^{9}Be$ ratios vary from 1.3×10^{-4} to 11.6×10^{-4} for normal (i.e., non-FUN) CAIs and $(3.0 \pm 1.2) \times 10^{-4}$ (MacPherson et al., 2003) or $< 5.8 \times 10^{-4}$ (Dunham et al., 2017) for FUN CAIs. No corrections are needed for these data.

Sugiura et al. (2001) and Wielandt et al. (2012) conducted Be–B measurements on the same CAIs (E38 and E48) from Efremovka. However, the $^{10}Be/^{9}Be$ ratios reported

by Sugiura et al. (2001; $(6.1 \pm 1.2) \times 10^{-4}$ and $(8.1 \pm 3.1) \times 10^{-4}$, respectively) are higher than those reported by Wielandt et al. (2012; $(4.43 \pm 0.61) \times 10^{-4}$ and $(4.82 \pm 0.25) \times 10^{-4}$, respectively). Wielandt et al. (2012) determined a Be/B RSF of ~2.6 using the NIST SRM glass 612 (SiO_2 = 71.8 wt%; Jochum et al., 2011) and ~1.78 using GSC-1G and GSD-1G glasses (SiO_2 = 52.5 wt% and 53.0 wt%, respectively; Jochum et al., 2005). The former is in good agreement with our RSFs for NIST glass 610 and melilitic glasses, but the latter is 30% lower than the RSF for our melilitic glasses. Wielandt et al. (2012) adopted the latter RSF, but the present results suggest that the former RSF may be appropriate for accurate Be–B measurements on melilites in CAIs. If I use 2.6 instead of 1.78 as the Be/B RSF, the revised values ($6.3 \pm 0.9 \times 10^{-4}$ and $7.0 \pm 0.4 \times 10^{-4}$, respectively) are consistent with those obtained by Sugiura et al. (2001), within uncertainties.

Note that the Be/B RSFs for NIST 610 and 612 determined by three different instruments are similar to each other, i.e., ~2.6 (IMS-1280; Wielandt et al., 2012), ~2.5 (IMS-6f; MacPherson et al., 2003), and ~2.44 (NanoSIMS; this study). This suggests that the relative sensitivities of Be and B do not depend much on the ion optics of the instruments but are more intrinsic to sputtering and ionization processes. In fact, Ito and Messenger (2016) also reported similar RSFs for rare earth elements determined by different instruments (IMS-3f, IMS-4f, and NanoSIMS).

Sugiura et al. (2001) determined a Be/B RSF of 2.67 ± 0.09 for a suite of geological standards with varying SiO_2 contents (51.0–72.3 wt%; Imai et al., 1995). Although Sugiura et al. (2001) did not measure the RSF of NIST glasses, a similar RSF was obtained for the NIST 610 and 612 glasses using the same instrument (IMS-6f; MacPherson et al., 2003). Hence, the $^{10}Be/^{9}Be$ ratios reported in Sugiura et al. (2001) may not need corrections. Note that our melilitic glasses and NIST 610 measured in this study also have varying SiO_2 contents (28.2–41.3 wt% and 69.4 wt%, respectively). This suggests that the Be/B RSF is rather insensitive to the SiO_2 content.

McKeegan et al. (2000) and Chaussidon et al. (2006) used a synthetic GB4 glass

standard (SiO_2 = 72.9 wt%; Gurenko et al., 2005) and measured Be–B isotopes in CV CAIs with an IMS-1270 ion microprobe. The Be/B RSF measured by Chaussidon et al. (2006) varies from 2.51 to 2.88 (with an average of 2.73), which overlaps with that of NIST glass standards determined by three different instruments, as described above. Therefore, these data may not need corrections. Recently, Sossi et al. (2017) also used the GB4 standard for the Be–B analysis of CV CAIs. However, their Be/B RSF (~3.17) is significantly higher than that of GB4 determined by Chaussidon et al. (2006) or that of silica-rich NIST glasses obtained by other researchers (see above). The cause for this difference is uncertain but may be attributed to different analytical conditions. In this case, I cannot make proper corrections.

Previous studies indicated a large variation in the $^{10}Be/^{9}Be$ ratios of CV CAIs, from 1.3 to 11.6×10^{-4} (McKeegan et al., 2000; Sugiura et al., 2001; MacPherson et al., 2003; Chaussidon et al., 2006; Wielandt et al., 2012; Srinivasan and Chaussidon, 2013; Dunham et al., 2016, 2017). The present results confirm that most of the previous data may not need corrections. Hence, the variation in the $^{10}Be/^{9}Be$ ratios of CV CAIs is real. Note that the data for other types of refractory inclusions, such as hibonite and grossite inclusions, also show a large variation in the $^{10}Be/^{9}Be$ ratios, from 5.3×10^{-4} to 100×10^{-4} (Liu et al., 2010; Gounelle et al., 2013). These data, however, must be re-evaluated because the Be/B RSFs for hibonite and grossite may, in principle, not be identical to those of melilite or NIST standard glasses, especially considering that hibonite and grossite are non-silicate minerals.

The observed variation in the $^{10}Be/^{9}Be$ ratios suggests the local production of ^{10}Be, which is consistent with the production of ^{10}Be by solar cosmic ray irradiation (e.g., McKeegan et al., 2000). As mentioned above, however, Banerjee et al. (2016) showed that ^{10}Be is produced by the neutrino spallation process with low mass core-collapse supernovae. They found that this model can produce ^{10}Be at a level of $^{10}Be/^{9}Be \sim (5.2\text{-}6.4) \times 10^{-4}$. Moreover, Tatischeff et al. (2014) demonstrated that irradiation of the presolar

molecular cloud by background GCRs produced a steady-state $^{10}Be/^{9}Be$ ratio $\leq 1.3 \times 10^{-4}$ at the time of solar system formation. Thus, the inferred initial $^{10}Be/^{9}Be$ ratio included both ^{10}Be from core-collapse supernovae and that from presolar molecular cloud is $^{10}Be/^{9}Be \sim (6.5\text{-}7.7) \times 10^{-4}$, which is in accord with the average value of CV CAI ($^{10}Be/^{9}Be = 6.7 \times 10^{-4}$). Thus, these mechanisms cannot be completely ruled out for the origin of ^{10}Be. Further studies are required to reveal the origin of ^{10}Be in the early solar system.

2.4.3. Implications for the CAI formation process

Figure 2.3 summarizes initial $^{10}Be/^{9}Be$ ratios previously reported for CV normal and FUN CAIs (filled symbols). The original data of Wielandt et al. (2012) are shown as open symbols and the corrected data, assuming a Be/B RSF of 2.6, are displayed as filled symbols. Note that the data for FUN CAIs were relatively low (2.8×10^{-4} to 3.4×10^{-4}; Wielandt et al., 2012) before the correction. However, they are much higher after the correction (4.0×10^{-4} to 4.9×10^{-4}). Based on the original data, Wielandt et al. (2012) and Tatischeff et al. (2014) suggested that the $^{10}Be/^{9}Be$ ratios recorded in FUN CAIs represent the baseline level present in the protosolar molecular cloud. However, the corrected $^{10}Be/^{9}Be$ ratios of FUN CAIs are higher than that of the baseline level of the molecular cloud ($\sim1.3\times10^{-4}$ to 3.4×10^{-4}; Tatischeff et al., 2014) and within the range of normal CV CAIs (see Fig. 2.3). Furthermore, Dunham et al. (2017) recently reported a very low $^{10}Be/^{9}Be$ ratio of $1.27 \pm 0.50\times10^{-4}$ for a normal CV CAI (B4), that is, much lower than the corrected $^{10}Be/^{9}Be$ ratios of CV FUN CAIs. These observations indicate that the initial $^{10}Be/^{9}Be$ ratios of CV FUN CAIs cannot be explained by a baseline level of ^{10}Be abundances in the protosolar molecular cloud.

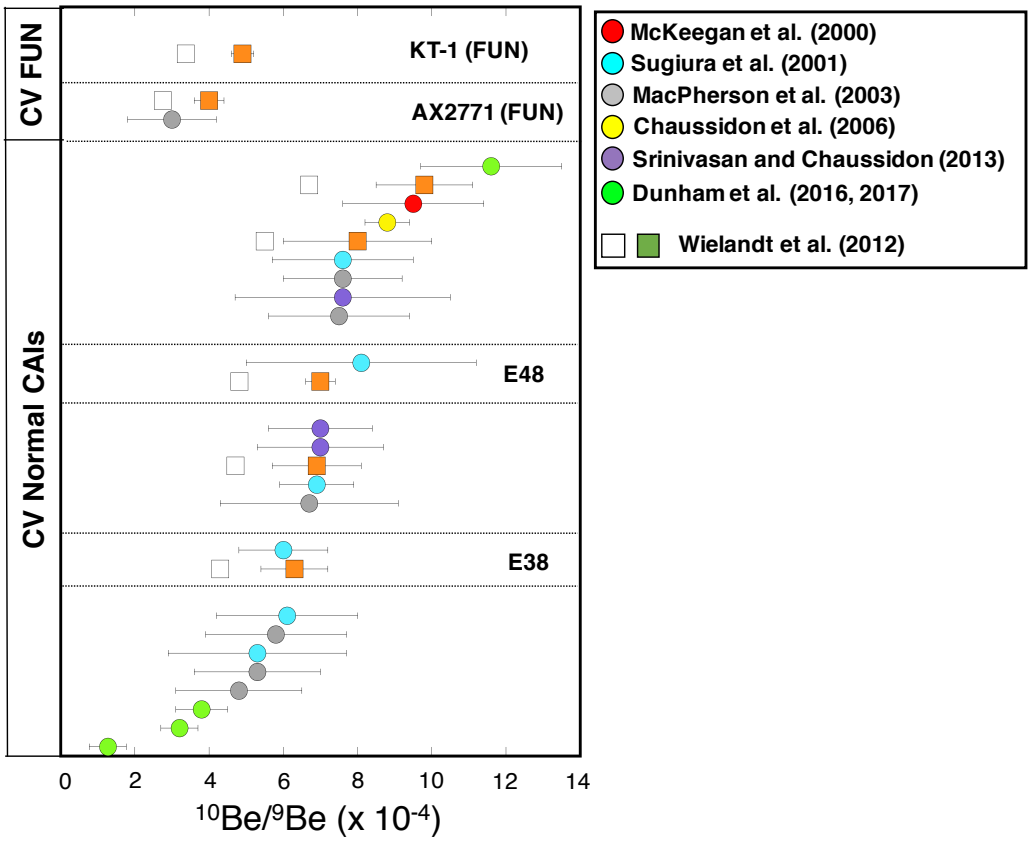

Fig.2.3. Compilation of the reported initial $^{10}Be/^{9}Be$ ratios of CV normal and *F*ractionation and *U*nidentified *N*uclear effect (FUN) CAIs (filled circles: McKeegan et al., 2000; Sugiura et al., 2001; MacPherson et al., 2003; Chaussidon et al., 2006; Srinivasan and Chaussidon, 2013; Dunham et al., 2016, 2017; open squares: Wielandt et al., 2012). The calculated initial $^{10}Be/^{9}Be$ ratios using the RSF of the NIST 612 reported by Wielandt et al. (2012; see text) (filled squares) are also plotted. The error bars represent 2 σ.

2.4.4. Controlling factors of relative sensitivity factors

As discussed above, the present results demonstrate that sample matrix does not significantly affect the relative ionization efficiencies of Be and B at least for the melilitic glasses and NIST 610 glass standard. The lack of matrix dependency is consistent with the case for rare earth elements (REEs) among various matrices (Sano et al., 2002). In this study, I also found that Be is ~2.5 times more effectively ionized than B in the NanoSIMS instrument. Here I consider the reason why ionization efficiency of Be is higher than that of B. Based on the local thermal equilibrium (LTE) model proposed by Andersen and Hinthorne (1973) to quantify secondary ion yields, Reed (1983) developed the following equation.

$$\frac{n_{M^+}}{n_M} = \text{const.} \times \frac{T^{3/2}}{n_{e^-}} \frac{B_{M^+}}{B_M} \exp\left[-\frac{I_{M^+}}{kT}\right]$$

where M, M^+ and e^- are atoms, positive ions, and electrons, respectively, n is the number of atoms, positive ions, and electrons, B is the partition function, T is the plasma temperature in K, and I_M is the ionization potential. Then relative secondary ion yields are likely to be a function of the ionization potential as follows:

$$\frac{S_A}{S_B} = \text{const.} \times \exp\left[-\frac{I_A - I_B}{kT}\right]$$

where S is the secondary ion yield of the indicated element. Reed (1983) suggested that no clear correlation exists between the first valence ionization potential and the relative secondary ion yields of REEs. The first valence ionization potentials of Be and B are almost the same (899.5 and 800.6 kJ/mol, respectively), indicating no clear relationship between the first valence ionization potential and the relative secondary ion yields of Be and B. Sano et al. (2002) reported a correlation between the second valence ionization

potential and the relative secondary ion yields of REEs. The second ionization potential of Be (1757.1 kJ/mol) is lower than that of B (2427.1 kJ/mol). Hence, the relationship between the second ionization potentials and ionization efficiencies of Be and B in the NanoSIMS is consistent with the reported correlation by Sano et al. (2002). However, the physical mechanisms of this correlation are not well known. Thus, at present it is not well understood to what extent the LTE model is applicable to quantify a RSF of given elements. Further studies are required for understanding the controlling factors of RSFs in SIMS measurements.

2.5. Summary

In this study, I synthetized five melilitic glasses and investigated the Be/B RSFs of these glasses using a NanoSIMS 50 and LA-ICP-MS. I found that the Be/B RSFs of melilitic glasses are (1) independent of the Åk# and (2) identical to that for NIST 610 silica-rich glass within uncertainties. After proper correction of previous data based on the present results, the revised $^{10}Be/^{9}Be$ ratios of CV FUN CAIs become higher and well within the range of $^{10}Be/^{9}Be$ ratios of CV normal CAIs. Hence, the $^{10}Be/^{9}Be$ ratios of CV FUN CAIs may not represent a baseline level of ^{10}Be abundances in the protosolar molecular cloud, but similar formation processes are suggested both for FUN and normal (non-FUN) CAIs, possibly spallation reactions induced by solar cosmic ray irradiation.

CHAPTER 3: Li-Be-B and Al-Mg isotopic compositions of CAIs in CO, ungrouped C, CH, and CH/CBb chondrites.

In this chapter I report Li-Be-B and Al-Mg isotopic compositions of CAIs in Yamato 81020 (CO), Yamato 82094 (ungrouped C; CO-like), Sayh al Uhaymir 290 (CH), and Isheyevo (CH/CBb) chondrites. The inferred $^{10}Be/^{9}Be$ ratios obtained for these CAIs are much higher and more variable than previously thought. These results strongly suggest that ^{10}Be was produced by solar cosmic ray irradiation. In addition, it is also found that Li isotopic compositions of these CAIs are nearly chondritic independent of their $^{10}Be/^{9}Be$ ratios. The present results can be well explained if the targets of cosmic ray irradiation are the chondritic composition; in other words, targets are most likely not CAI themselves, but their precursors of solar gases.

3.1. Introduction

Observations of solar-type young stellar objects (YSOs) have shown enhanced X-ray luminosities, ~5 orders of magnitude stronger than what the contemporary Sun emits, suggesting that solar cosmic ray irradiation also occurs on the surrounding accreting disk (e.g., Feigelson and Montmerle, 1999; Feigelson et al., 2002a; Wolk et al., 2005). In our solar system, the presence of ^{10}Be was inferred from Be-B analyses of CV CAIs. As mentioned in chapter 1, because ^{10}Be cannot be produced by thermonuclear reactions in stars, the origin of ^{10}Be was thought to be a cosmic ray irradiation caused by solar flares (e.g., McKeegan et al., 2000; Gounelle et al. 2001). Recently, however, Banerjee et al. (2016) demonstrated that ^{10}Be can be readily synthesized in low mass supernovae by neutrino spallation reaction. Furthermore, Desch et al. (2004) and Tatischeff et al. (2014) proposed models of the molecular cloud origin of ^{10}Be in the early solar system (see chapter 1), and hence, the origin of ^{10}Be in the early solar system remains controversial.

It should be noted that most of initial ^{10}Be abundances in our solar system were deduced from the Be-B analyses of CV coarse-grained CAIs (McKeegan et al., 2000; Sugiura et al., 2001; MacPherson et al., 2003; Chaussidon et al., 2006; Wielandt et al., 2012; Srinivasan & Chaussidon, 2013). Because coarse-grained CAIs are dominant mostly in CV chondrites, it is unclear whether or not coarse-grained CAIs represent the earliest stage of the evolution of the proto-solar disk. Moreover, most of CV chondrites have experienced exposure thermal and shock processes on parent bodies (Scott et al., 1992; Krot et al., 1995). Thus, some of the observed isotopic compositions would be disturbed by these secondary processes. In order to reveal the origin of ^{10}Be in the early solar system, it is important to determine the initial ^{10}Be abundances of CAIs in various types of chondrites, esp., pristine ones, to understand the distribution of ^{10}Be in the early solar system. Because CAIs in other types of chondrites show relatively small sizes, it is difficult to measure B isotopic compositions using a conventional mass spectrometer. To

overcome this problem, I developed a protocol for high accuracy and high spatial resolution measurement techniques (see chapter 2) and applied for CAIs in various types of carbonaceous chondrites.

Here, I measured Li-Be-B and Al-Mg isotopic compositions of CAIs in CO, ungrouped C, CH, and CH/CBb chondrites. CAIs in CO and ungrouped C chondrites have distinct characteristics from CV CAIs, such as types of the CAI, typical sizes, and its mineralogy (Russel et al., 1998; Scott and Krot, 2014). Therefore, these CAIs may have different information about evolution of the proto-solar disk, which will expand our knowledge about distribution of ^{10}Be in the proto-solar disk. In addition, I analyzed CAIs in the Y81020 chondrite, which is one of the least altered carbonaceous chondrite classified as CO3.05 (Grossman & Brearley, 2005; Kimura et al., 2008). Thus, Y81020 CAIs should record pristine information about proto-solar disk.

CH and CH/CBb chondrites are also the most pristine (unmetamorphosed) meteorites in our collections. CH and CH/CBb chondrites are characterized by enrichments in ^{15}N (up to 1,100‰; Murty et al., 2007; Ivanova et al., 2008; Briani et al., 2009; Bonal et al., 2010), which is similar to the characteristics of comets (Füri and Marty, 2015). In addition, Van Kooten et al. (2016) and Olsen et al. (2016) proposed that Mg and Cr isotopic compositions of bulk CH and CH/CBb chondrites require significant amounts (20-50%) of primordial molecular cloud matter in their precursor material. These observations suggest that these meteorites may have accreted a significant amount of possible outer solar system materials.

CAIs in CH and CH/CBb chondrites also have distinctive characteristics: smaller sizes than those in other chondrites (e.g., CV, CO, and CR), high abundances of refractory minerals (e.g., grossite, hibonite, gehlenitic melilite), lack of evidence of thermal and aqueous alteration on their parent bodies (Bishcoff et al., 1993; Kimura et al., 1993; Krot et al., 2002), and no excesses in ^{26}Mg decayed from ^{26}Al (Kimura et al., 1992; Weber et al., 1995; Krot et al., 2008a). Thus, CH and CH/CBb CAIs also have different information

about time and/or spatial evolution of the protosolar disk. According to the new dataset, I discuss the possible origin of ^{10}Be in the early solar system and its implication for the evolution of the protosolar disk.

3.2. Samples and methods

I studied twelve CAIs in 4 carbonaceous chondrites, Yamato 81020 (CO), Yamato 82094 (ungrouped C), SaU290 (CH), and Isheyevo (CH/CBb).

The mineralogy and major elemental abundances of the CAIs were investigated using the JEOL JXA-8530F Field Emission Electron Probe Micro Analyzer (FE-EPMA) at the Department of Earth and Planetary Science, The University of Tokyo. EPMA analyses were conducted at 15 KeV with a beam current of 12 nA, and 1 μm focused beam. Elemental abundances were obtained by using a ZAF correction.

Rare Earth Element (REE) abundances of the CAIs were investigated using the Thermo Fisher Scientific iCAP Qc ICP-MS coupled with a CETAC LSX-213 G2+ Nd:YAG LA system at the Department of Earth and Planetary Science, The University of Tokyo. The operating conditions of the instruments are listed in Table 3.1.

Table. 3.1 Instrumental operating parameteres of the LA-ICP-MS

Nd:YAG LASER	CETAC LSX-213 G2+ (CETAC, USA) equipped with an active two-volume HelEx^{TM} cell
Laser source	213 nm
Pulse width	5 ns
beam diameter	20-25 μm
Repetition rate	4 or 5 Hz
Laser He carrier gas	0.95 L min^{-1}
ICPMS	iCAP Qc (Thermo Fisher Scientific)
RF-power	1550 W
Sampling depth	4.8 mm
Cool gas (Ar)	14 L min^{-1}
Auxiliary gas (Ar)	0.8 L min^{-1}
Sample gas (Ar)	0.86 L min^{-1}
Measured isotopes (dwell time: second)	^{43}Ca (0.01s), ^{139}La (0.05s), ^{140}Ce (0.05s), ^{141}Pr (0.1s), ^{143}Nd (0.1s), ^{147}Sm (0.1s), ^{151}Eu (0.1s), ^{157}Gd (0.1s), ^{159}Tb (0.1s), ^{163}Dy (0.1s), ^{165}Ho (0.1s), ^{167}Er (0.1s), ^{169}Tm (0.1s), ^{173}Yb (0.1s), ^{175}Lu (0.1s)
Calibration standard	Glass standard reference material (NIST SRM 612)
Secondary standard	Glass standard reference material (BCR-2G)

Minerals observed in each inclusion will be sometimes abbreviated as follows:

Al-(Ti)-di: Al-(Ti)-rich diopside [$Ca(Mg, Ti, Al)(Al, Si)_2O_6$]

Di: diopside [$CaMgSi_2O_6$]

Fo: forsterite [$(Mg, Fe)_2SiO_4$]

Gro: grossite [$CaAl_4O_7$]

Hib: hibonite [$CaAl_{12}O_{19}$]

Ilm: ilmenite [$FeTiO_3$]

Mel: melilite [$Ca_2(MgSi, Al_2)SiO_7$]

Pl: plagioclase [$(Na, Ca)(Si, Al)_4O_8$]

Pv: perovskite [$CaTiO_3$]

Spi: spinel [$(Mg, Fe)Al_2O_4$]

3.2.1. CO and ungrouped C CAIs

Y81020 is known as one of the least altered carbonaceous chondrites and classified as CO3.05 (Grossman and Brearley, 2005; Kimura et al., 2008). Two CAIs in Y81020, named Y20-1X1 and Y20-9-1, were selected for investigation by LA-ICPMS and NanoSIMS measurements.

CAI Y20-1X1, ~300 × 300 μm^2 in size, has a rounded shape and consists of anhedral grains of spinel, and perovskite enclosed in melilite and Al, Ti-diopside. Melilite shows chemical zoning with increase åkermanite contents from near spinel (~$Åk_{34}$) to the CAI interior (~$Åk_{55}$) (see Table 3.2 and Fig. 3.2). The CAI is surrounded by a double-layered rim of Al-Ti-rich diopside layer and diopside layer. An object like this have been previously described from CO3s (Russel et al., 1998) and a subgroup of CO3s of Acfer 094 (Krot et al., 2004), DOM 08004, and 08006 (Simon & Grossman, 2016). They have been called type A inclusions based on the similarity of their mineralogy to that typical of compact type A inclusions in CV chondrites (Simon et al., 1999). The CAI have a modified group II REE pattern (Fig.3.3), which shows depletions of ultra-refractory HREEs with positive anomalies in Ce, Eu, and Yb

(Hiyagon et al., 2011). Major and REE element concentrations are shown in Table. 3.2 and 3.3, respectively. A BEI of Y20-1X1 is shown in Fig. 3.1. X-ray elemental maps are shown in Fig. 3.2.

Tabel 3.2. Major element concentrations of the Y20-1X1 CAI in the Y81020 (CO3.05) chondrite

Mineral	spi	mel	mel	mel	di	mel	mel	mel	mel	Al, Ti-rich di	di_rim
SIMS spots*		BeB_1	BeB_2	BeB_3	BeB_4	BeB_5	BeB_6	BeB_7	Li_1		
Na_2O	0.00	0.00	0.00	0.02	0.00	0.01	0.07	0.04	0.00	0.00	0.01
MgO	27.94	8.05	6.45	7.91	18.01	4.98	5.72	5.45	7.37	9.06	19.12
SiO_2	0.48	34.82	31.94	34.22	53.85	29.63	30.63	30.58	33.44	36.57	55.66
Al_2O_3	69.75	16.63	20.16	16.86	2.81	24.47	22.11	22.63	18.03	18.87	0.74
FeO	0.06	0.06	0.06	0.08	0.22	0.03	0.04	0.01	0.04	0.12	0.45
MnO	0.01	0.02	0.01	0.02	0.03	0.02	0.02	0.02	0.03	0.03	0.00
K_2O	0.01	0.01	0.01	0.02	0.00	0.00	0.05	0.03	0.01	0.00	0.01
CaO	0.55	40.95	40.88	40.44	25.57	40.96	39.86	40.60	41.13	25.70	24.99
TiO_2	0.31	0.04	0.05	0.26	0.46	0.01	0.25	0.17	0.07	9.45	0.15
V_2O_3	0.38	0.00	0.01	0.00	0.04	0.02	0.02	0.01	0.01	0.20	0.01
Cr_2O_3	0.27	0.01	0.00	0.00	0.08	0.00	0.03	0.00	0.01	0.04	0.05
NiO	0.03	0.02	0.03	0.01	0.04	0.02	0.00	0.00	0.00	0.05	0.02
Total	99.78	100.61	99.60	99.84	101.11	100.15	98.80	99.55	100.13	100.08	101.21
No. of analyses	3	2	2	3	3	3	1	2	2	1	1
Ak#		55	45	54		34	40	38	51		

* EPMA measurements were performed near analysis spots of Be-B and Li isotopes.

Tabel 3.3. Rare earth element concentrations of the Y20-1X1 CAI in the Y81020 (CO3.05) chondrite

	mel			pv + Al-Ti-di + mel		
	ppm		1SD	ppm		1SD
La	0.447	±	0.291	7.747	±	1.395
Ce	1.726	±	0.535	45.521	±	6.226
Pr	0.160	±	0.081	4.682	±	0.774
Nd	0.493	±	0.356	17.068	±	2.621
Sm	0.252	±	0.236	9.398	±	2.158
Eu	2.105	±	0.302	2.514	±	0.307
Gd	0.067	±	0.121	0.925	±	0.383
Tb	0.010	±	0.017	0.163	±	0.082
Dy	0.029	±	0.050	0.983	±	0.216
Ho	0.002	±	0.008	0.126	±	0.058
Er	0.005	±	0.022	0.379	±	0.199
Tm	0.008	±	0.010	0.754	±	0.169
Yb	0.365	±	0.218	18.513	±	3.285
Lu	0.005	±	0.012	0.062	±	0.029

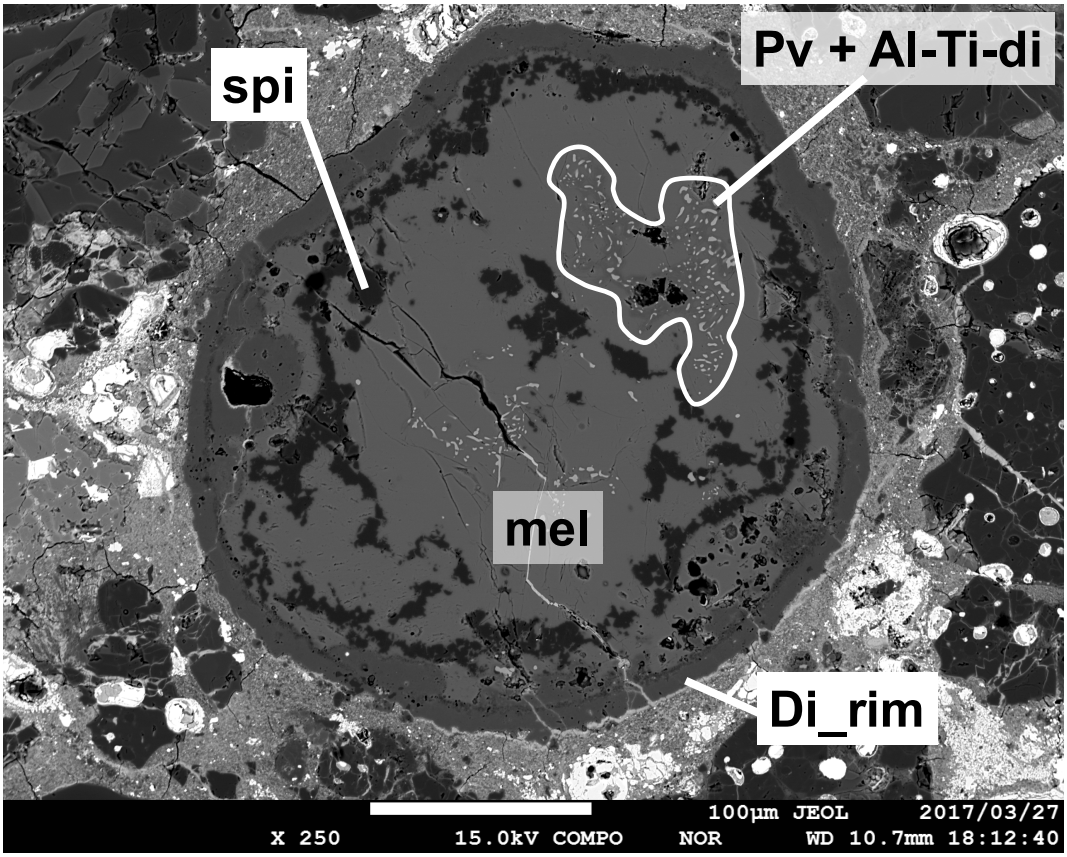

Fig. 3.1. A BEI of the CAI Y20-1X1 in the Y81020 (CO3.05) chondrite. It consists of anhedral grains of spinel, and perovskite enclosed in melilite and Al, Ti-diopside. Secondary minerals (e.g., nepheline, sodalite) are absent.

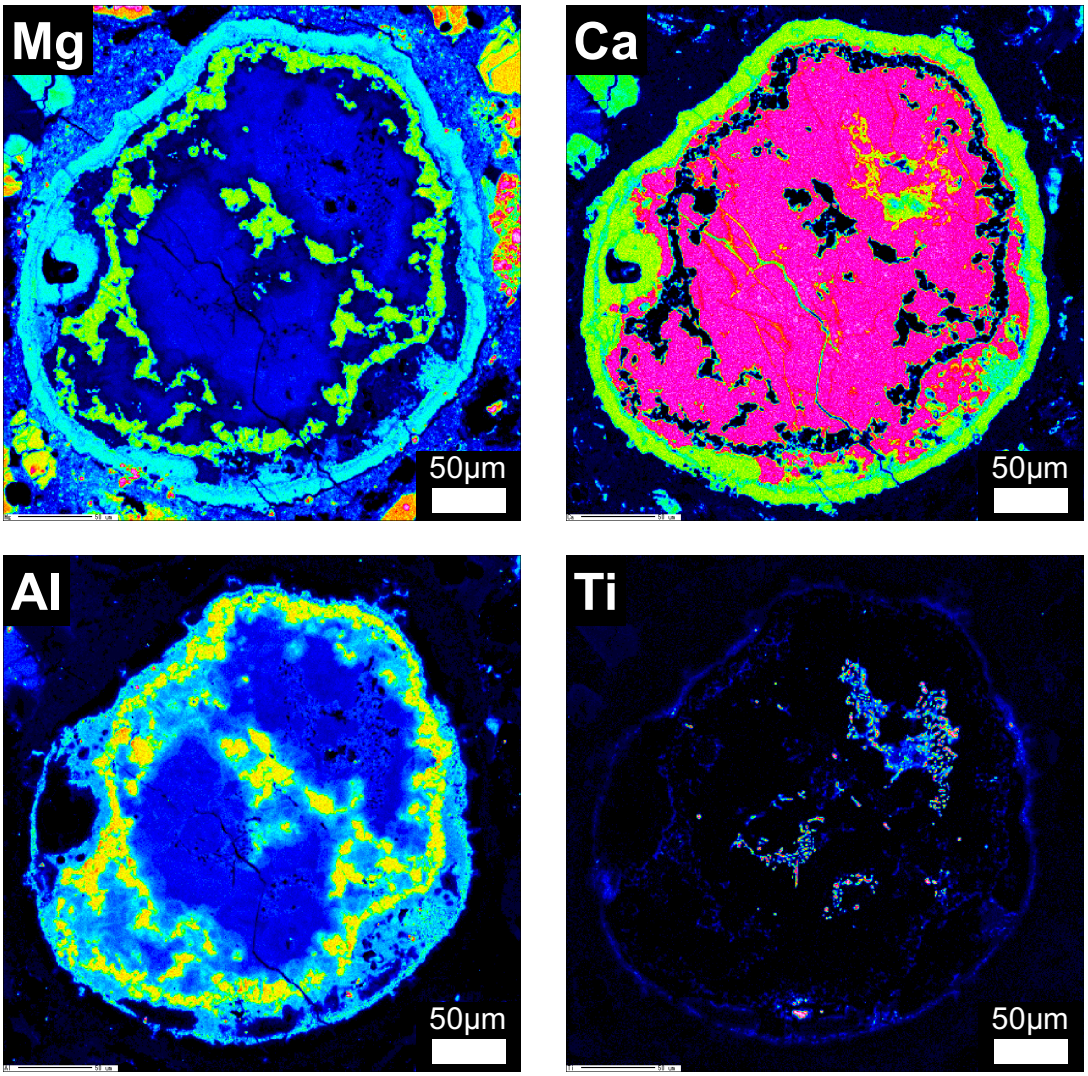

Fig. 3.2. X-ray elemental maps in Mg, Ca, Al, and Ti of the CAI Y20-1X1 in the Y81020 (CO3.05) chondrite. Melilite shows chemical zoning with increase åkermanite contents from near spinel (~$Åk_{34}$) to the CAI interior (~$Åk_{55}$).

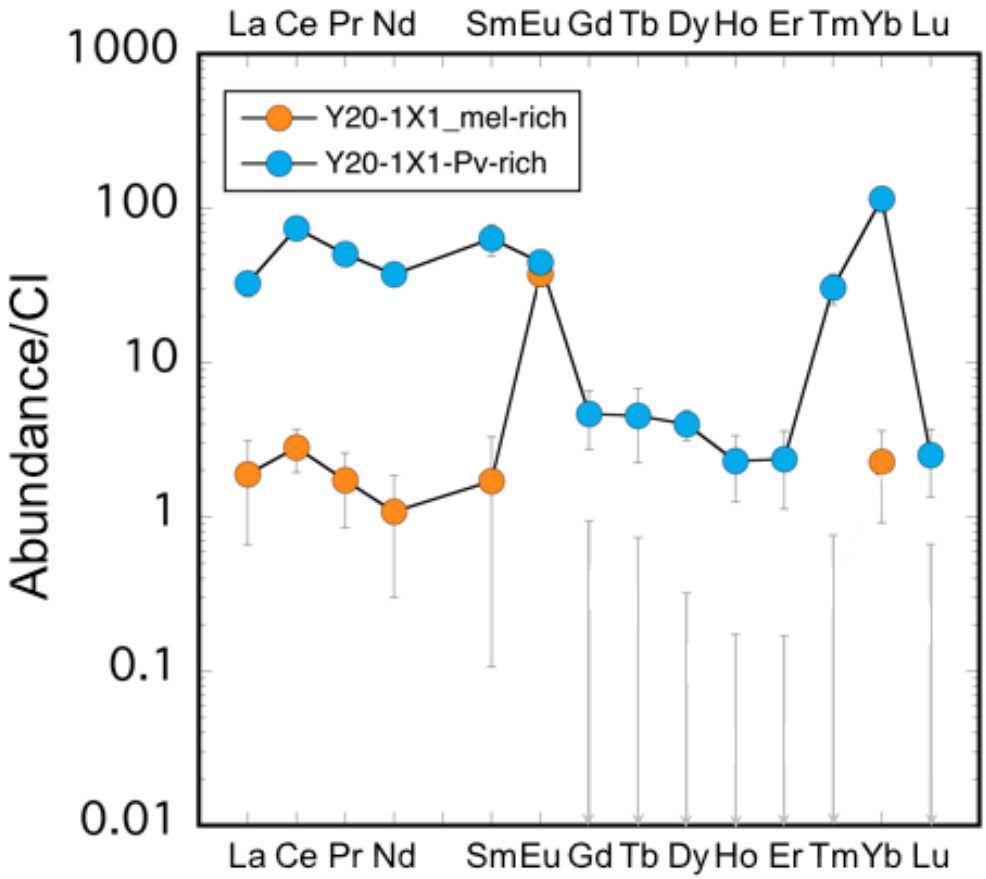

Fig. 3.3. CI-normalized abundances of REEs in the CAI Y20-1X1 in the Y81020 (CO3.05) chondrite. Because Gd to Tm, and Lu data of mel-rich region show large errors due to low concentrations, only upper limits are shown. Both of mel-rich and pv-rich region show modified group II patterns, suggesting that precursor materials have condensed from the HREE depleted solar nebula. The differences in absolute concentrations would reflect the differences in partition coefficients and would be produced by melting events.

CAI Y20-9-1 is a fragment of a melilite rich CAI. It consists of gehlenitic melilite ($Åk_{4\text{-}11}$) and minor anhedral grains of spinel and perovskite. Anhedral spinel grains are concentrated near the CAI edge. Melilite near the rim shows more gehlenitic compositions ($Åk_{4\text{-}5}$) than that of the CAI interior ($Åk_{7\text{-}11}$). There are several voids in melilite, and perovskite commonly occurs around these voids (Fig. 3.5). The CAI is surrounded by a double-layered rim of discontinuous spinel layer and Al, Ti-rich

diopside layer. The CAI have a modified group II REE pattern (Fig.3.6). The mineralogy and texture of this CAI are very similar to the Acfer 094 CAI G104 reported in Ushikubo et al. (2017). Major and REE element concentrations are shown in Tables 3.4 and 3.5, respectively. A BEI of Y20-90-1 is shown in Fig. 3.4. X-ray elemental maps are shown in Fig. 3.5.

Tabel 3.4. Major elment concentrations of the Y20-9-1 CAI in the Y81020 (CO3.05) chondrite

Mineral	mel	pv	spi	Al-Ti-rich di	di_rim
Na_2O	0.00	0.00	0.04	0.00	0.00
MgO	1.03	0.41	28.33	9.64	16.38
SiO_2	23.22	0.62	0.06	29.34	50.35
Al_2O_3	33.77	1.24	70.08	26.95	5.59
FeO	0.08	0.28	0.14	0.35	0.36
MnO	0.01	0.04	0.02	0.00	0.03
K_2O	0.00	0.00	0.01	0.00	0.01
CaO	40.99	40.23	0.37	21.77	25.19
TiO_2	0.36	56.79	0.28	11.48	2.42
V_2O_3	0.01	0.40	0.33	0.64	0.13
Cr_2O_3	0.01	0.06	0.13	0.08	0.00
NiO	0.02	0.05	0.00	0.05	0.00
Total	99.51	100.13	99.78	100.31	100.45
No. of analyses	75	1	1	1	1
Ak#	7				

Tabel 3.5. Rare earth elment concentrations of the Y20-9-1 CAI in the Y81020 (CO3.05) chondrite

	mel_3			mel_4		
	ppm		1SD	ppm		1SD
La	5.361	±	1.818	5.023	±	2.167
Ce	31.044	±	12.845	26.400	±	10.879
Pr	2.588	±	1.049	2.398	±	1.050
Nd	9.844	±	3.517	9.044	±	3.732
Sm	4.589	±	2.347	4.087	±	2.079
Eu	2.475	±	0.520	2.169	±	0.488
Gd	1.702	±	0.773	1.390	±	0.690
Tb	0.274	±	0.125	0.226	±	0.119
Dy	1.879	±	0.976	1.783	±	1.041
Ho	0.191	±	0.137	0.190	±	0.145
Er	0.484	±	0.293	0.630	±	0.504
Tm	0.626	±	0.333	0.632	±	0.401
Yb	13.487	±	6.026	11.941	±	4.250
Lu	0.084	±	0.060	0.076	±	0.066

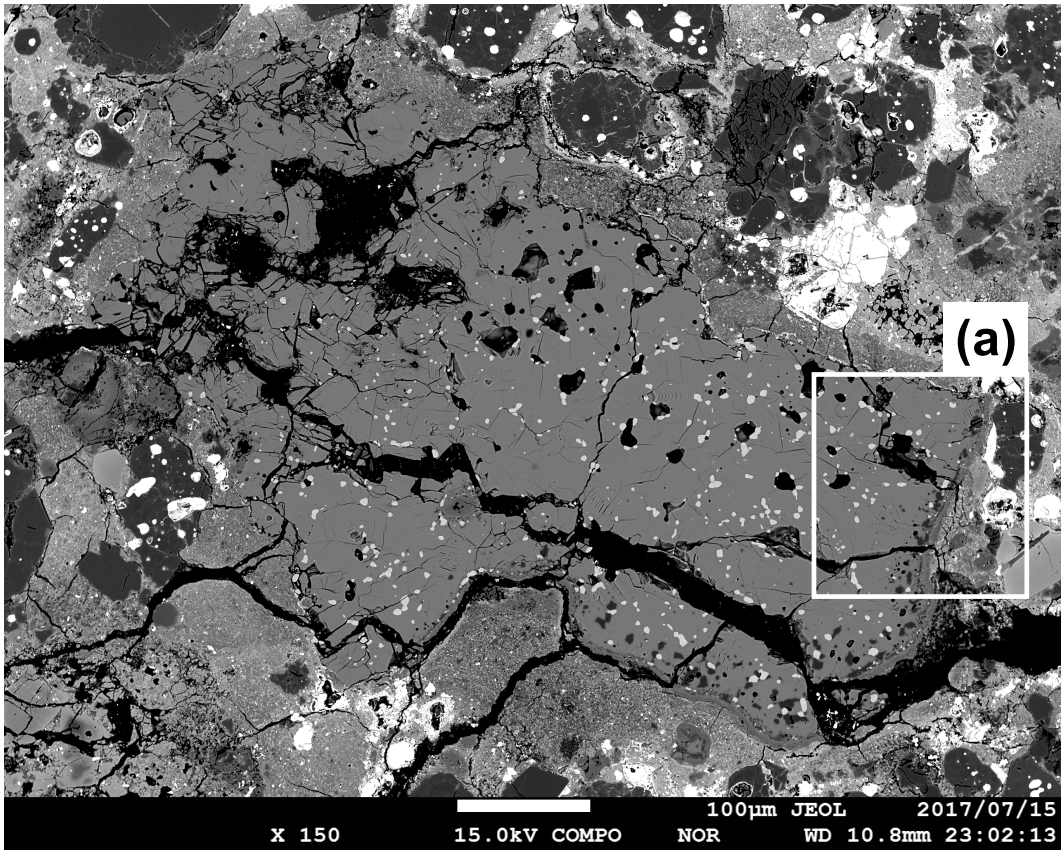

Fig. 3.4. A BEI of the CAI Y20-9-1 in the Y81020 (CO3.05) chondrite. X-ray mapping of a region outlined is shown in Fig. 3.5 (a). It consists of gehlenitic melilite ($Åk_{4\text{-}11}$) and minor anhedral grains of spinel and perovskite. Secondary minerals (e.g., nepheline, sodalite) are absent.

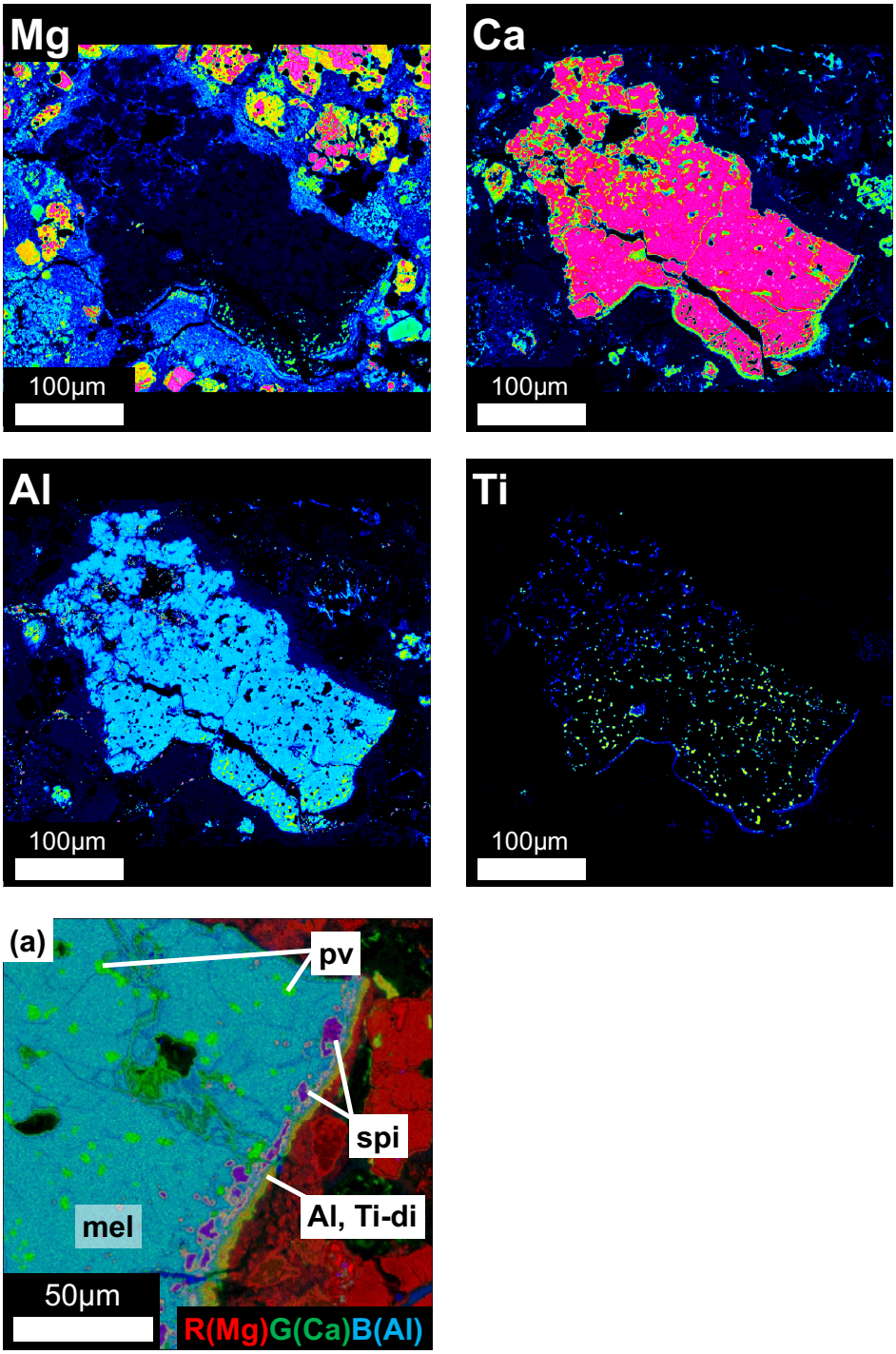

Fig. 3.5. X-ray elemental maps in Mg, Ca, Al, and Ti and (a) a combined X-ray elemental map of the CAI Y20-9-1 in the Y81020 (CO3.05) chondrite.

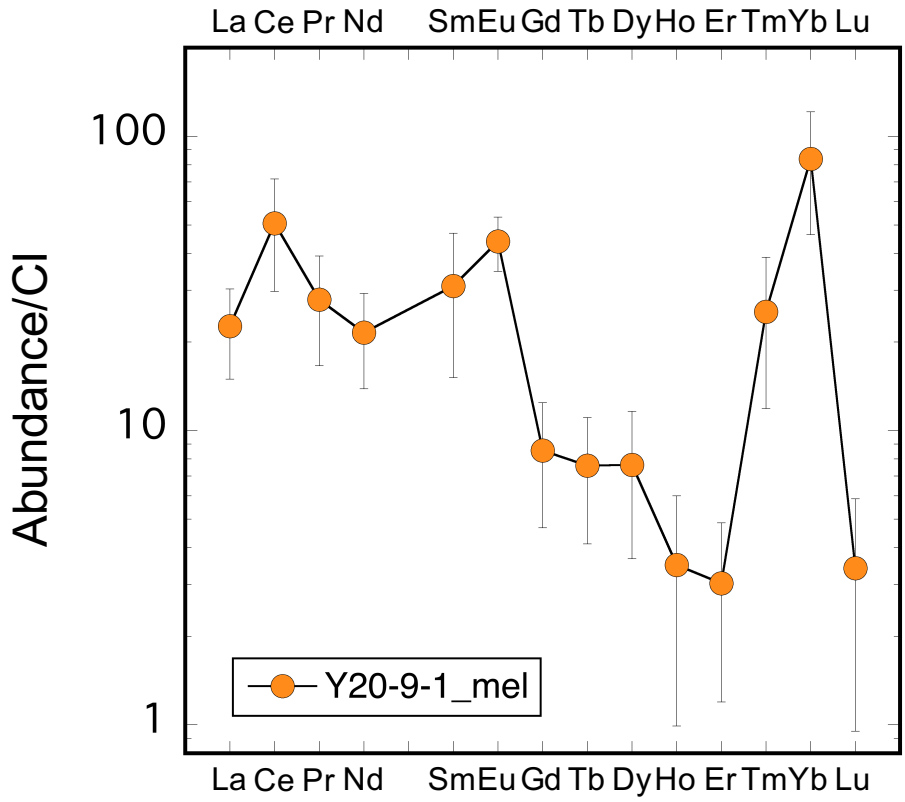

Fig. 3.6. CI-normalized abundances of REEs in the CAI Y20-9-1 in the Y81020 (CO3.05) chondrite. Melilites show modified group II patterns.

Y82094 was originally classified as a CO chondrite (Yanai and Kojima, 1987). However, recent detailed observation and the bulk chemical composition of Y82094 revealed that this meteorite is an ungrouped C chondrite with petrologic type of 3.2 (Kimura et al., 2014). Two CAIs in Y82094, Y94-42C5 and Y94-42C7, were selected for investigation by LA-ICPMS and NanoSIMS measurements.

CAI Y94-42C5 is a fragment of a melilite-rich CAI. It consists of gehlenitic melilite ($Åk_{4-6}$), hibonite, and minor subhedral grains of spinel. Secondary minerals, such as Fe-rich spinel, ilmenite, and Al-rich silicate, were also identified. The Al-rich silicate are commonly in contact with melilite and likey formed by replacement of this phase (Fig. 3.7). The CAI is surrounded by a diopside rim. The CAI have a ultra-refractory REE pattern (Fig. 3.9), indicating that a precursor of this CAI would have experienced high temperature gas/solid separation processes (e.g., Hiyagon et al., 2003). Major and REE element concentrations are shown in Tables 3.6 and 3.7, respectively. A BEI of Y94-42C5 is shown in Fig. 3.7. X-ray elemental maps are shown in Fig. 3.8.

Tabel 3.6. Major elment concentrations of the Y94-42C5 CAI in the Y82094 (ungrouped C3.2) chondrite

Mineral	mel	hib	spi	Fe-spi	ilm	Al-rich silicate	di_rim
Na_2O	0.02	0.02	0.00	0.03	0.00	5.38	0.01
MgO	0.67	2.90	27.57	19.43	3.19	5.59	19.03
SiO_2	22.44	0.17	0.27	0.05	0.07	26.38	52.70
Al_2O_3	34.69	80.76	69.48	65.92	0.19	42.19	2.77
FeO	0.40	0.32	0.91	12.14	40.65	9.37	1.12
MnO	0.03	0.00	0.00	0.04	0.52	0.02	0.01
K_2O	0.01	0.01	0.00	0.01	0.01	0.71	0.00
CaO	40.86	8.50	0.33	0.17	0.90	3.86	24.27
TiO_2	0.09	5.38	0.30	0.17	49.34	0.23	0.64
V_2O_3	0.03	0.61	0.07	0.36	0.39	0.04	0.06
Cr_2O_3	0.01	0.08	0.14	0.09	0.02	0.03	0.04
NiO	0.03	0.03	0.03	0.03	0.04	0.29	0.05
Total	99.29	98.78	99.09	98.43	95.32	94.10	100.70
No. of analyses	4	1	1	3	2	2	2
Ak#	5						
Comment						alteration of mel?	

Tabel 3.7. Rare earth elment concentrations of the Y94-42C5 CAI in the Y82094 (ungrouped C3.2) chondrite

	position_1 (mainly mel)			position_2 (mainly mel)		
	ppm		1SD	ppm		1SD
La	34.3	±	3.9	25.9	±	6.8
Ce	124.5	±	12.7	98.0	±	23.6
Pr	14.1	±	1.3	10.2	±	2.2
Nd	72.4	±	10.4	47.7	±	13.7
Sm	27.1	±	6.7	16.0	±	3.9
Eu	1.1	±	0.3	2.3	±	0.7
Gd	101.7	±	18.5	50.6	±	12.3
Tb	21.1	±	3.8	10.6	±	2.4
Dy	197.5	±	35.9	93.0	±	21.3
Ho	94.0	±	16.3	43.8	±	10.0
Er	374.9	±	69.7	173.1	±	38.1
Tm	7.9	±	1.4	3.8	±	0.9
Yb	54.1	±	8.3	27.8	±	5.1
Lu	59.8	±	10.0	28.3	±	5.6

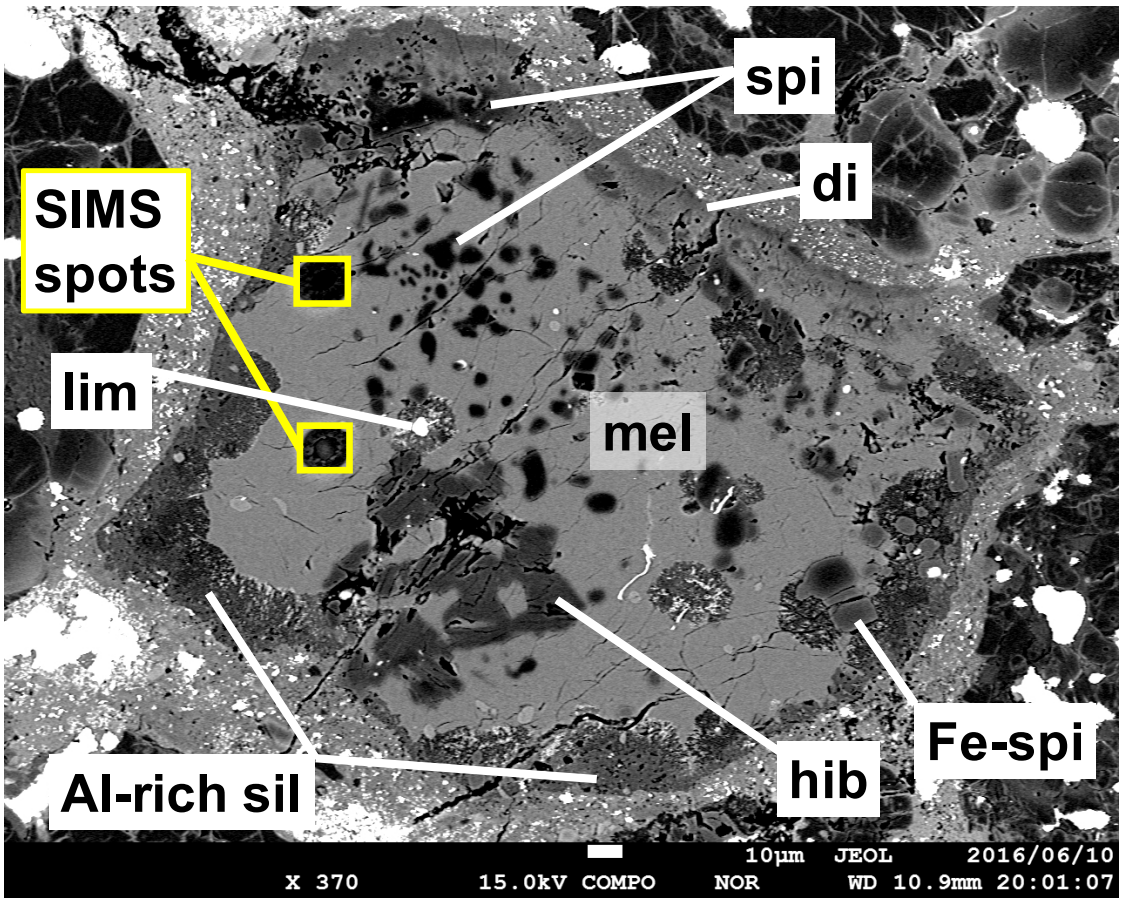

Fig. 3.7. A BEI of the CAI Y94-42C5 in the Y82094 (ungrouped C3.2) chondrite. It consists of gehlenitic melilite ($Åk_{4-6}$), hibonite, and minor subhedral grains of spinel. Secondary minerals, such as Fe-rich spinel, ilmenite, and Al-rich silicate, were also identified.

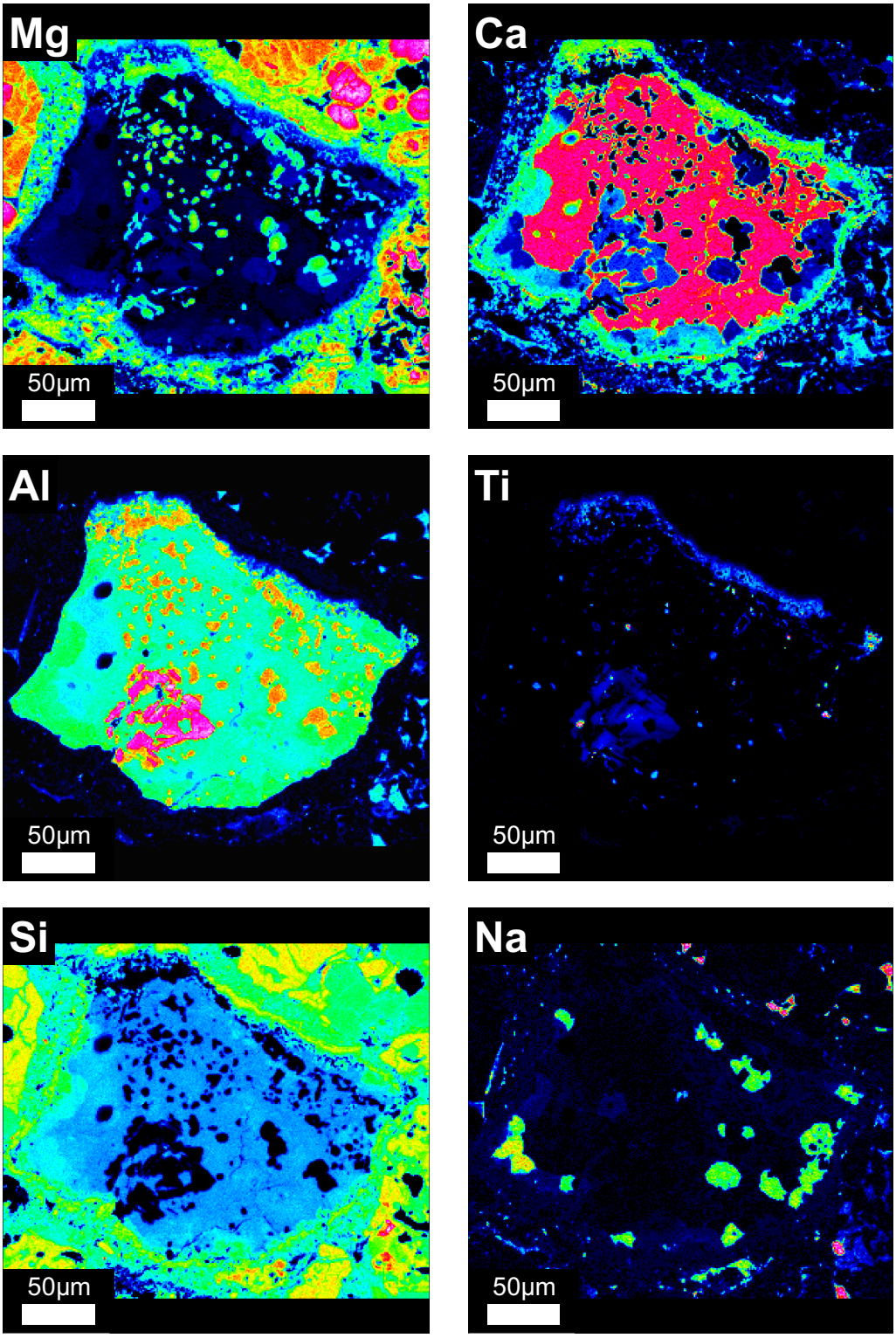

Fig. 3.8. X-ray elemental maps in Mg, Ca, Al, Ti, Si, and Na of the CAI Y94-42C5 in the Y82094 (ungrouped C3.2) chondrite.

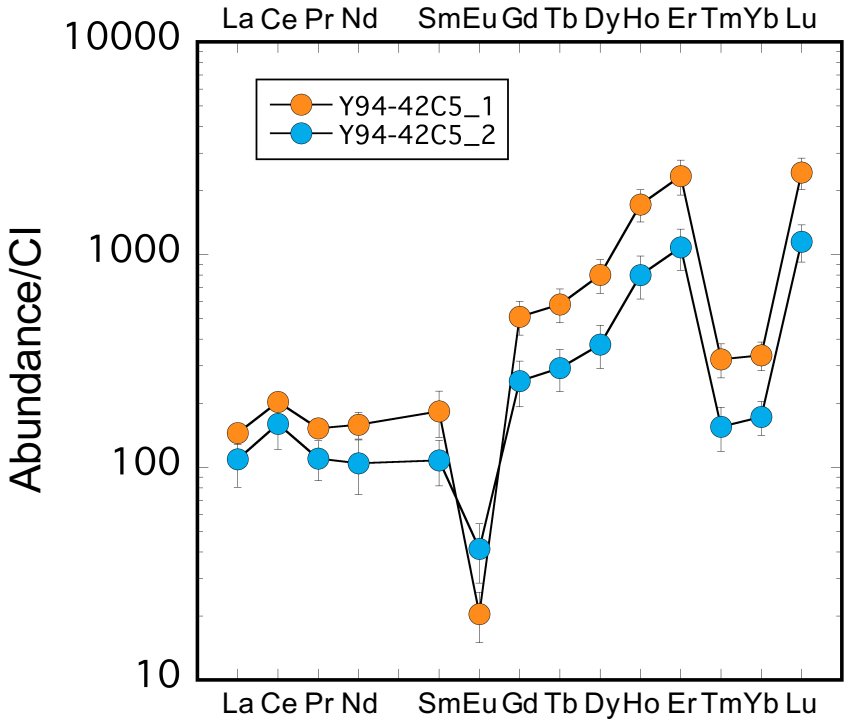

Fig. 3.9. CI-normalized abundances of REEs in the CAI Y94-42C5 in the Y82094 (ungrouped C3.2) chondrite. The CAI shows ultra-refractory REE patterns.

CAI Y94-42C7 is a fragment of a melilite-rich CAI. It consists of melilite ($Åk_{14-21}$), perovskite, plagioclase, pyroxene, and Al-rich silicate. The Al-rich silicates are commonly in contact with melilite and likey formed by replacement of this phase (Fig. 3.10 a). Plagioclase and pyroxene occur only in the alteration region so that these minerals would be secondary products by parent body alterations (Fig. 3.10 b). Melilites show an equilibrium texture with typical 120° triple junctions (Fig. 3.10 c). This feature indicates that CAI Y94-42C7 formed by aggregation of individual melilite grains and subsequent high-temperature annealing (Greshake et al., 1998; Simon et al., 1999; Han & Brearley, 2017). The CAI have a modified group II REE pattern (Fig.3.11). Major and REE element concentrations are shown in Tables 3.8 and 3.9, respectively. BEIs of Y94-42C5 is shown in Fig. 3.10 a-c.

Tabel 3.8. Major elment concentrations of the Y94-42C7 CAI in the Y82094 (ungrouped C3.2) chondrite

Mineral	mel	pv	pl	pyroxene	Al-rich silicate
Na_2O	0.05	0.00	0.82	0.34	0.52
MgO	2.61	0.12	0.24	11.71	3.03
SiO_2	25.79	0.15	43.27	50.07	31.81
Al_2O_3	29.76	0.25	34.58	3.04	38.07
FeO	0.37	2.10	1.55	10.26	4.97
MnO	0.02	0.04	0.03	0.06	0.00
K_2O	0.00	0.00	0.04	0.03	0.05
CaO	41.06	39.56	18.34	23.25	16.35
TiO_2	0.05	58.84	0.06	0.04	0.22
V_2O_3	0.00	0.54	0.02	0.01	0.00
Cr_2O_3	0.03	0.02	0.00	0.12	0.02
NiO	0.03	0.02	0.32	0.02	0.47
Total	99.77	101.64	99.27	98.94	95.51
No. of analyses	4	1	1	1	2
Ak#	18				
Comment					alteration of mel?

Tabel 3.9. Rare earth elment concentrations of the Y94-42C7 CAI in the Y82094 (ungrouped C3.2) chondrite

	mel		
	ppm		1SD
La	12.54	±	4.89
Ce	37.21	±	13.98
Pr	5.21	±	2.07
Nd	24.24	±	10.05
Sm	7.46	±	3.12
Eu	2.12	±	0.25
Gd	1.95	±	0.98
Tb	0.30	±	0.14
Dy	1.44	±	0.66
Ho	0.13	±	0.08
Er	0.22	±	0.15
Tm	0.64	±	0.31
Yb	7.58	±	3.27
Lu	0.04	±	0.04

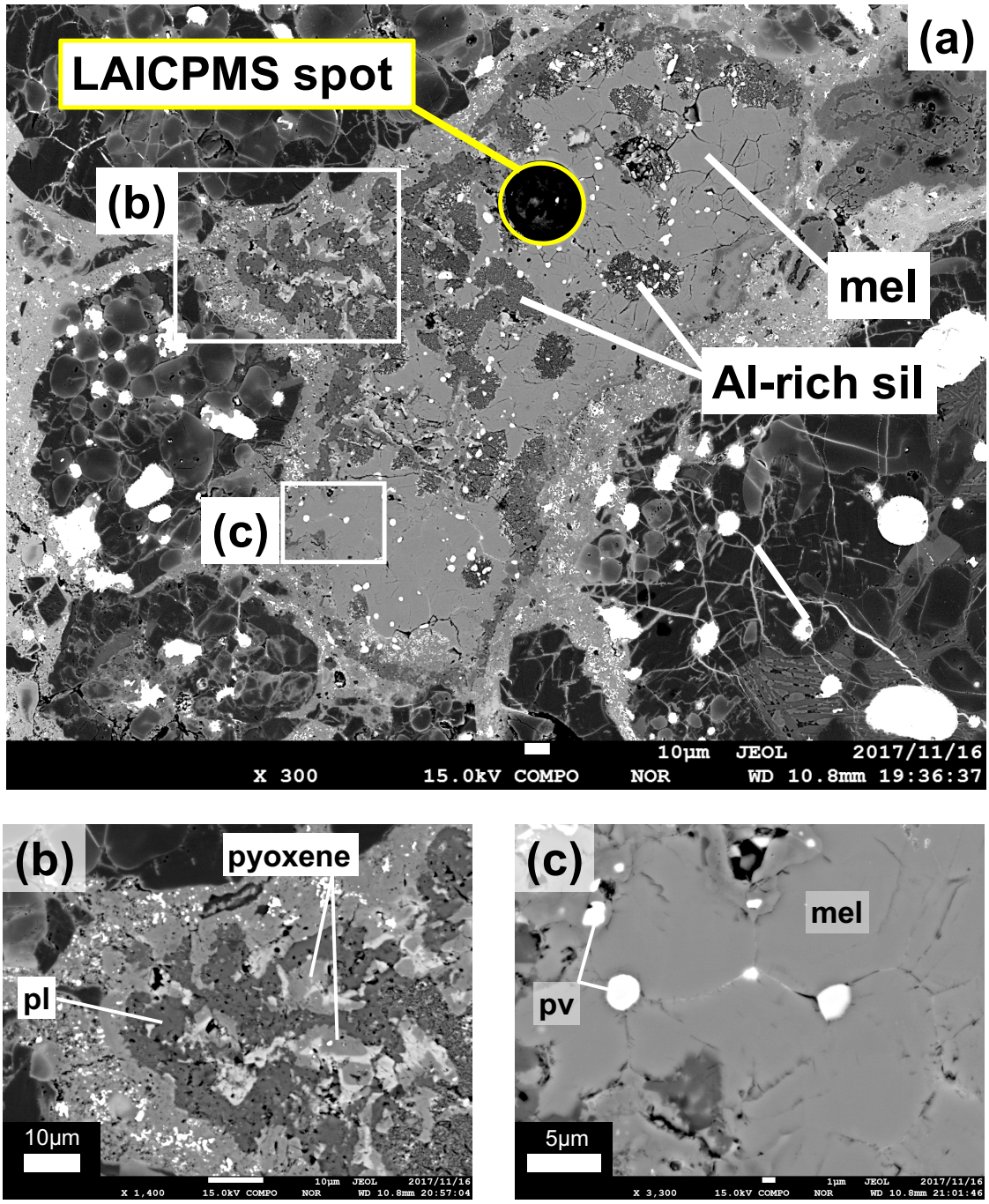

Fig. 3.10. (a) A BEI of the CAI Y94-42C7 in the Y82094 (ungrouped C3.2) chondrite. It consists of melilite ($Åk_{14-21}$), perovskite, plagioclase, pyroxene, and Al-rich silicate. Regions outlined in (a) are shown in detail in (b) and (c). (b) Plagioclase and Fe pyroxene occur in the outer portion of the CAI, suggesting that they are products by parent body alteration. (c) Some melilite grains have triple junctions.

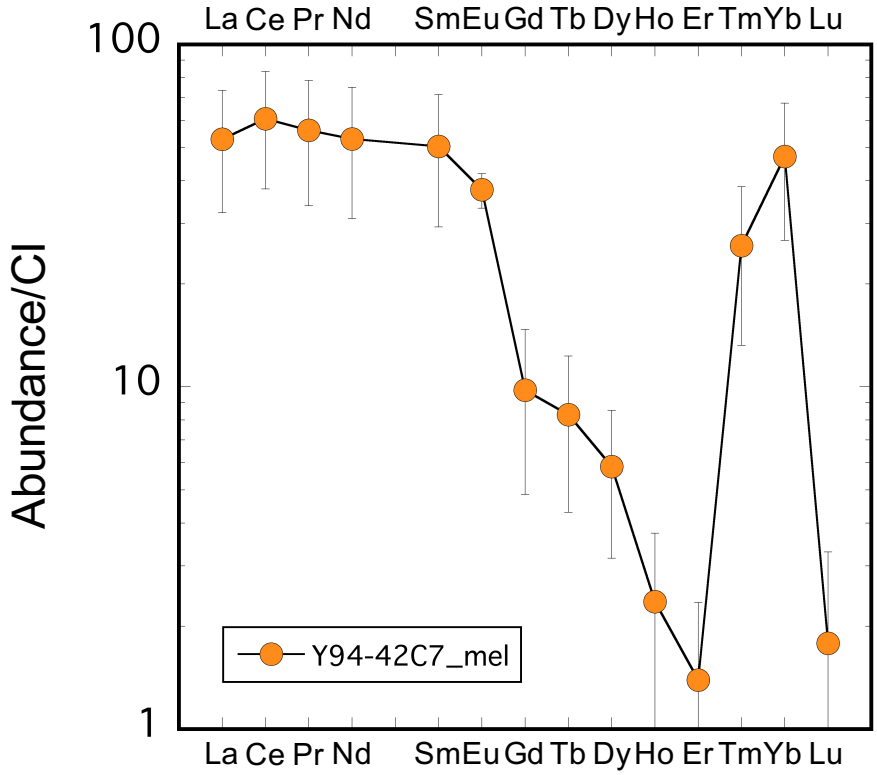

Fig.3.11. CI-normalized abundances of REEs in the CAI Y94-42C7 in the Y82094 (ungrouped C3.2) chondrite. Melilite in the CAI shows modified group II REE patterns.

3.2.2. CH and CH/CBb CAIs

Sayh al Uhaymir (SaU) 290 is classified as a CH3 carbonaceous chondrite based on its petrology, bulk chemistry, oxygen isotopes, and heavy $\delta^{15}N$ value (Murty et al., 2007). CAIs were identified in polished thick sections of the SaU290 and Isheyevo chondrites using X-ray elemental mapping with the FE-EPMA at the University of Tokyo. The 43 of SaU290 and 5 of Isheyevo thick sections were mapped in Mg, Ca, Al, Ti, and Fe X-rays using a 5 μm electron beam, 15 keV accelerating voltage, 80 nA beam current, 5 ms per pixel acquisition time, and resolution of 5 μm per pixel with Wavelength

Dispersive Spectrometer (WDS) detectors. Seven CAIs in SaU290 and one CAI in Isheyevo were selected for SIMS measurements with the aid of Al and Ca X-ray maps. ISC 103 is from Isheyevo and the others are from SaU290.

CAI ISC103 consists mostly of melilite, minor spinel and Al-Ti-rich diopside. The CAI is surrounded by a rim composed of three layers (from inside to outward): discontinuous spinel → Al-diopside → forsterite (Fig. 3.12 and 3.13). Major element concentrations are shown in Tables 3.10. BEIs of ISC103 are shown in Fig. 3.12 a-b. X-ray elemental maps are shown in fig. 3.13.

Tabel 3.10. Major elment concentrations of the ISC103 CAI in the Isheyevo (CH/CBb) chondrite

Mineral	mel	Al-Ti-rich di	spi	di_rim	fo_rim
Na_2O	0.00	0.00	0.01	0.00	0.00
MgO	0.70	7.00	28.41	17.75	56.39
SiO_2	22.90	34.42	0.06	53.25	42.39
Al_2O_3	34.85	23.63	70.78	3.83	0.16
FeO	0.29	0.28	0.41	0.86	0.87
MnO	0.00	0.03	0.05	0.03	0.01
K_2O	0.00	0.00	0.00	0.02	0.00
CaO	40.89	24.95	0.21	25.12	0.76
TiO_2	0.12	10.02	0.50	0.13	0.00
V_2O_3	n.m.**	0.11	0.22	0.18	0.06
Cr_2O_3	0.04	0.02	0.13	0.04	0.07
NiO	0.04	0.03	0.00	0.03	0.01
Total	99.83	100.48	100.78	101.24	100.72
No. of analyses	4	2	1	1	1
Ak#	5				

** Not measured

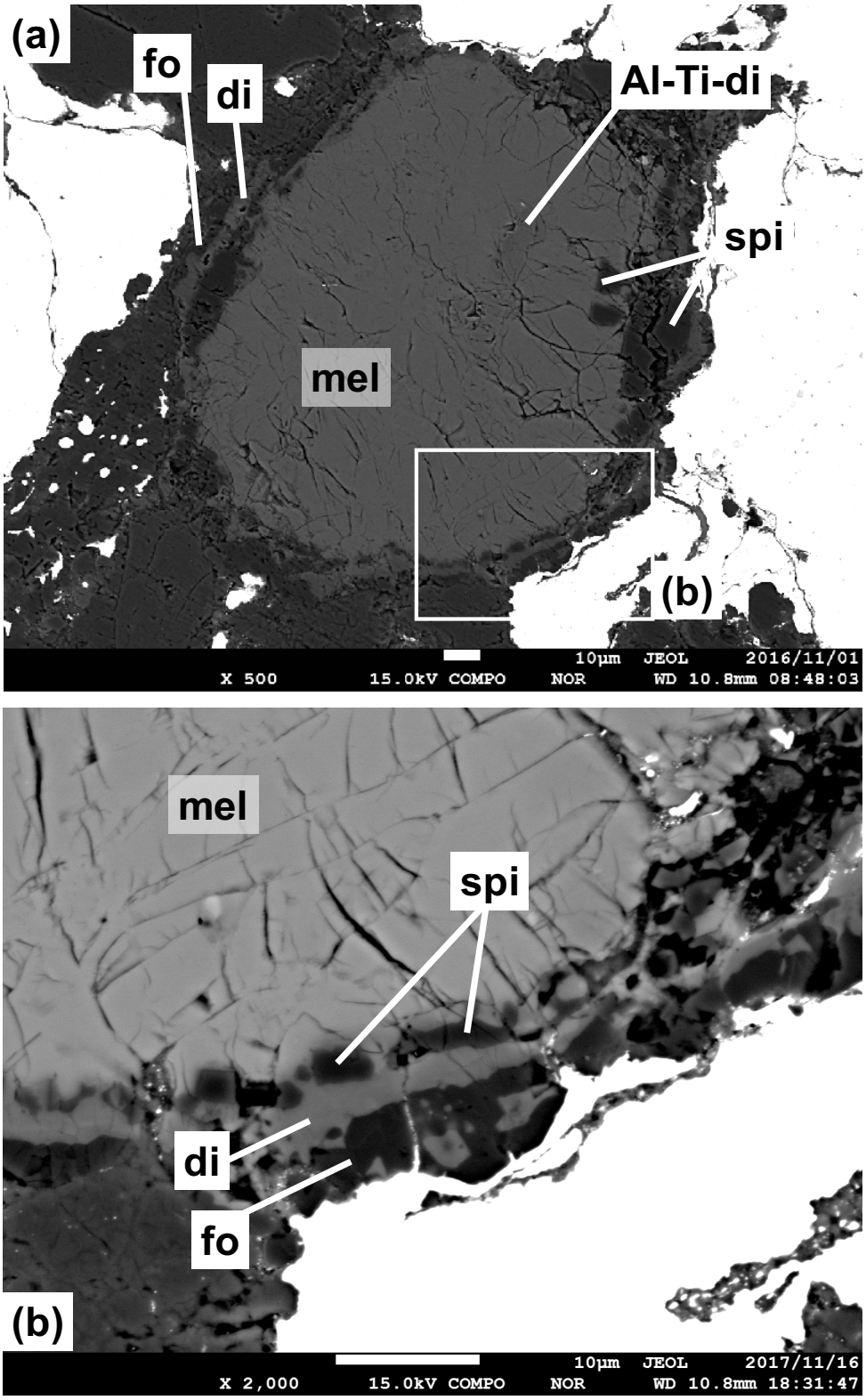

Fig. 3.12. (a) A BEI of the CAI ISC103 in the Isheyevo (CH/CBb) chondrite. It consists mostly of melilite, minor spinel and Al-Ti-rich diopside. Regions outlined in (a) are

shown in detail in (b). (b) The CAI is surrounded by a multi-layered rim (spinel → Al-diopside → forsterite).

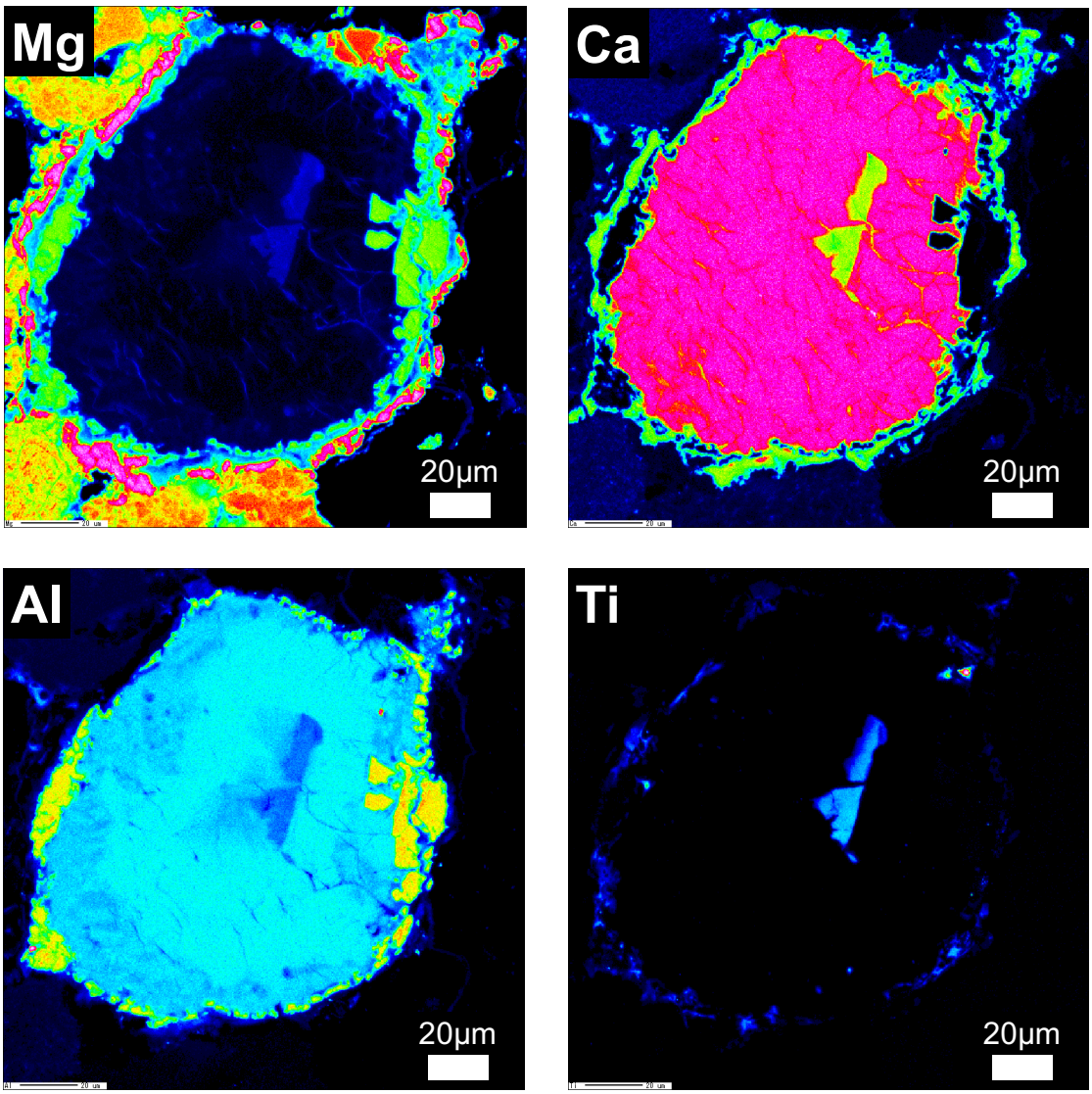

Fig. 3.13. X-ray elemental maps in Mg, Ca, Al, and Ti of the CAI ISC103 in the Isheyevo (CH/CBb) chondrite.

CAI SA201 is round and ~80 μm in diameter. It consists mostly of gehlenitic melilite ($Åk_{3-5}$), spinel, hibonite, and V-rich perovskite (V_2O_3 ~1.7 wt%). The CAI is

surrounded by a thin (< 1μm) rim of Al-Ti-rich diopside (see Fig. 3.15). The diopside rim is too small for quantitative electron microprobe analysis, and was identified only by energy dispersive spectrometer (EDS). Major element concentrations are shown in Table. 3.11. A BEI of SA201 is shown in Fig. 3.14. X-ray elemental maps are shown in Fig. 3.15.

Tabel 3.11. Major elment concentrations of the SA201 CAI in the SaU290 (CH3) chondrite

Mineral	hib	spi	mel	pv
Na_2O	0.00	0.02	0.00	0.02
MgO	0.92	28.08	0.63	0.04
SiO_2	0.07	0.14	22.82	2.20
Al_2O_3	88.00	69.96	35.17	1.13
FeO	0.37	0.93	0.58	0.81
MnO	0.01	0.03	0.02	0.04
K_2O	0.00	0.01	0.01	0.01
CaO	8.77	0.27	41.09	41.92
TiO_2	1.83	0.76	0.10	53.33
V_2O_3	0.16	0.42	0.01	1.74
Cr_2O_3	0.03	0.07	0.02	0.08
NiO	0.03	0.06	0.03	0.06
Total	100.14	101.07	100.68	101.38
No. of analyses	3	2	6	3
Ak#			4	
Comment				V-rich

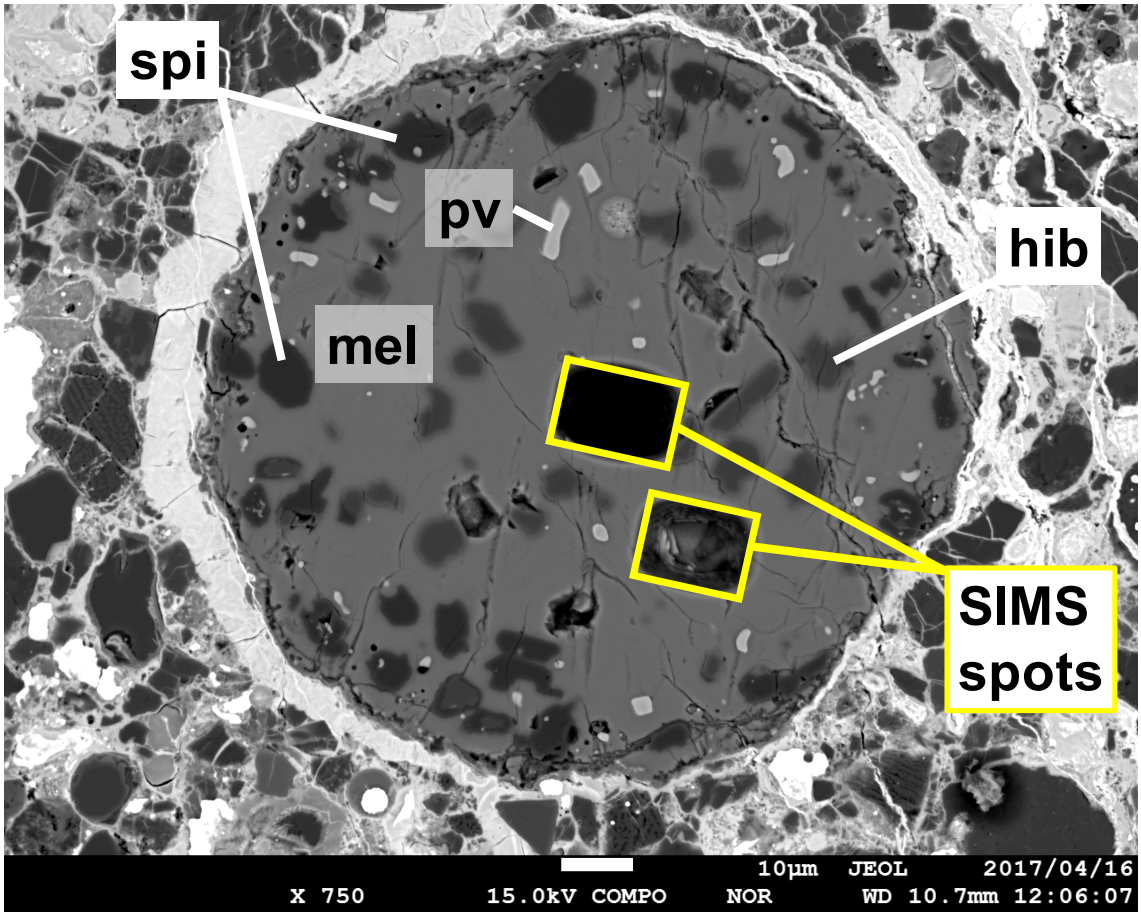

Fig. 3.14. A BEI of the CAI SA201 in the SaU290 (CH3) chondrite. It consists mostly of gehlenitic melilite ($Åk_{3\text{-}5}$), spinel, hibonite, and perovskite.

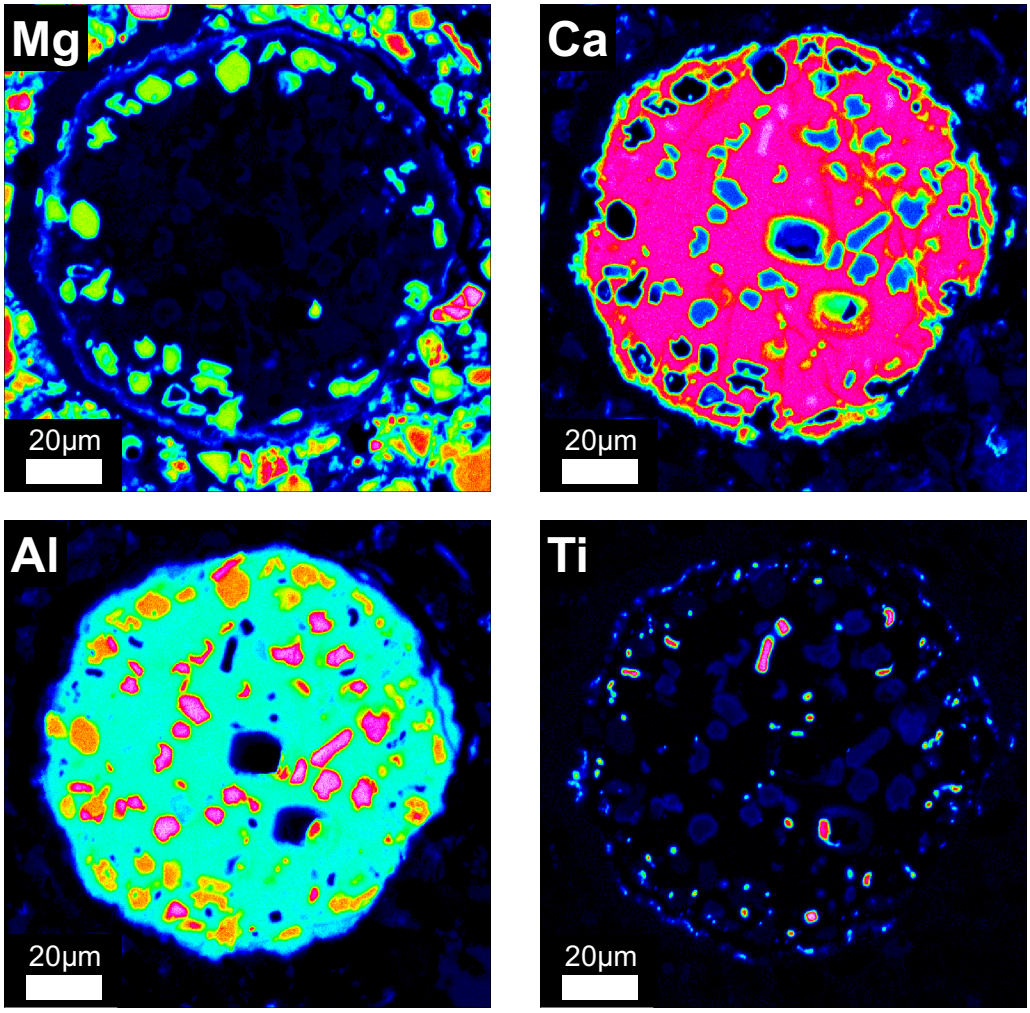

Fig. 3.15. X-ray elemental maps in Mg, Ca, Al, and Ti of the CAI SA201 in the SaU290 (CH3) chondrite. The CAI is surrounded by a thin (< 1μm) rim of Al-Ti-rich diopside. Central dark areas in Al and Ca maps correspond SIMS pits.

CAI SB202 is round and ~100 μm in diameter. It consists mostly of gehlenitic melilite ($Åk_{5-9}$), grossite, spinel, and perovskite. The CAI is surrounded by a rim composed of three layers (from inside to outward): a discontinuous spinel-diopside layer → melilite → Al-diopside (Fig. 3.18). Major element concentrations are shown in Table. 3.12. A BEI of SB202 is shown in Fig. 3.16. X-ray elemental maps are shown in Figs. 3.17 and 3.18.

Tabel 3.12. Major elment concentrations of the SA202 CAI in the SaU290 (CH3) chondrite

Mineral	mel_core	mel_rim	gro	spi	pv	di_rim
Na_2O	0.00	0.00	0.00	0.00	0.00	0.00
MgO	0.59	1.44	0.08	23.77	0.01	17.11
SiO_2	22.87	24.06	0.10	0.18	0.20	51.47
Al_2O_3	35.06	33.18	76.92	71.84	0.82	2.50
FeO	0.51	0.80	0.40	0.31	0.42	2.63
MnO	0.00	0.01	0.00	0.00	0.03	0.00
K_2O	0.00	0.00	0.01	0.02	0.00	0.00
CaO	41.07	41.00	21.24	2.99	41.58	24.18
TiO_2	0.07	0.09	0.32	0.15	56.96	0.05
V_2O_3	n.m.**	n.m.**	n.m.**	n.m.**	0.64	0.00
Cr_2O_3	0.04	0.03	0.05	0.10	0.00	0.03
NiO	0.04	0.06	0.03	0.01	0.03	0.07
Total	100.26	100.68	99.15	99.37	100.68	98.02
No. of analyses	4	3	3	1	1	1
Ak#	4	10				

** Not measured

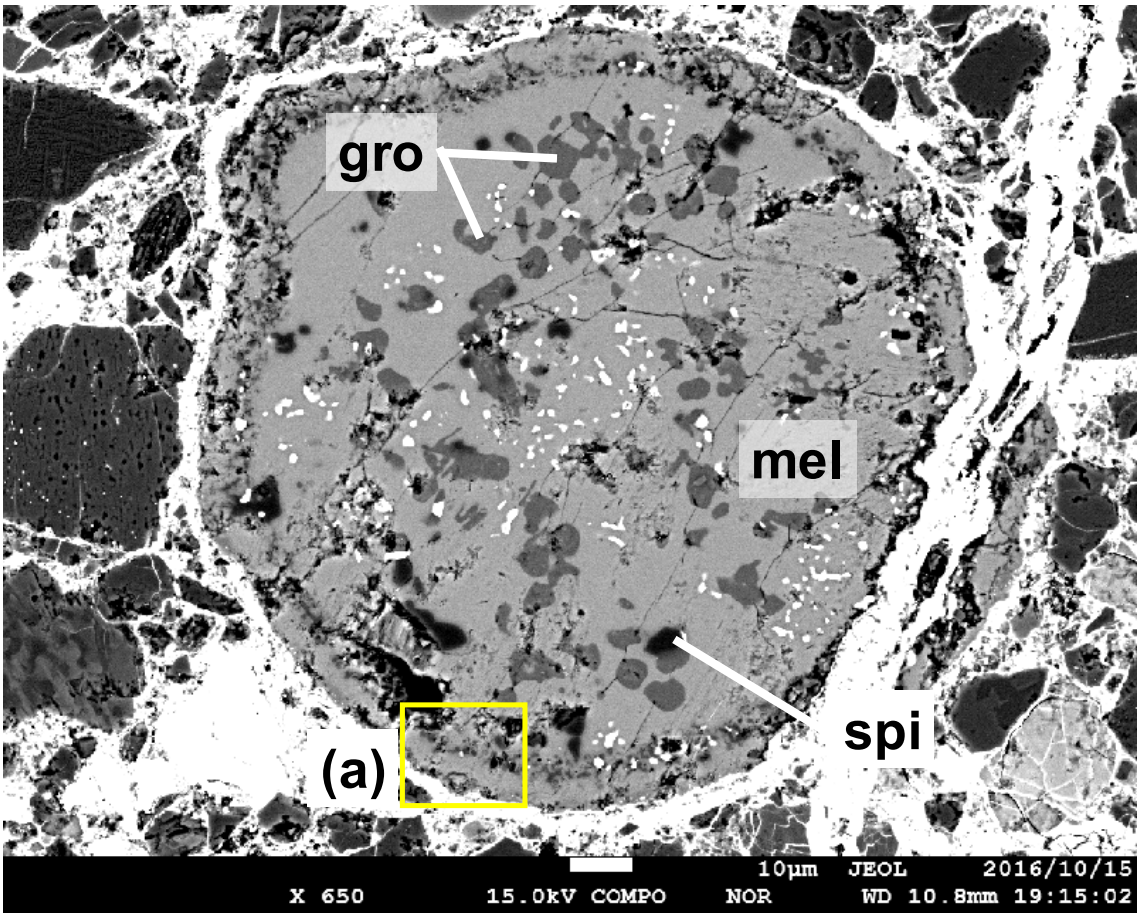

Fig. 3.16. A BEI of the CAI SA202 in the SaU290 (CH3) chondrite. It consists mostly of gehlenitic melilite ($Åk_{5-9}$), grossite, spinel and perovskite. X-ray elemental maps of regions outlined in (a) are shown in Fig. 3.18.

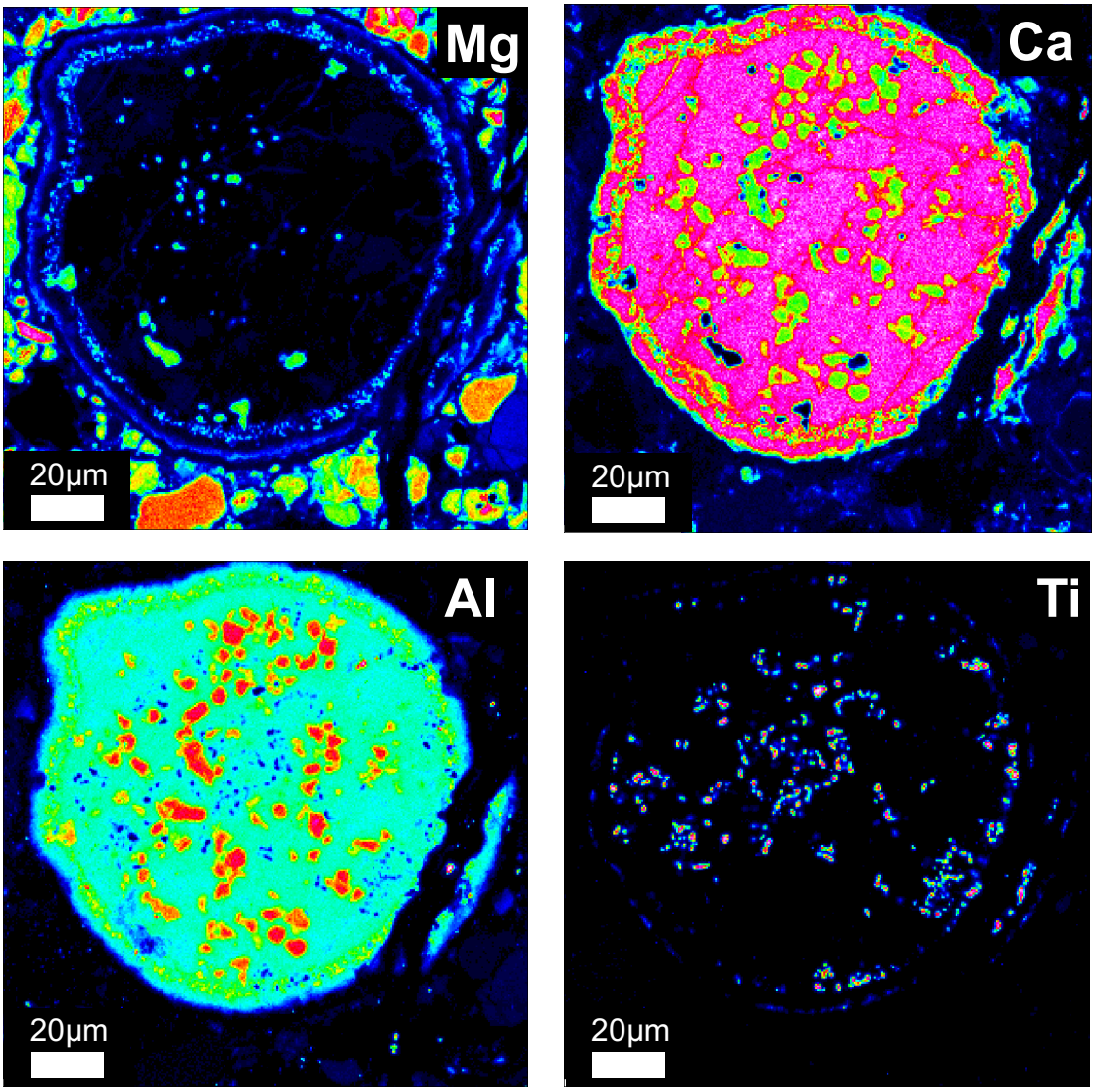

Fig. 3.17. X-ray elemental maps in Mg, Ca, Al, and Ti of the CAI SA202 in the SaU290 (CH3) chondrite.

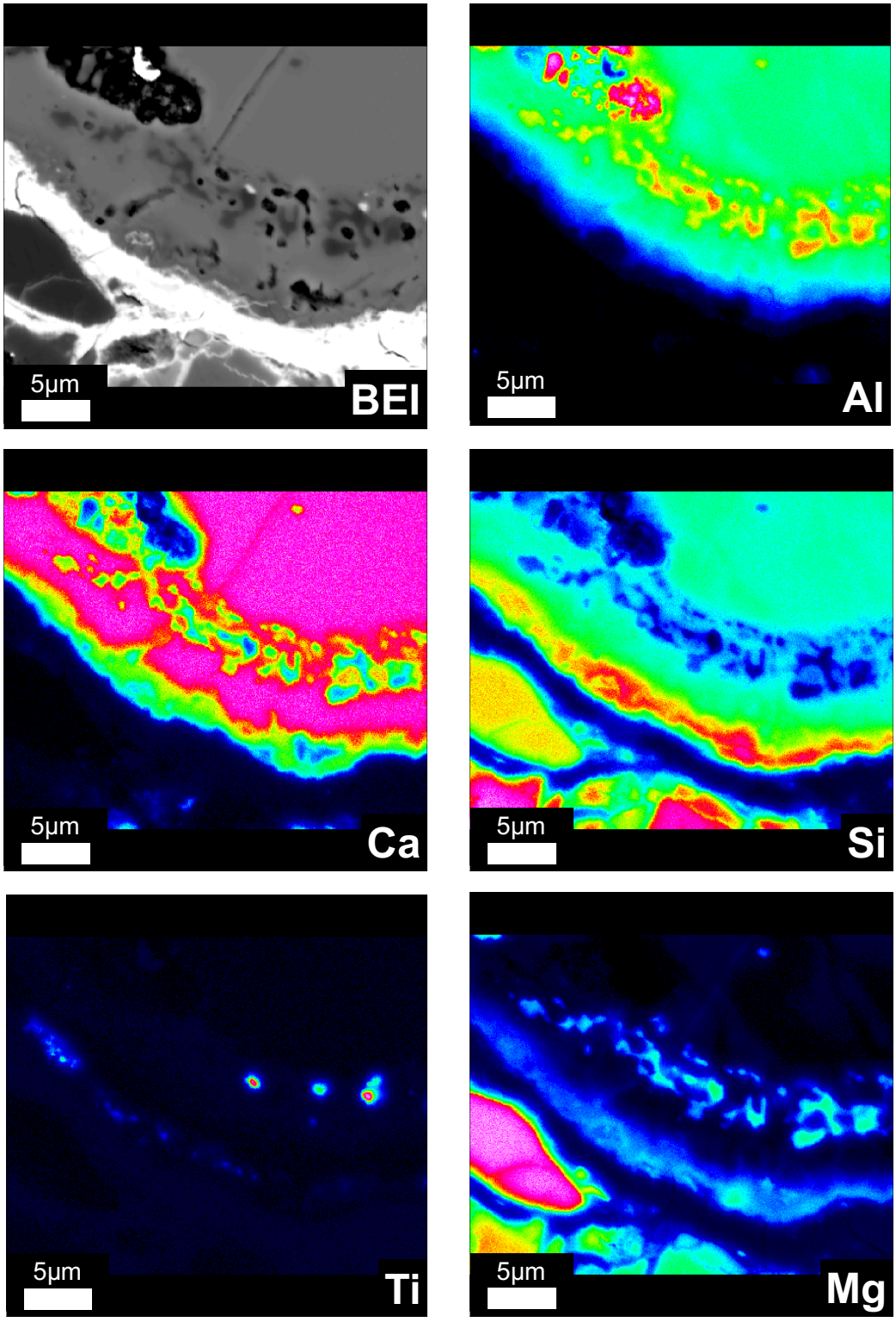

Fig. 3.18. A BEI and X-ray elemental maps in Mg, Ca, Al, Si, and Ti of outlined in Fig. 3.16 a. The CAI SA202 is surrounded by a multi-layered rim (diopside + spinel → melilite → Al-diopside).

CAI SA301 is round and ~80 μm in diameter. It consists mostly of gehlenitic melilite ($Åk_1$), spinel, hibonite, and perovskite. It is surrounded by a double-layered rim of Al-diopside and forsterite. Major element concentrations are shown in Table 3.13. A BEI of SA301 is shown in Fig. 3.19. X-ray elemental mapping are shown in Figs. 3.20 and 3.21.

Tabel 3.13. Major elment concentrations of the SA301 CAI in the SaU290 (CH3) chondrite

Mineral	pv	mel	hib	spi	Al-di_rim	fo_rim
Na_2O	0.00	0.00	0.01	0.02	0.00	0.01
MgO	0.06	0.42	4.77	27.85	15.50	56.34
SiO_2	0.10	22.31	0.76	0.09	49.00	42.64
Al_2O_3	0.90	35.90	75.34	70.26	10.85	0.07
FeO	0.22	0.40	0.27	0.45	0.61	0.86
MnO	0.00	0.01	0.00	0.02	0.00	0.02
K_2O	0.00	0.01	0.00	0.01	0.01	0.01
CaO	41.99	41.14	8.44	0.12	25.23	0.93
TiO_2	57.23	0.43	10.58	0.58	0.27	0.05
V_2O_3	0.09	n.m.**	n.m.**	n.m.**	n.m.**	n.m.**
Cr_2O_3	0.05	0.00	0.06	0.08	0.02	0.10
NiO	0.00	0.01	0.03	0.00	0.02	0.02
Total	100.62	100.62	100.26	99.48	101.50	101.05
No. of analyses	1	5	2	1	1	2
Ak#		3				

** Not measured

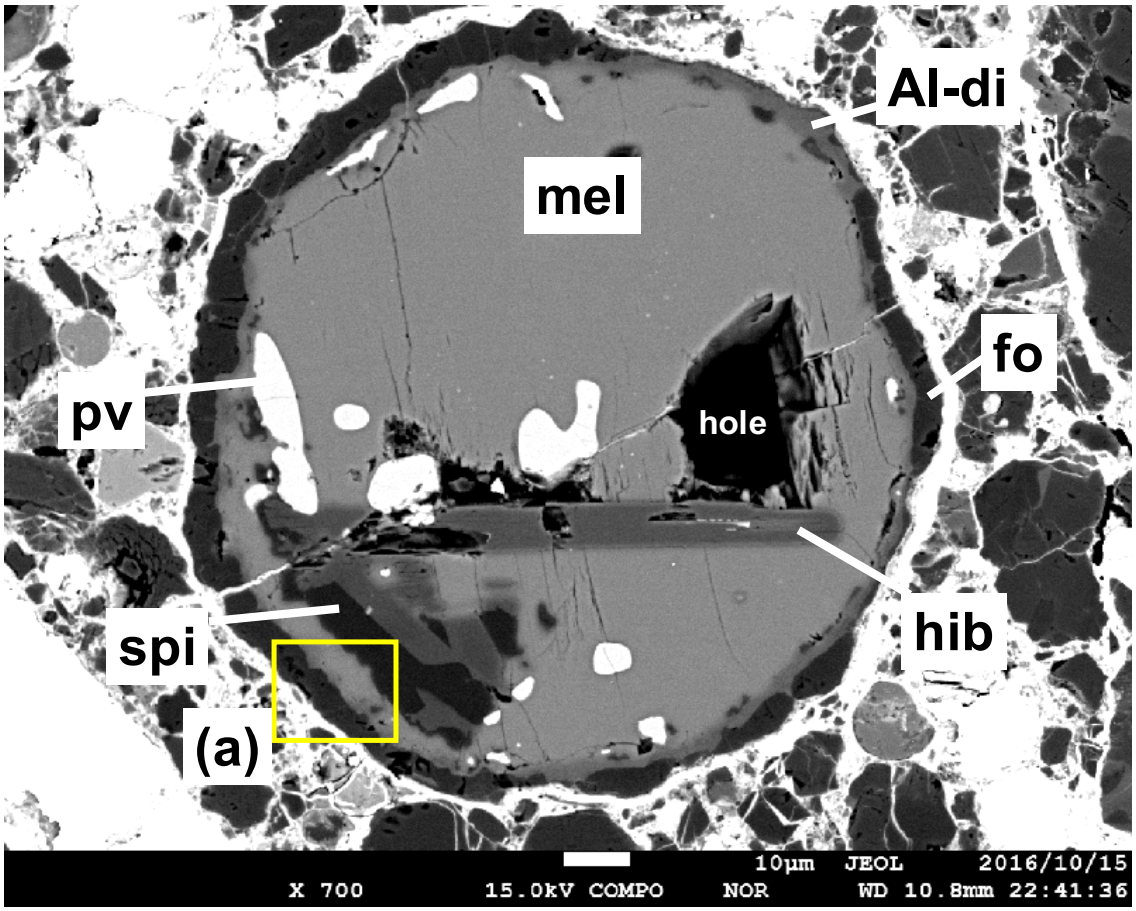

Fig. 3.19. A BEI of the CAI SA301 in the SaU290 (CH3) chondrite. X-ray elemental maps of the region outlined in (a) are shown in Fig. 3.21.

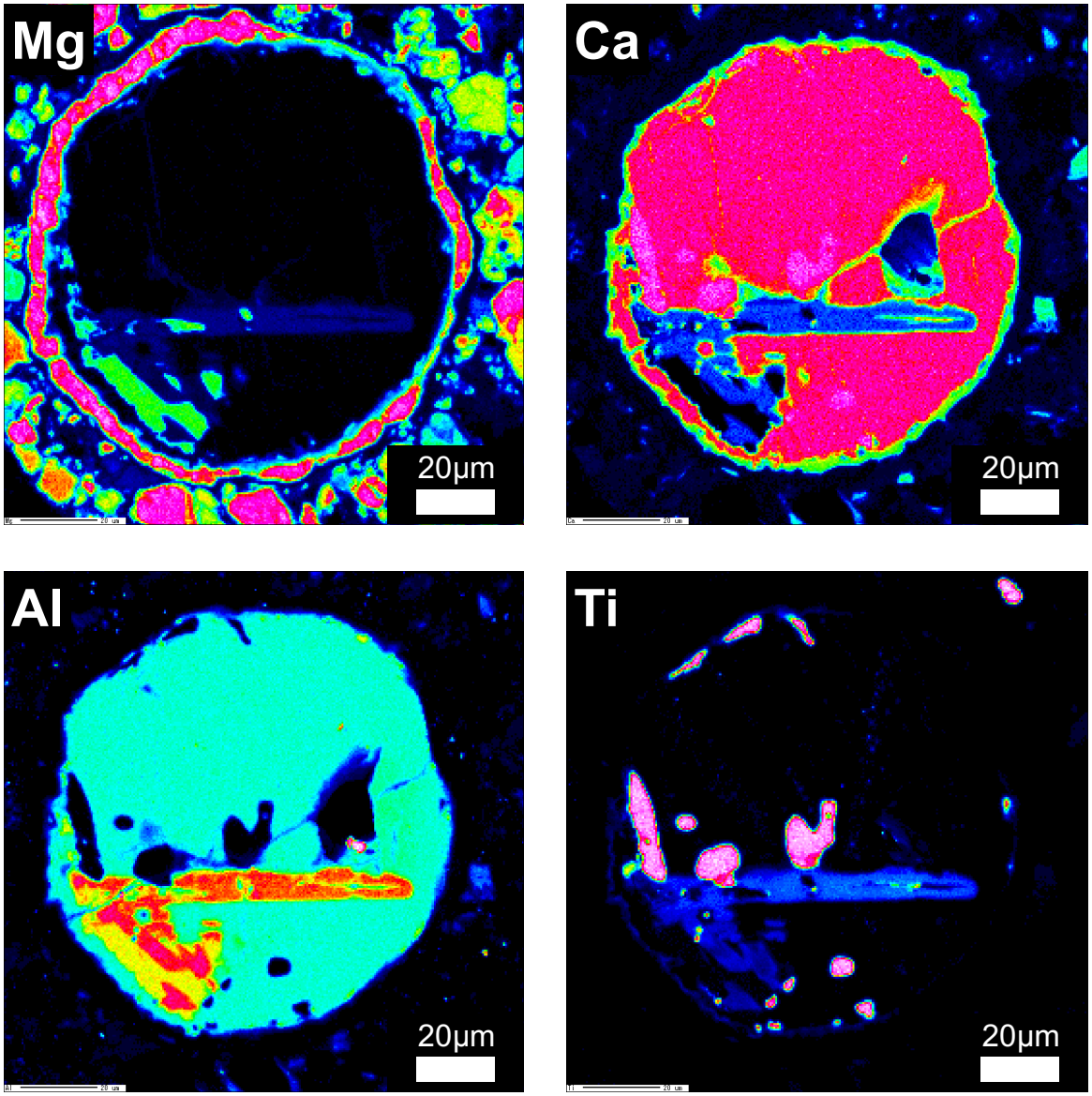

Fig. 3.20. X-ray elemental maps in Mg, Ca, Al, and Ti of the CAI SA301 in the SaU290 (CH3) chondrite. Hibonite shows chemical zoning in Mg, Ti and Al.

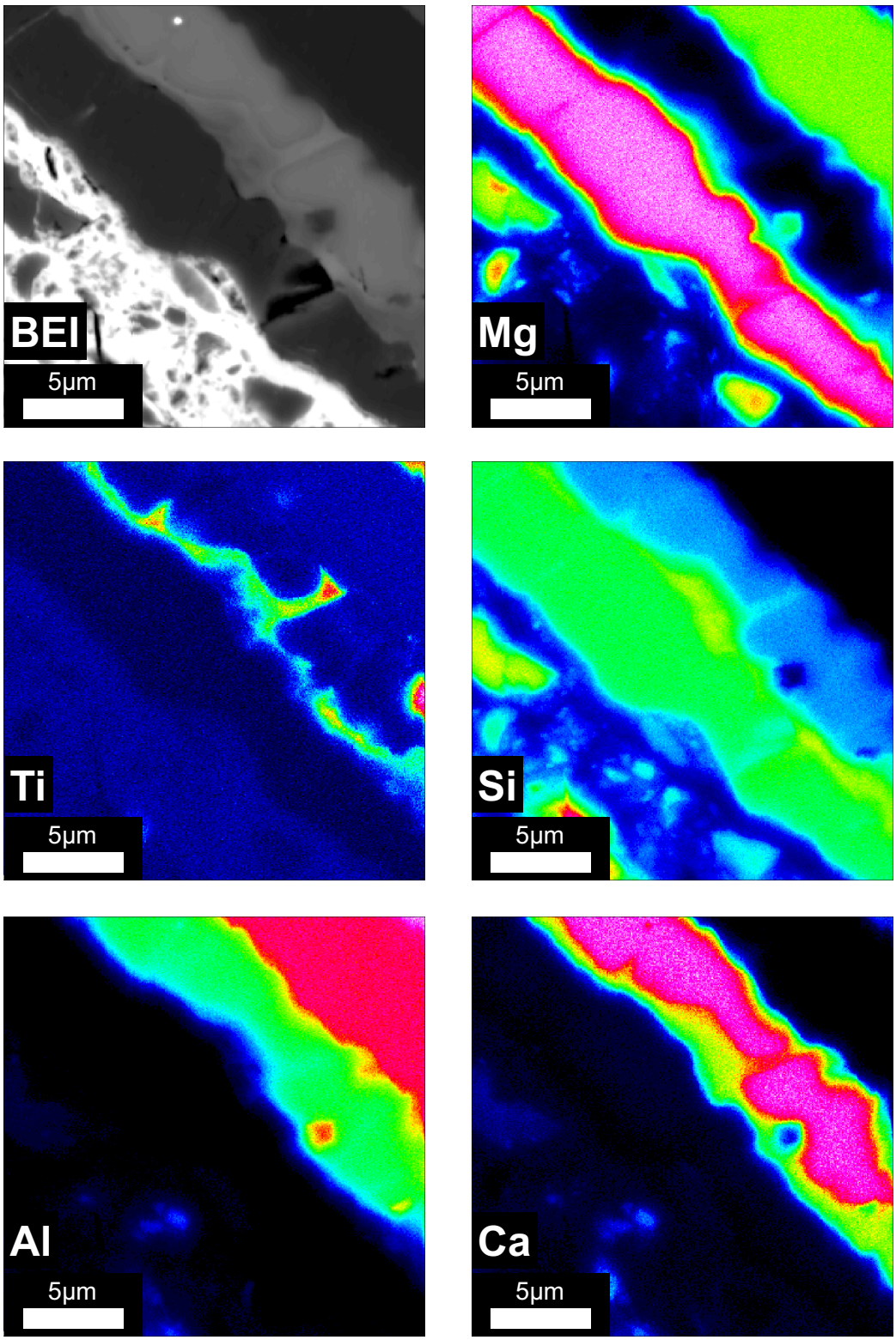

Fig. 3.21. A BEI and X-ray elemental maps in Mg, Ca, Al, Si, and Ti of the outlined region in Fig. 3.19 a. The CAI SA301 is surrounded by a double-layered rim of Al-diopside and forsterite.

CAI fragment SA302 is composed of gehlenitic melilite ($Åk_2$), spinel, and diopside. Titanium in diopside is sector zoned (see Fig. 3.23). Major element concentrations are shown in Table. 3.14. A BEI of SA302 is shown in Fig. 3.22. X-ray elemental mapping are shown in Fig. 3.23.

Tabel 3.14. Major elment concentrations of the SA302 CAI in the SaU290 (CH3) chondrite

Mineral	mel	spi	Al-di	Al-Ti-di
Na_2O	0.00	0.01	0.00	0.01
MgO	0.60	28.30	16.27	13.15
SiO_2	22.61	0.05	51.85	46.59
Al_2O_3	35.46	70.81	7.11	14.20
FeO	0.29	0.46	0.55	0.53
MnO	0.00	0.03	0.04	0.02
K_2O	0.01	0.00	0.01	0.00
CaO	41.00	0.07	25.34	25.37
TiO_2	0.08	0.00	0.03	1.15
V_2O_3	n.m.**	n.m.**	n.m.**	n.m.**
Cr_2O_3	0.01	0.13	0.05	0.15
NiO	0.03	0.04	0.04	0.00
Total	100.09	99.90	101.28	101.16
No. of analyses	5	2	1	1
Ak#	4			

** Not measured

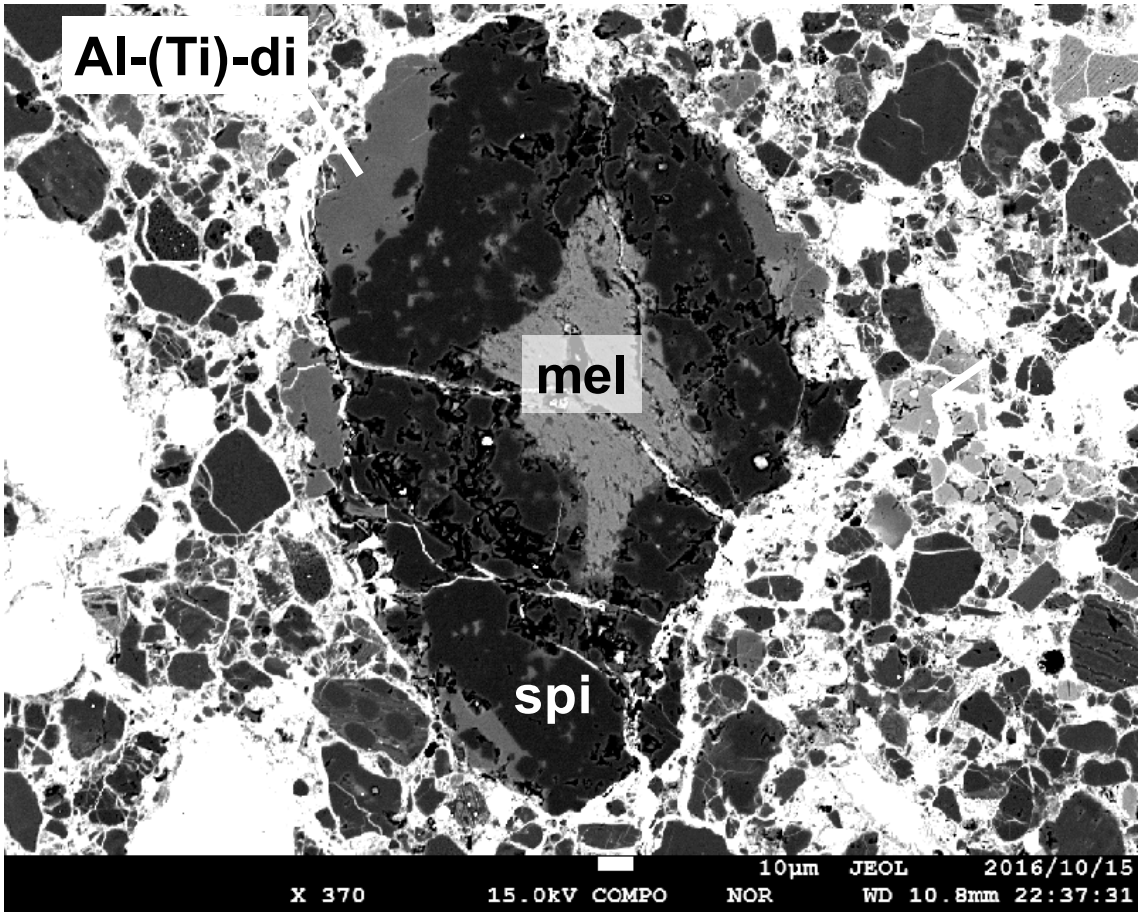

Fig. 3.22. A BEI of the CAI SA302 in the SaU290 (CH3) chondrite.

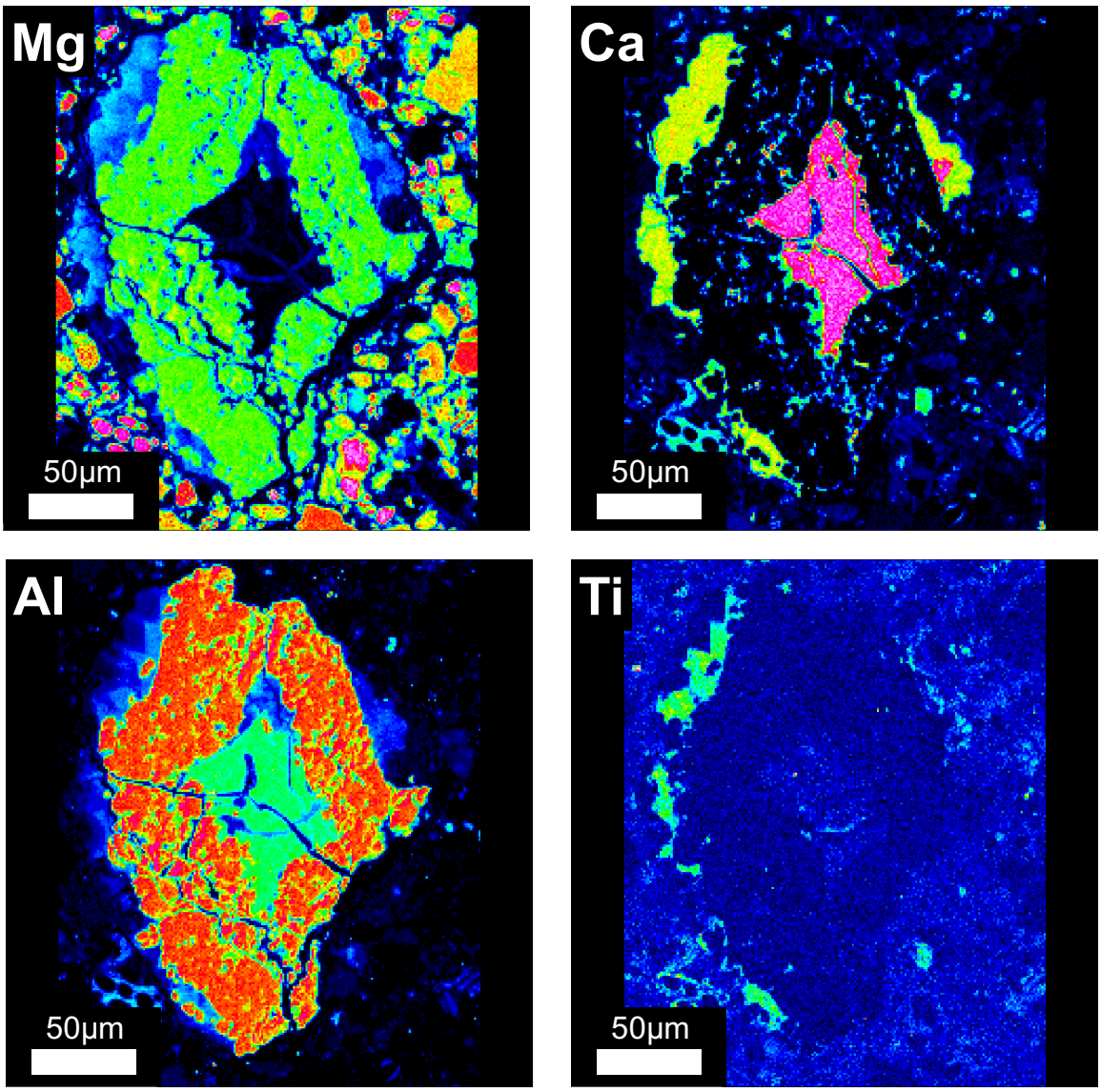

Fig. 3.23. X-ray elemental maps in Mg, Ca, Al, and Ti of the CAI SA302 in the SaU290 (CH3) chondrite. Diopside shows sector zoning in Mg, Al, and Ti.

CAI fragment SD101 consists mostly of gehlenitic melilite ($Åk_3$), Al-Ti-rich diopside, and perovskite. It is surrounded by a double-layered rim of Al-Ti-diopside and olivine. Major element concentrations are shown in Table. 3.15. A BEI of SA302 is shown in Fig. 3.24.

Tabel 3.15. Major elment concentrations of the SD101 CAI in the SaU290 (CH3) chondrite

Mineral	mel	pv	Al-Ti-di	Al-Ti-di_rim	fo_rim
Na_2O	0.00	0.02	0.00	0.00	0.00
MgO	0.93	0.05	6.81	13.09	52.29
SiO_2	23.26	0.44	33.28	42.67	41.52
Al_2O_3	34.53	0.48	20.71	16.60	0.75
FeO	0.52	0.63	1.61	0.82	1.30
MnO	0.01	0.00	0.00	0.00	0.00
K_2O	0.01	0.00	0.00	0.02	0.00
CaO	41.21	41.14	26.36	24.83	1.88
TiO_2	0.13	57.54	12.01	2.33	0.09
V_2O_3	n.m.**	0.73	0.38	0.32	0.09
Cr_2O_3	0.02	0.04	0.10	0.11	0.12
NiO	0.04	0.00	0.06	0.08	0.00
Total	100.66	101.06	101.31	100.86	98.03
No. of analyses	4	1	1	1	1
Ak#	6				

** Not measured

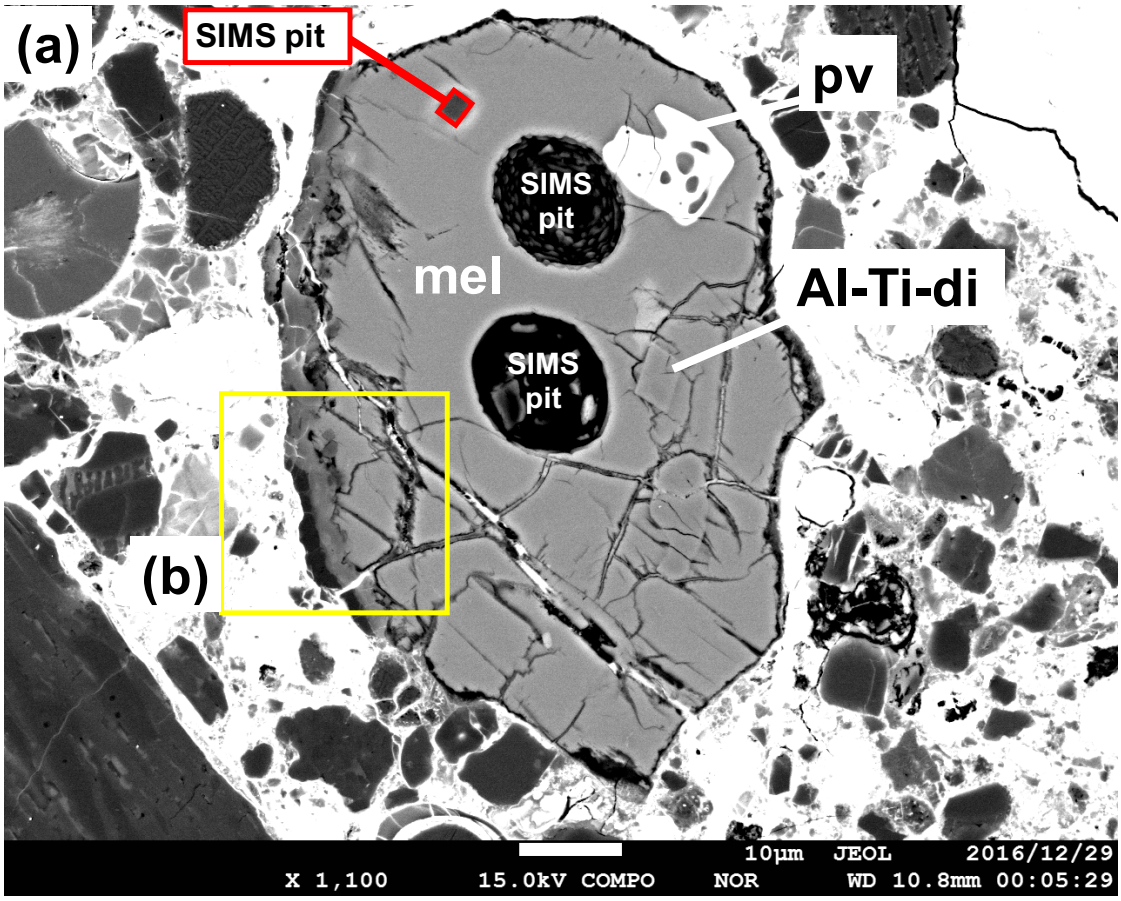

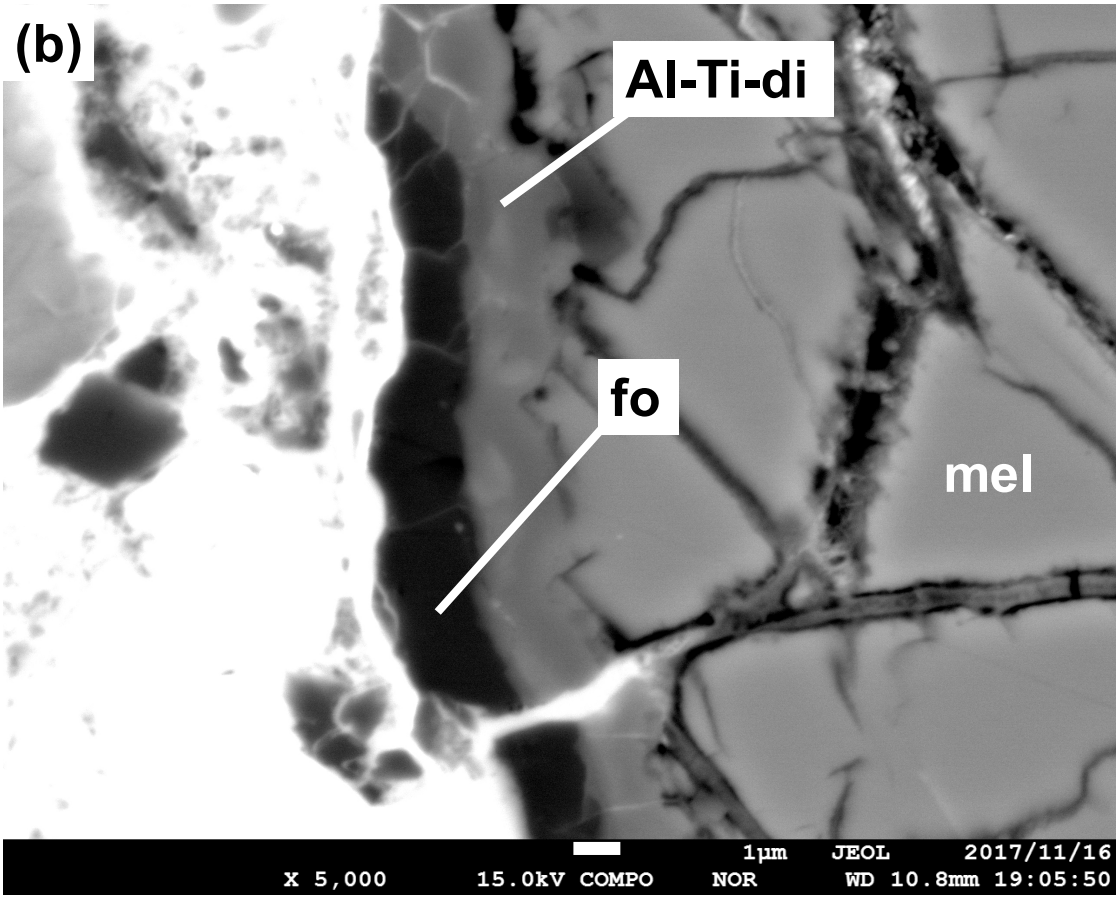

Fig. 3.24. (a) A BEI of the CAI SD101 in the SaU290 (CH3) chondrite. A region outlined in (a) is shown in detail in (b). The CAI is surrounded by a double-layered rim of Al-Ti-diopside and olivine.

CAI SD103 is round and ~30 μm in diameter. It consists mostly of grossite. The CAI is surrounded by a double-layered rim of spinel and Al-diopside. Major element concentrations are shown in Table. 3.16. A BEI of SD103 is shown in Fig. 3.25.

Tabel 3.16. Major elment concentrations of the SD103 CAI in the SaU290 (CH3) chondrite

Mineral	gro	spi_rim	di_rim
Na_2O	0.01	0.01	0.00
MgO	0.06	27.75	16.33
SiO_2	0.07	0.89	48.90
Al_2O_3	77.96	70.52	6.24
FeO	0.97	1.07	4.60
MnO	0.02	0.05	0.05
K_2O	0.01	0.00	0.04
CaO	21.36	0.83	22.21
TiO_2	0.20	0.11	0.04
V_2O_3	n.m.**	n.m.**	n.m.**
Cr_2O_3	0.01	0.02	0.06
NiO	0.05	0.08	0.44
Total	100.70	101.32	98.91
No. of analyses	9	1	1

** Not measured

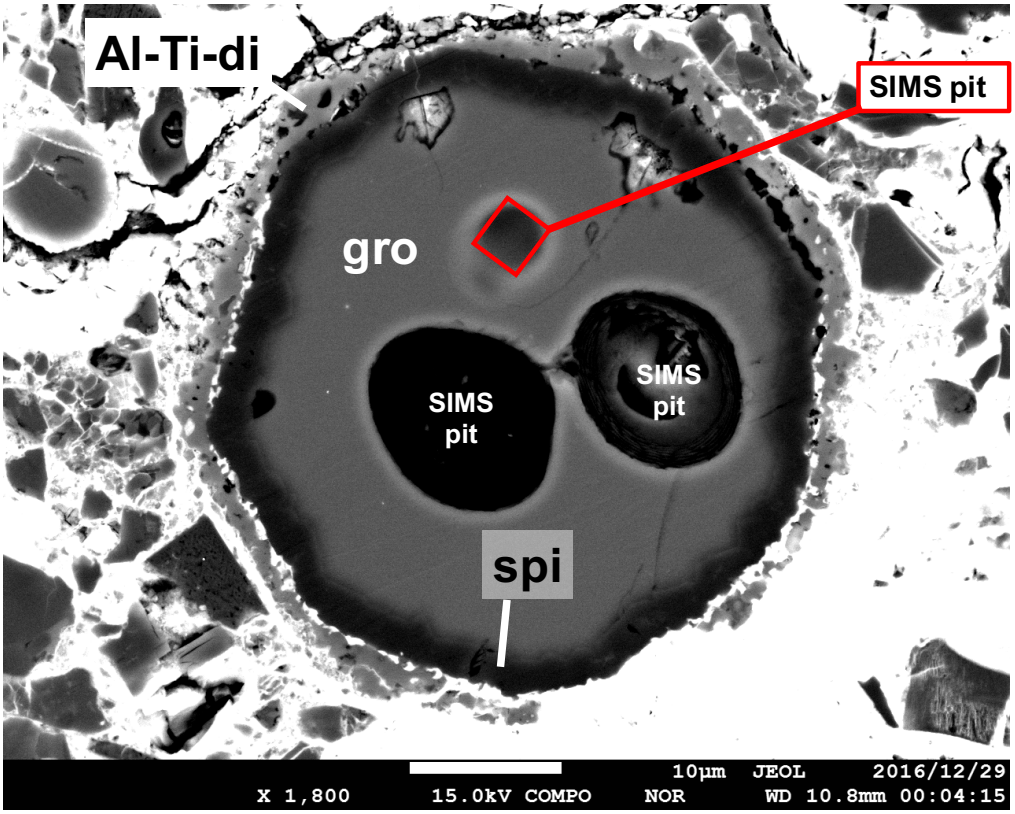

Fig. 3.25. A BEI of the CAI SD103 in the SaU290 (CH3) chondrite. The CAI is surrounded by a double-layered rim of spinel and Al-Ti-rich diopside.

CAI SF1803 is round and ~70 μm in diameter. It consists of gehlenitic melilite ($Åk_2$), grossite, hibonite, and perovskite. It is surrounded by a double-layered rim of melilite (~5 μm) and Al-diopside (~1 μm). The core and rim melilite are both gehlenitic ($Åk_2$). Major element concentrations are shown in Table. 3.17. BEIs of SF1803 are shown in Fig. 3.25. X-ray elemental maps are shown in Figs. 3.26 and 3.27.

Tabel 3.17. Major elment concentrations of the SF1803 CAI in the SaU290 (CH3) chondrite

Mineral	mel_core	mel_rim	gro	hib	pv
Na_2O	0.00	0.00	0.00	0.00	0.00
MgO	0.70	0.55	0.19	1.03	0.04
SiO_2	22.82	22.29	0.59	0.61	0.91
Al_2O_3	35.07	36.16	76.29	86.55	1.91
FeO	0.46	0.96	0.94	0.41	0.52
MnO	0.01	0.00	0.03	0.00	0.00
K_2O	0.00	0.01	0.00	0.01	0.02
CaO	41.22	40.50	21.68	9.79	41.78
TiO_2	0.10	0.09	0.11	2.21	55.65
V_2O_3	n.m.**	n.m.**	n.m.**	n.m.**	0.98
Cr_2O_3	0.03	0.00	0.00	0.03	0.06
NiO	0.05	0.08	0.06	0.04	0.00
Total	100.46	100.65	99.88	100.67	101.86
No. of analyses	2	2	2	1	1
Ak#	5	4			

** Not measured

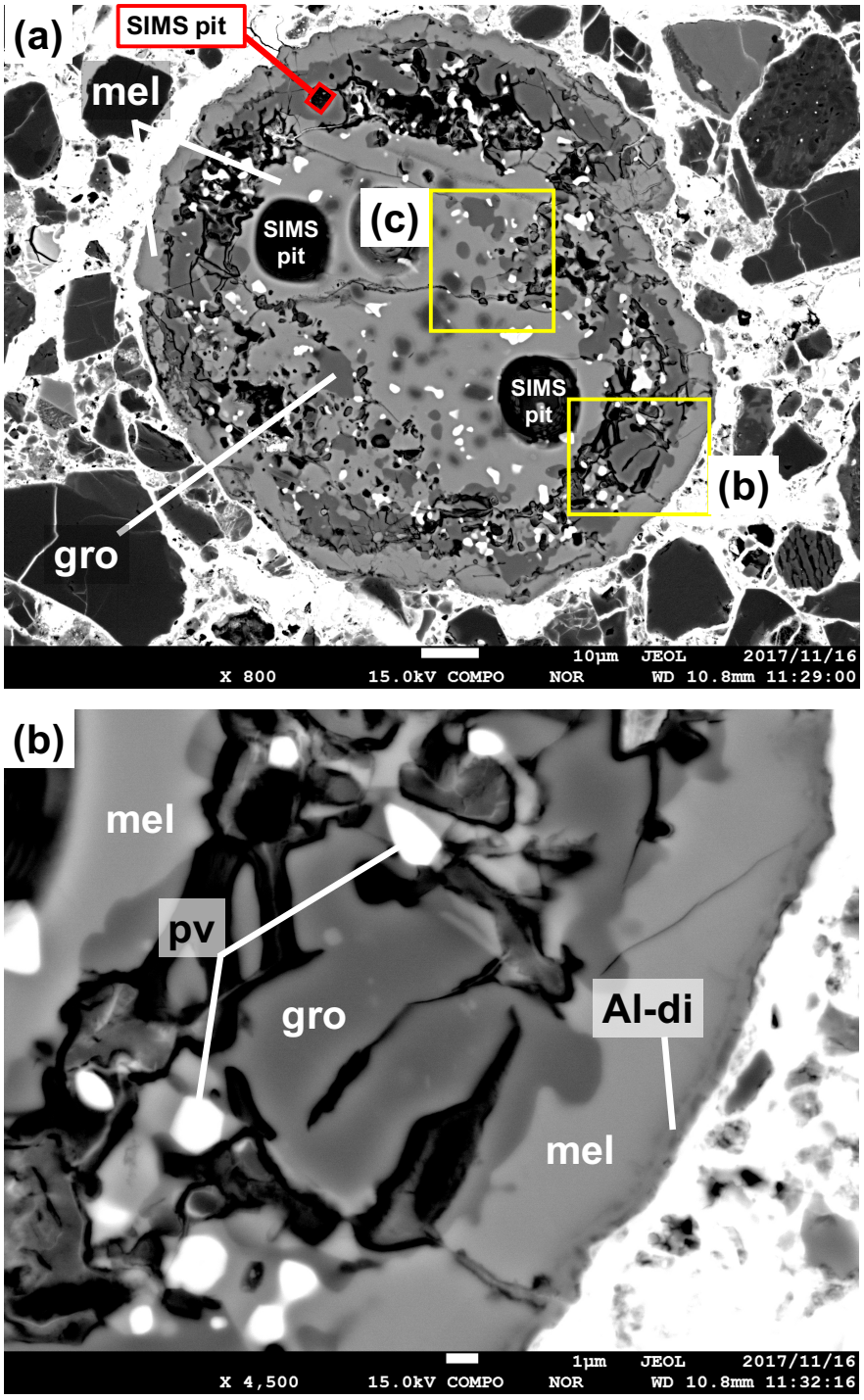

Fig. 3.26. (a) A BEI of the CAI SF1803 in the SaU290 (CH3) chondrite. A region outlined in (a) is shown in detail in (b). The CAI is surrounded by a double-layered rim of melilite and Al-Ti-diopside. X-ray elemental maps of the CAI are shown in Fig. 3.27. X-ray elemental maps of a region of (c) are shown in Fig. 3.28.

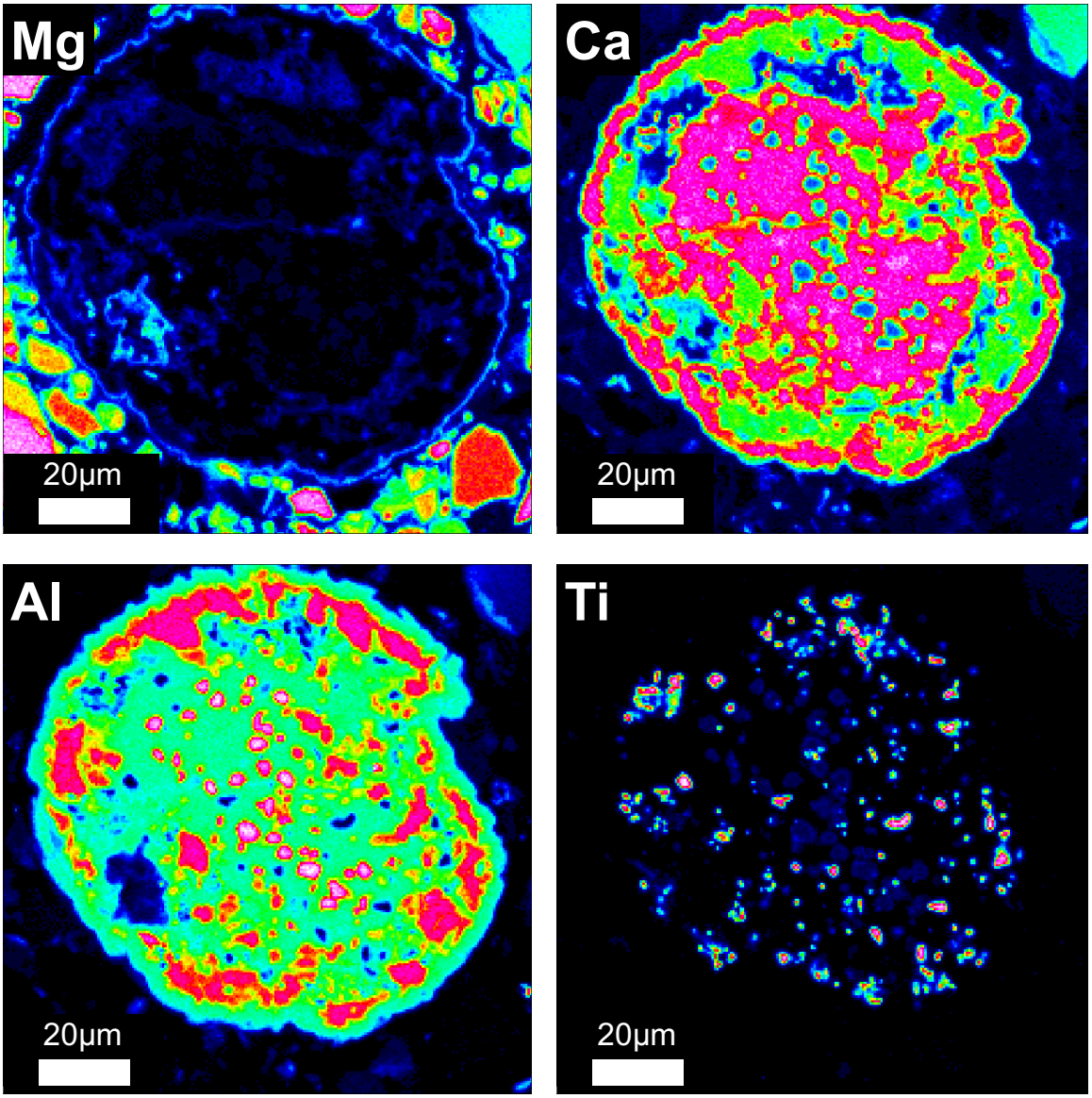

Fig. 3.27. X-ray elemental maps in Mg, Ca, Al, and Ti of the CAI SF1803 in the SaU290 (CH3) chondrite.

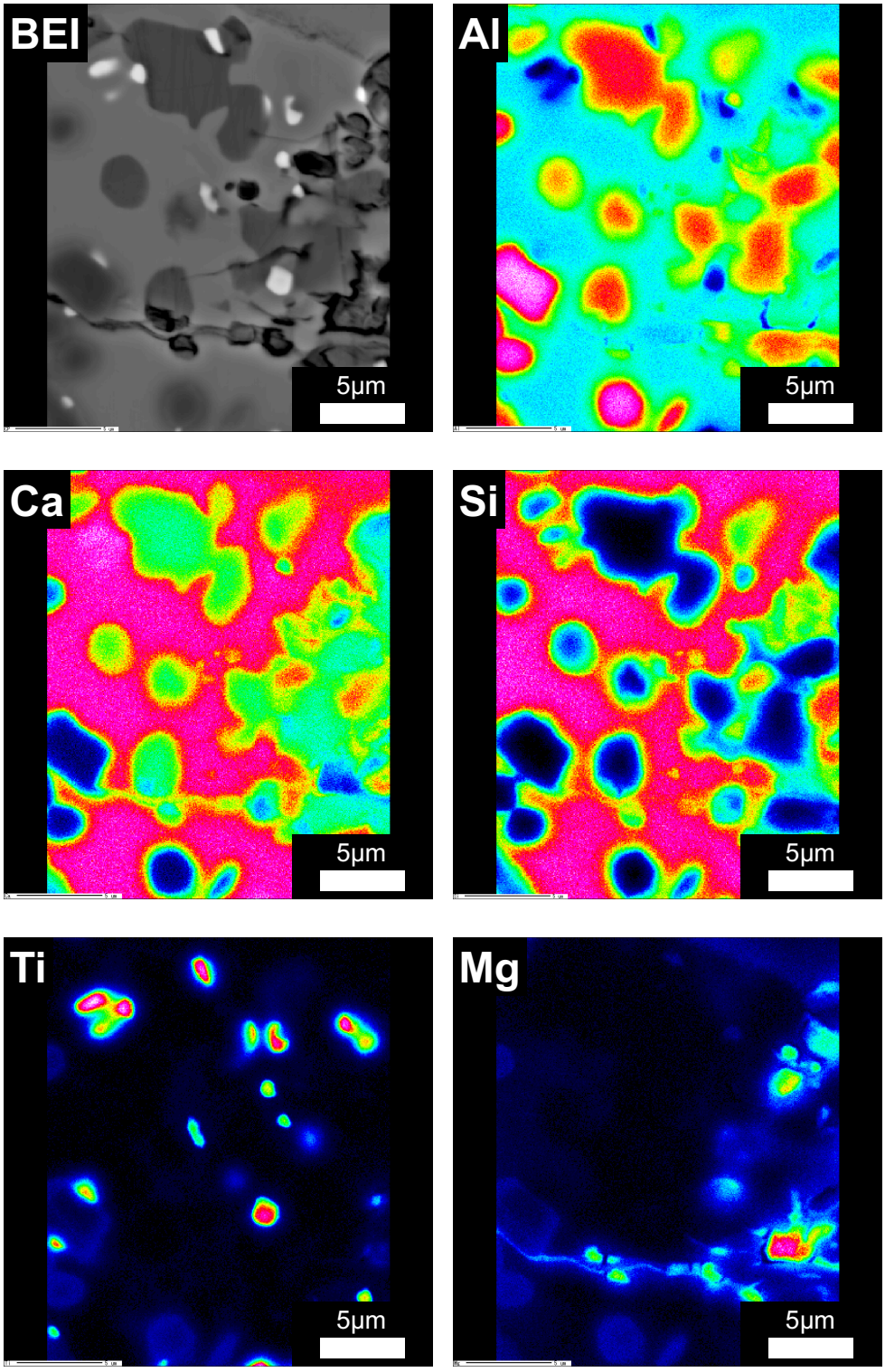

Fig. 3.28. A BEI and X-ray elemental maps in Mg, Ca, Al, Si, and Ti of a region of (c) outlined in Fig. 3.26. Hibonite and grossite in the CAI SA301 show chemical zoning in these elements.

3.2.3. Measurement conditions of Li-Be-B isotope analyses

The Be-B isotope measurements were performed using a NanoSIMS 50 installed at the Atmosphere and Ocean Research Institute (AORI), the University of Tokyo. The measurement conditions are similar to those described in section 2.2.2. An $^{16}O^-$ primary ion beam, ~5 nA intensity and ~10 μm in diameter, was rastered over 10 x 10 μm^2 areas (32 × 32 pixel with a dwell time of 200 μs/pixel). Prior to the measurements, a primary ion beam of ~5 nA was rastered over 15 × 15 μm^2 on the samples to remove surface contamination and to obtain secondary ion images of the samples, which helped to choose measurement spots. Typical intensities of $^9Be^+$, $^{10}B^+$, and $^{30}Si^+$ of the samples were ~500 cps, ~0.2 cps, and ~1.0×10^5 cps, respectively. An electronic beam blanking mode was applied so that only signals from the central 24 × 24 pixel area were collected. A dead time (~44 ns) of the counting system was also corrected. The background of EMs were checked for each analytical spot after each measurement and corrected. The background ranged from 0.007 to 0.05 cps. The Be/B, Be/Si and B/Si RSF was evaluated using NIST 610 standard that has the same Be/B RSF determined from the measurements of synthetic melilite glasses (see chapter 2). The instrumental mass fractionation effects were also corrected using NIST 610 standard ($^{10}B/^{11}B = 0.2469$: Kasemann et al. 2001).

After the Be-B isotope measurements, Li isotope measurements were performed using the same secondary ion optics of the Be-B isotope measurements. Secondary ions of $^6Li^+$, $^7Li^+$, and $^{30}Si^+$ were detected simultaneously with EMs. Intensities of $^6Li^+$ and $^{30}Si^+$ of the samples were ~5 cps and 1.0×10^5 cps, respectively. The background ranged from 0.005 to 0.02 cps. The instrumental mass fractionation effects were corrected using a NIST 612 glass ($^7Li/^6Li = 12.553$; Kasemann et al., 2005). The Li concentrations of CAIs were estimated by comparison with the NIST 612 glass ([Li] = 40.2 ppm; Jochum et al., 2011).

3.2.4. Measurement conditions of Al-Mg isotope analyses

The Al-Mg isotope measurements were performed with the NanoSIMS 50 at AORI, the University of Tokyo. An $^{16}O^-$ primary ion beam, ~ 50 to 200 pA intensity and ~2 μm in diameter, was rastered over 5 x 5 μm^2 areas (32 × 32 pixel with a dwell time of 200 μs/pixel). Prior to the measurements, a primary ion beam of ~200 pA was rastered over 5 × 5 μm^2 on the samples to remove carbon coating and to obtain secondary ion images of the samples, which helped to choose measurement spots. Then secondary ions of $^{27}Al^{++}$, $^{24}Mg^+$, $^{25}Mg^+$, and $^{26}Mg^+$ were detected in a combined peak-jumping/multi-detection mode. The magnet was cycled through three field setting and the waiting times were 6, 4, and 4 seconds, respectively. In the first setting, $^{27}Al^{++}$ and $^{24}Mg^+$ were simultaneously detected with two EMs with the measurements time of 1 second. Subsequently, $^{25}Mg^+$ was detected with the same EM as for $^{24}Mg^+$ with the measurement time of 5 seconds. Finally, $^{26}Mg^+$ was detected with the same EM as for $^{24}Mg^+$ and $^{25}Mg^+$ with the measurement time of 5 seconds. Measurements were performed with a mass resolving power (MPR) of 3500 at 10% peak height, which is sufficient to separate $^{24}Mg^1H^+$ on $^{25}Mg^+$ and $^{25}Mg^1H^+$ on $^{26}Mg^+$. Intensities of $^{27}Al^{++}$ and $^{25}Mg^+$ of the samples ranged from ~150 to 900 cps and ~50 to 12000 cps, respectively. An electronic beam blanking mode was applied so that only signals from the central 24 × 24 pixel area were collected. This blanking helped to avoid contributions from scattered ions from the surroundings. A dead time (~44 ns) of the counting system was also corrected. The background of EMs, much lower than ~0.02 cps, was not corrected because it was negligible compared with the count rates of $^{27}Al^{++}$ and $^{25}Mg^+$ for the samples. The Al/Mg RSF was evaluated using Madagascar hibonite and synthetic melilite glasses standards. The instrumental mass fractionation effects were corrected using Madagascar hibonite, assuming that it has a terrestrial magnesium-isotope composition [$^{25}Mg/^{24}Mg = 0.12663$, $^{26}Mg/^{24}Mg = 0.13932$ (Catanzaro et al., 1966)].

3.3. Isotopic results

I studied the Be-B systems for two CAIs in Y81020, two CAIs in Y82094, seven CAIs in SaU290, and one CAI in Isheyevo. Among these CAIs, I also studied the Al-Mg systems for one CAI in Y81020, six CAIs in SaU290, and one CAI in Isheyevo. In addition, I also measured Li isotopic compositions of two CAIs in Y81020 and five CAIs in SaU290. CAIs measured by LA-ICPMS and SIMS in this study are summarized in Table 3.18. The results of the isotope analyses are presented in Tables 3.19, 3.20, and 3.21.

Table. 3.18 List of analyses performed on the samples in the present study.

meteorite	Sample name	minerals*[2]	Li	Be-B	Al-Mg	REE
Y81020 (CO3.05)	Y20-1X1	mel, spi, pv, Al-Ti-di	**	**	---	**
Y81020 (CO3.05)	Y20-9-1	mel, spi, pv	**	**	**	**
Y82094 (ungrouped C3.2)	Y94-42C5	mel, hib, spi, ilm, Al-rich silicate	---	**	*[1]	**
Y82094 (ungrouped C3.2)	Y94-42C7	mel, pv, pl, pyx, Al-rich silicate	---	**	**	**
Isheyevo (CH/CBb)	ISC103	mel, spi, Al-Ti-di, fo	---	**	**	---
SaU290 (CH3)	SA201	mel, hib, spi, pv, Al-Ti-di	---	**	---	---
SaU290 (CH3)	SB202	mel, gro, spi, pv, Al-Ti-di	---	**	**	---
SaU290 (CH3)	SA301	mel, hib, spi, Al-di, fo	**	**	**	---
SaU290 (CH3)	SA302	mel, hib, spi, Al-(Ti)-di	**	**	**	---
SaU290 (CH3)	SD101	mel, pv, Al-Ti-di	**	**	**	---
SaU290 (CH3)	SD103	gro, spi, Al-Ti-di	**	**	**	---
SaU290 (CH3)	SF1803	mel, gro, hib, pv, Al-di	**	**	**	---

** indicates measured data in the present study and --- indicates note measred.

*[1] Unpublised data measured by N. Sugiura

*[2] Abbreviations: mel = melilite, spi = spinel, pv = perovskite, hib = hibonite, gro = grossite, ilm = ilmenite Al-(Ti)-di = Al-(Ti)-rich diopside, pl = plagioclase, pyx = pyroxene, fo = forsterite

Table. 3.19 Be-B isotope data of the CAIs in the Y81020, Y82094, Isheyevo, and SaU290 carbonaceous chondrites

Meteorite	Sample name	Analysis spots	mineral	Be (ppb)	B (ppb)	$^{9}Be/^{11}B$	error (2σ)	$^{10}B/^{11}B$	error (2σ)
Y81020 (CO3.05)	Y20-1X1	Y20-1X1_A	mel	529	28	30.3	2.8	0.338	0.052
		Y20-1X1_B	mel	648	15	77.6	8.9	0.471	0.094
		Y20-1X1_1	mel	736	7	266.8	40.0	1.059	0.209
		Y20-1X1_2	mel	578	5	250.8	37.2	0.999	0.198
		Y20-1X1_3	mel	563	7	161.2	19.3	0.695	0.118
		Y20-1X1_4	di	22	2912	0.011	0.001	0.251	0.004
		Y20-1X1_5	mel	763	9	161.6	18.7	0.666	0.110
		Y20-1X1_6	mel	---**	---**	80.2	12.1	0.666	0.150
		Y20-1X1_7	mel	560	8	145.6	16.6	0.751	0.118
		mel_Average		*625*	*4*				
Y81020 (CO3.05)	Y20-9-1	Y20-9-1_1	mel	909	12	156.8	29.9	0.821	0.217
		Y20-9-1_2	mel	800	68	18.7	1.9	0.338	0.048
		Y20-9-1_3	mel	843	7	335.3	74.1	1.309	0.365
		Y20-9-1_5	mel	733	6	332.5	71.7	1.161	0.321
		Y20-9-1_6	mel	892	12	131.2	15.4	0.458	0.074
		Y20-9-1_8	mel	662	18	59.2	6.7	0.358	0.073
		Y20-9-1_9	mel	787	15	94.0	10.5	0.494	0.086
		Y20-9-1_10	mel	714	7	215.1	26.7	0.723	0.127
		Average		*793*	*18*				
Y82094 (ungrouped C3.2)	Y94-42C5	Y94-42C5_1	mel	1081	125	13.1	0.7	0.267	0.028
		Y94-42C5_2	mel	971	17	90.2	7.0	0.331	0.049
		Y94-42C5_3	mel	537	77	10.8	0.5	0.305	0.032
		Average		*863*	*73*				
Y82094 (ungrouped C3.2)	Y94-42C7	Y94-42C7_1	mel	983	23	77.7	12.6	0.544	0.127
		Y94-42C7_2	mel	907	43	33.1	4.3	0.327	0.066
		Average		*945*	*33*				
Isheyevo (CH/CBb)	ISC103	ISC103_1	mel	349	17	30.7	1.4	0.341	0.052
SaU290 (CH3)	SA201	SA201_1	mel	1346	36	44.1	1.0	0.285	0.052
		SA201_1	mel	1009	62	18.9	0.4	0.273	0.054
		*Average & Weighted mean**		*1178*	*49*	*22.8*	*0.4*	*0.279*	*0.037*
SaU290 (CH3)	SB202	SB202_1	mel	531	52	16.0	0.7	0.312	0.021
		SB202_2	mel	332	23	23.0	1.0	0.356	0.066
		*Average & Weighted mean**		*432*	*19*	*18.3*	*0.6*	*0.321*	*0.020*
SaU290 (CH3)	SA301	SA301_1	mel	397	8	141.8	3.2	0.939	0.169
		SA301_2	mel	449	13	101.7	1.5	0.637	0.173
		SA301_3	mel	307	5	61.0	0.9	0.457	0.068
		*Average & Weighted mean**		*384*	*8*	*75.8*	*0.8*	*0.537*	*0.059*
SaU290 (CH3)	SA302	SA302_1	mel	467	69	10.4	0.3	0.272	0.037
SaU290 (CH3)	SD101	SD101_1	mel	761	15	86.2	4.1	0.392	0.079
		SD101_2	mel	720	14	82.3	4.0	0.310	0.051
		*Average & Weighted mean**		*740*	*15*	*84.2*	*2.9*	*0.334*	*0.043*
SaU290 (CH3)	SD103	SD103_1	gro	1875	11	277.4	13.3	0.294	0.102
SaU290 (CH3)	SF1803	SF1803_1	mel	561	17	47.7	1.2	0.361	0.074

* concentrations represent average values and $^{9}Be/^{11}B$ ratios and $^{10}B/^{11}B$ ratios represent weighted mean values.

** ^{30}Si is not measured.

Table. 3.20 Li isotope data of the CAIs in the Y81020 and SaU290 carbonaceous chondrites

Meteorite	Sample name	Analysis spots	mineral	Li (ppb)	$^{7}Li/^{6}Li$	error (2σ)
Y81020 (CO3.05)	Y20-1X1	Y20-1X1_1	mel	630	12.18	0.17
Y81020 (CO3.05)	Y20-9-1	Y20-9-1_1	mel	71	12.06	0.36
		Y20-9-1_2	mel	59	12.01	0.44
		*Average & Weighted mean**		*65*	*12.04*	*0.28*
SaU290 (CH3)	SA301	SA301_1	mel	38	11.78	0.61
		SA301_2	mel	42	11.93	0.37
		*Average & Weighted mean**		*40*	*11.89*	*0.31*
SaU290 (CH3)	SA302	SA302_1	mel	26	11.68	0.92
SaU290 (CH3)	SD101	SD101_1	mel	63	12.03	1.02
SaU290 (CH3)	SD103	SD103_1	gro	376	12.46	0.51
SaU290 (CH3)	SF1803	SF1803_1	mel	40	12.70	0.61

* concentrations represent average values and $^{9}Be/^{11}B$ ratios and $^{10}B/^{11}B$ ratios represent weighted mean values.

Table. 3.21 Al-Mg isotope data of the CAIs in the Y81020, Isheyevo, and SaU290 carbonaceous chondrites

Meteorite	Sample name	Analysis spots	mineral	$\delta^{25}Mg$ (‰)	error (2σ)	$^{27}Al/^{24}Mg$	error (2σ)	$\delta^{26}Mg^{*}$ (‰)	error (2σ)
Y81020 (CO3.05)	Y20-9-1	Y20-9-1_1	mel	-0.4	3.1	38.3	2.4	17.7	5.5
		Y20-9-1_2	mel	-1.0	1.9	23.9	1.5	9.4	3.0
		Y20-9-1_3	mel	-1.4	2.1	27.6	1.7	11.7	3.3
		Y20-9-1_4	mel	2.8	1.9	60.7	3.7	16.5	3.0
		Y20-9-1_5	mel	0.7	1.8	34.5	2.1	9.6	2.8
		Y20-9-1_6	mel	-2.7	2.2	39.7	2.4	15.3	3.5
		Y20-9-1_7	mel	-0.2	3.4	32.8	1.9	16.5	5.8
		Y20-9-1_8	mel	-0.8	2.8	36.7	2.1	17.9	4.4
		Y20-9-1_9	mel	3.2	2.7	23.1	1.3	9.2	4.0
		Y20-9-1_10	mel	4.1	2.8	21.4	1.2	4.4	4.0
		Y20-9-1_11	mel	6.1	3.3	33.7	1.9	11.4	5.7
		Y20-9-1_12	mel	-2.3	2.6	51.1	2.9	21.7	3.6
		Y20-9-1_13	mel	-1.3	2.8	26.4	1.5	13.1	4.0
Isheyevo (CH/CBb	ISC103	ISC103_1	mel	0.8	4.3	62.4	3.7	0.6	6.4
SaU290 (CH3)	SB202	SB202_1	mel	-1.9	5.9	119.7	7.3	1.7	7.2
		SB202_2	gro	2.8	7.2	2415.6	146.4	-3.3	9.6
SaU290 (CH3)	SA301	SA301_1	hib	-0.1	4.9	13.1	0.8	-1.6	4.7
		SA301_2	mel	-1.0	5.6	61.6	3.7	3.4	6.7
SaU290 (CH3)	SA302	SA302_1	mel	-0.6	5.4	57.1	3.5	-0.4	6.2
SaU290 (CH3)	SD101	SD101_1	mel	-2.4	3.7	32.0	1.9	-4.0	5.1
SaU290 (CH3)	SD103	SD103_1	gro	1.3	19.6	17645.7	1058.7	27.8	28.0
SaU290 (CH3)	SF1803	SF1803_1	mel	1.4	3.6	427.9	25.7	-0.3	4.5

3.3.1. CO and ungrouped C CAIs

For Be-B measurements, taking advantage of the high spatial resolution of the NanoSIMS, I performed replicate analyses for different spots on single CAIs with a total of 9 measurements for Y20-1X1, 8 measurements for Y20-9-1, 3 measurements for Y94-42C5, and 2 measurements for Y94-42C7. Y81020 CAIs (Y20-1X1 and Y20-9-1) show elevated $^{9}Be/^{11}B$ ratios up to ~335 and clear ^{10}B excesses of up to ~4300‰ which correlate well with the $^{9}Be/^{11}B$, indicating the in-situ decay of ^{10}Be (Fig. 3.29a and Fig. 3.29b). The initial $^{10}Be/^{9}Be$ ratios, $(^{10}Be/^{9}Be)_0$, were determined from the slope of isochrons. The $(^{10}Be/^{9}Be)_0$ values were determined to be $(3.0 \pm 0.4) \times 10^{-3}$ and $(2.2 \pm 1.0) \times 10^{-3}$ for Y20-1X1 and Y20-9-1, respectively (errors are 2σ). The initial $^{10}B/^{11}B$ ratios were also determined from the intercept of isochrons, which give 0.251 ± 0.0042 and 0.269 ± 0.093, respectively (errors are 2σ). One of the Y82094 CAIs, Y94-42C7, also shows excesses in ^{10}B with elevated $^{9}Be/^{11}B$ ratios (Fig. 3.29d). Only two Be-B analyses were performed for Y94-42C7. Fitting for the two data points can be made with a simple calculation, which gives the inferred initial $^{10}Be/^{9}Be$ ratio of $(4.9 \pm 3.5) \times 10^{-3}$ with an initial $^{10}B/^{11}B$ ratio of 0.17 ± 0.19 (2σ errors). Here errors in x-axis ($^{9}Be/^{11}B$ ratio) and y-axis ($^{10}B/^{11}B$ ratio) were assumed to be independent. If I assume a chondritic initial boron isotopic ratio ($^{10}B/^{11}B = 0.2481$: Zhai et al., 1996), I obtain a model initial $^{10}Be/^{9}Be$ ratio of $(3.2 \pm 1.3) \times 10^{-3}$ (2σ error), which is consistent with the results of the two-point fitting within uncertainties. Another CAI, Y94-42C5, in the Y82094 may also show a positive correlation between $^{9}Be/^{11}B$ and $^{10}B/^{11}B$ (Fig. 3.29c), but the calculated slope has a large error. As such, we could only infer an upper limit on the $(^{10}Be/^{9}Be)_0$ value of 1.4×10^{-3} for this inclusion. It has an initial $^{10}B/^{11}B$ ratio of 0.28 ± 0.30.

$^{7}Li/^{6}Li$ ratios of Y20-1X1 and Y20-9-1 are 12.18 ± 0.17 and 12.04 ± 0.28, respectively and these values are identical to the chondritic $^{7}Li/^{6}Li$ ratio ($^{7}Li/^{6}Li = 12.06$: Seitz et al. 2007) within uncertainties.

The Al-Mg isotope systems of the Y20-9-1 exhibit a rough linear correlation in the $\delta^{26}Mg^*$ vs. $^{27}Al/^{24}Mg$ diagram (Fig. 3.30). The $^{27}Al/^{24}Mg$ ratios of melilite in Y20-9-1 are variable from 21 to 60. The initial $^{26}Al/^{27}Al$ ratio, $(^{26}Al/^{27}Al)_0$, was determined from the slope of the isochron assuming the initial Mg isotopic composition ($\delta^{26}Mg$ = -0.04; Jacobsen et al., 2008). The $(^{26}Al/^{27}Al)_0$ value was determined to be $(5.0 \pm 0.8) \times 10^{-5}$ (error is 2σ). The value is consistent with the canonical solar system value of $(5.25 \pm 0.02) \times 10^{-5}$ (Jacobsen et al., 2008; Larsen et al., 2011) within uncertainty.

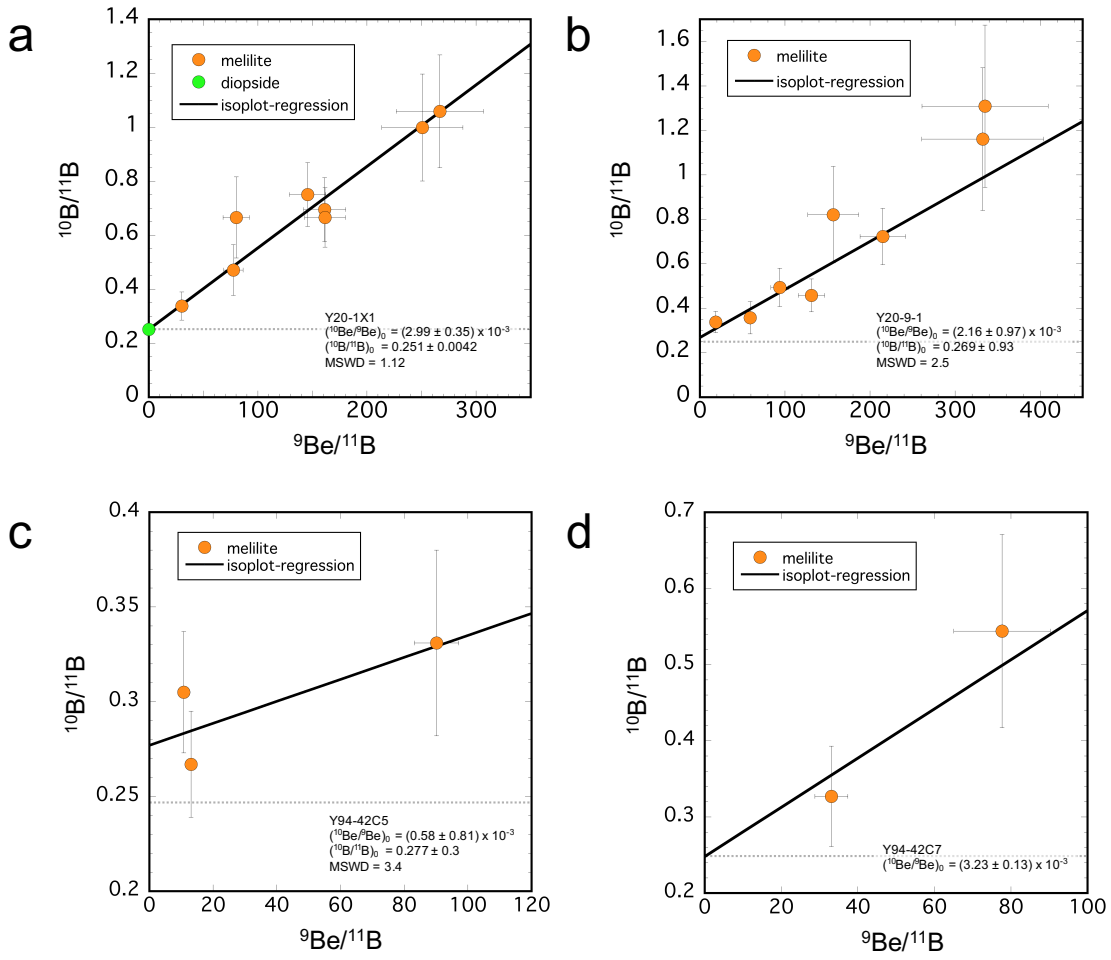

Fig. 3.29. Be-B isochron diagrams for CAIs in the two carbonaceous chondrites. (a) CAI Y20-1X1 in the Y81020 (CO3.05) chondrite. (b) CAI Y20-9-1 in the Y81020 (CO3.05) chondrite. (c) CAI Y94-42C5 in the Y82094 (ungrouped C3.2). (d) CAI Y94-42C7 in the

Y82094 (ungrouped C3.2). The initial $^{10}Be/^{9}Be$ ratio of Y94-42C7 was determined by assuming initial boron isotopic composition ($^{10}B/^{11}B$ =0.2481). Error bars (± 2σ) on both $^{10}B/^{11}B$ and $^{9}Be/^{11}B$ include both an external reproducibility and an internal precision.

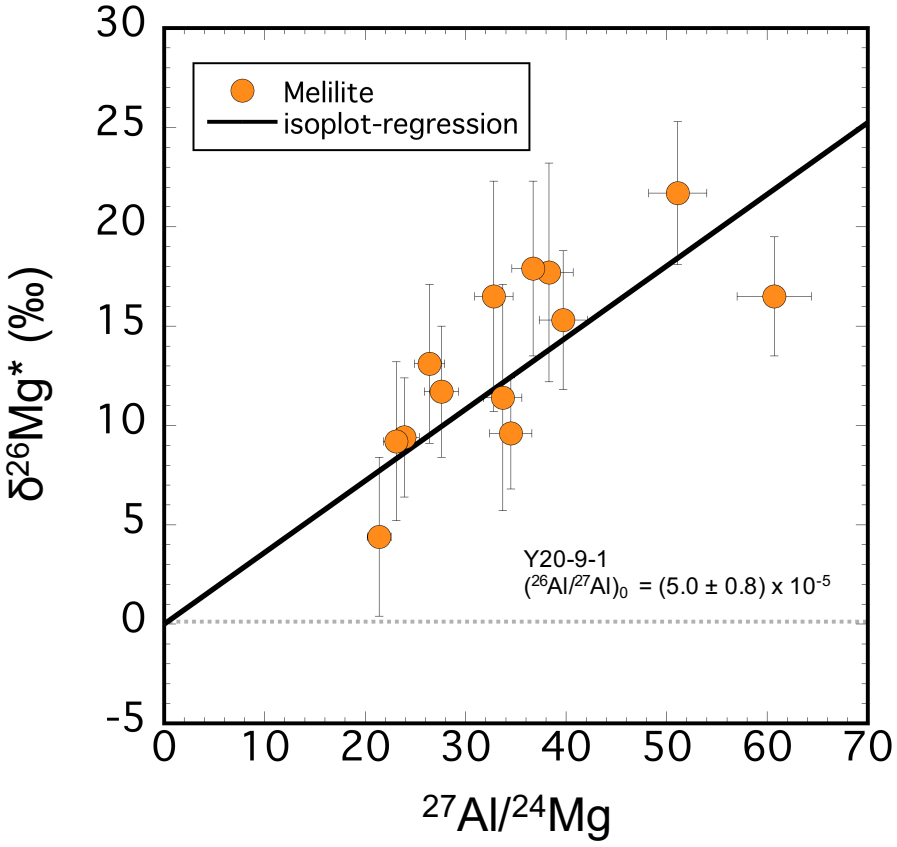

Fig. 3.30. The Al-Mg isochron diagram for the CAI Y20-9-1 in the Y81020 (CO3.05) chondrite. The initial $^{26}Al/^{27}Al$ ratio of Y94-42C7 was determined by assuming the initial magnesium isotopic composition ($\delta^{26}Mg$ = -0.04; Jacobsen et al., 2008). Error bars (± 2σ) on both $\delta^{26}Mg$ and $^{27}Al/^{24}Mg$ include both an external reproducibility and an internal precision.

3.3.2. CH and CH/CBb CAIs

Due to their small sizes, I performed only one or two Be-B analyses for each CH and CH/CBb CAI except for the SA301. Therefore, I calculated $^{10}Be/^{9}Be$ ratios based on model isochrons by assuming a chondritic initial boron isotopic composition ($^{10}B/^{11}B$ = 0.2481) and adopted weighted mean values if two analyses were performed. This assumption may not be valid for Be-B systems in the case that ^{10}Be was produced by SCR irradiation of refractory solids. If this is the case, the initial $^{10}B/^{11}B$ ratios might have been modified by spallogenic components (~0.44: Yiou et al., 1968). However, the SA301, which shows the highest $^{10}Be/^{9}Be$ ratio in this study, yields an internal isochron with the initial $^{10}B/^{11}B$ ratio of 0.11 ± 0.17. Although the error is large, the initial $^{10}B/^{11}B$ ratio is identical to the chondritic value ($^{10}B/^{11}B$ = 0.2481) within uncertainty, indicating that initial $^{10}B/^{11}B$ ratios of CH CAIs are not so high (~0.44), but nearly chondritic. Note that the $^{9}Be/^{11}B$ ratio of grossite in SD103 CAI was calculated using the RSF of NIST 610. This calibration may not be valid for the determination of accurate $^{9}Be/^{11}B$ ratio of grossite. Fortunately, however, grossite in SD103 shows no resolvable excess in ^{10}B within uncertainty (Fig. 3.31a). Thus, there is no effect on following discussions. The inferred $(^{10}Be/^{9}Be)_0$ values thus obtained are highly variable from $(1.7 \pm 3.6) \times 10^{-4}$ to $(40.5 \pm 7.2) \times 10^{-4}$ (errors are 2σ; see Fig. 3.31a and 3.31b).

$^{7}Li/^{6}Li$ ratios of three out of five CH and C/CBb CAIs are slightly lower than that of the chondritic ratio ($^{7}Li/^{6}Li$ = 12.06), but identical to that of the chondritic ratio within uncertainties.

In Fig. 3.32, I plot the Al-Mg isotope systematics of seven CH and CH/CB CAIs. All CAIs studied here do not show resolvable excesses in ^{26}Mg.

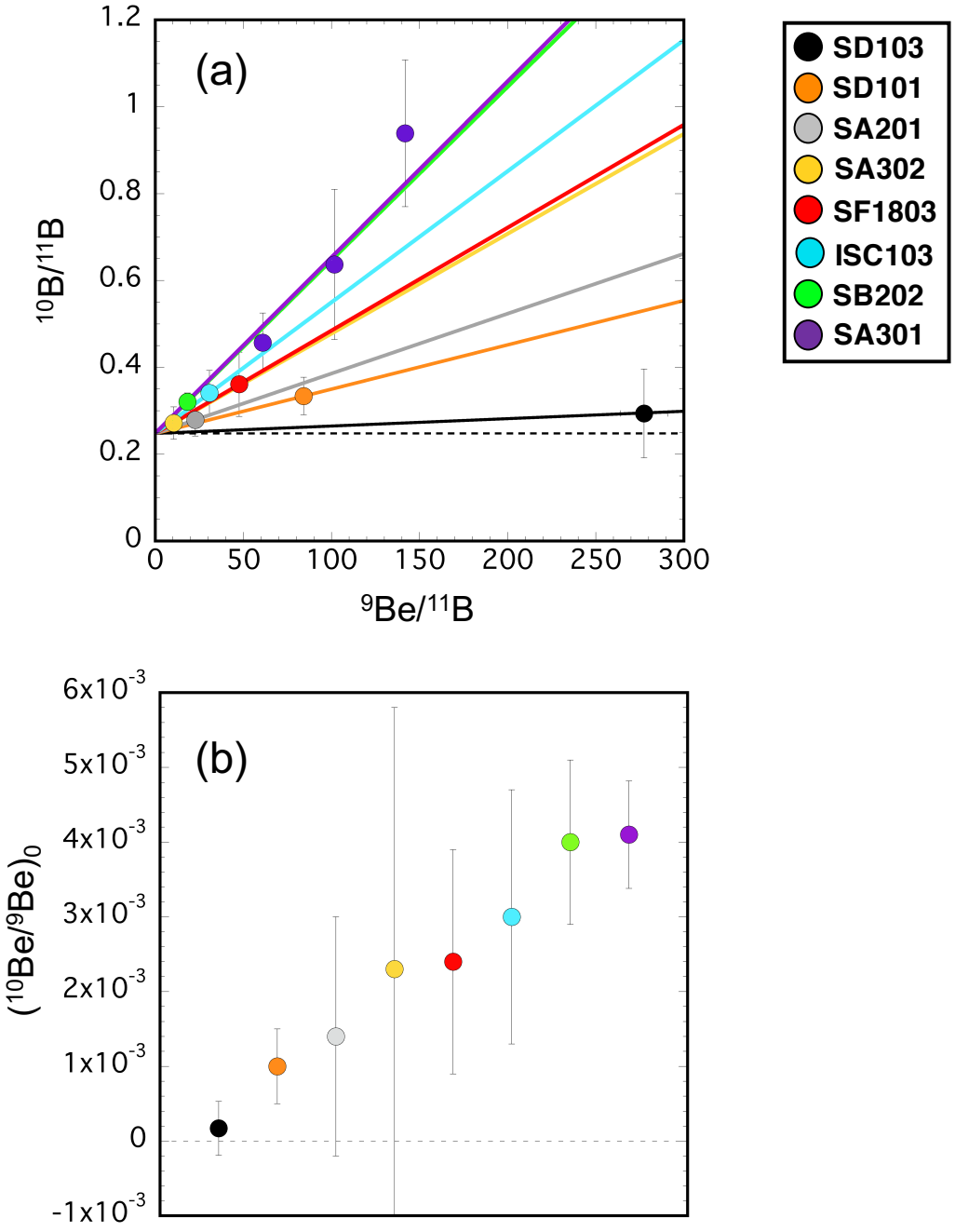

Fig. 3.31. (a) Be-B isochron diagrams for CAIs in the Isheyevo (CH/CBb) and SaU290 (CH3) chondrites. Error bars (± 2σ) on both $^{10}B/^{11}B$ and $^{10}Be/^{11}B$ include both an external reproducibility and an internal precision. (b) Initial $^{10}Be/^{9}Be$ ratios inferred from Fig. 3.30 (a). Note that initial $^{10}Be/^{9}Be$ ratios of each CAI were determined by assuming an initial boron isotopic composition ($^{10}B/^{11}B = 0.2481$).

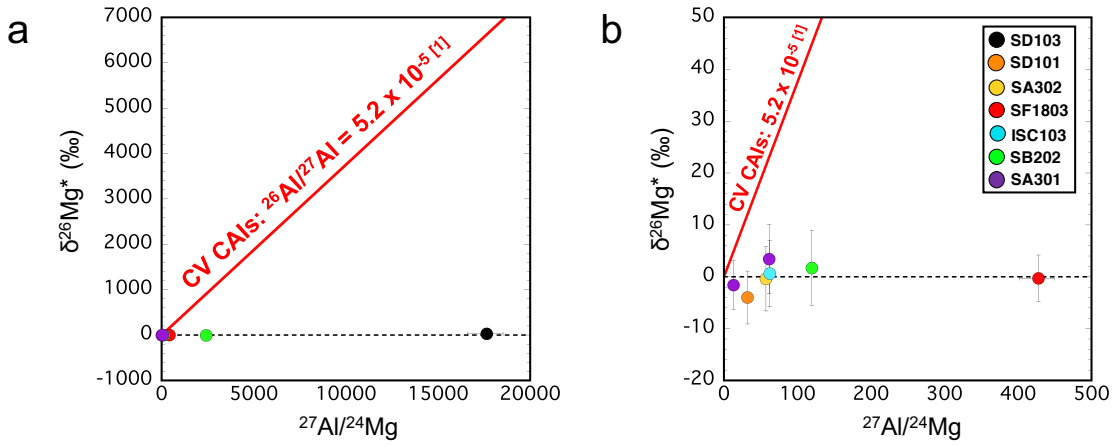

Fig. 3.32. Al-Mg isochron diagrams for CAIs in the Isheyevo and SaU290 chondrite. (b) Enlargement of the low $^{27}Al/^{24}Mg$ region in (a). Error bars (± 2σ) on both $\delta^{26}Mg$ and $^{27}Al/^{24}Mg$ include both an external reproducibility and an internal precision.

3.4. Discussion

3.4.1. Significance of variations in $^{10}Be/^{9}Be$ of CAIs: Are they primary or secondary signatures?

In this study, CO, ungrouped C, CH and CH/CBb CAIs show variable $(^{10}Be/^{9}Be)_0$ values (0.17 - 4.05 × 10^{-3}). If these signatures are resulted from decay of ^{10}Be, the variations in $(^{10}Be/^{9}Be)_0$ would have chronological or spallogenic meanings. However, the variations in $(^{10}Be/^{9}Be)_0$ could also be resulted from secondary processes such as aqueous alteration and thermal metamorphism on parent bodies and/or thermal processing in the solar nebula.

As mentioned above, Y81020 is the least altered carbonaceous chondrite and CAIs in Y81020 show mineralogically pristine and do not contain secondary alteration products (e.g., nepheline, sodalite, and anorthite). CAIs in SaU290 and Isheyevo also show no evidence for secondary alteration. Therefore, these CAIs should preserve

isotopic signatures at the time of CAI formation. On the other hand, CAIs in Y82094 contain some amounts of secondary minerals so that they must have undergone parent body alteration processes (see section 3.2.1). Therefore, it is possible that the Be-B systems of Y82094 CAIs might have been disturbed by these processes. In fact, no ^{10}Be isochron can be inferred from this dataset (Fig. 3.29c). Thus, I hereafter exclude the data of CAIs in Y82094 in the following discussions.

In this study, CH and CH/CBb CAIs show highly variable (^{10}Be/^{9}Be)$_0$ values than that of CV CAIs (Fig. 3.33). If the signatures truly reflect the distribution of ^{10}Be in the proto-solar disk, they are important observations for discussing the origin of ^{10}Be in the early solar system. However, thermal processing in the solar nebula could also generate variations in the apparent ^{10}Be/^{9}Be ratios from initially identical isochrons. It should be noted that about ~10% of CH CAIs might have undergone melting and O-isotope exchange in impact plume events (Krot et al., 2012b, 2017). Thus, the observed variability in ^{10}Be/^{9}Be of CH and CH/CBb CAIs may reflect secondary melting events in the solar nebula. Krot et al. (2008a; 2008b; 2012b; 2017) conducted comprehensive studies of mineralogy, petrography, O- and Mg-isotope compositions of CH and CH/CBb CAIs. They concluded that there are multiple populations/generations of CAIs in these meteorites. Most CH CAIs have small sizes, very refractory mineralogy (rich in grossite, hibonite, Al-rich pyroxene, perovskite, and gehlenitic melilite), typically spherical shapes with low ^{26}Al/^{27}Al ratios of $< 5 \times 10^{-7}$, and a large range of oxygen isotopic compositions (Δ^{17}O range from ~-35‰ to ~-5‰). In addition, Krot et al. (2008b; 2012b; 2017) described a population of the CB-like igneous CAIs composed mainly of less refractory minerals (Ti-poor Al-diopside, spinel, åkermanitic melilite, and forsterite, surrounded by Al-diopside-Ca-rich forsterite igneous rims) and characterized by isotopically uniform ^{16}O-depleted compositions (Δ^{17}O values ranging from ~-10‰ to ~-4‰). Krot et al. (2012b) suggested that isotopically uniform ^{16}O-depleted igneous CAIs in CH and CB chondrites experienced complete melting with gas-melt interaction and O-isotope

exchange in an impact plume, which is invoked for the origin of magnesian, non-porphyritic chondrules in CBs and CHs (Krot et al., 2005; 2010). Most of the CH and CH/CBb CAIs studied here have very refractory mineralogy (rich in grossite, hibonite, gehlenitic melilite ($Åk_{1\text{-}5}$), perovskite, and spinel) and rounded shapes, which are similar to those of typical (~90 % of) CAIs in CH and CH/CBb chondrites (Krot et al., 2008; Zhang et al., 2009). According to Krot et al. (2012b, 2017), ~10 % of the CH CAIs might have experienced melting and O-isotope exchange in impact plume events. Although I have not measured the O isotopic compositions of the present CAIs, their refractory nature suggests that they are representative of the major population of CH and CH/CBb CAIs, which have escaped gas-melt interactions in an impact plume.

Note that diffusivity of boron is generally much lower than that of oxygen in silicates. For example, diffusion coefficient of boron in SiO_2 was reported as 1.7×10^{-23} m^2/s at 1000 ℃ (Aoyama et al., 1999), which is 5 orders of magnitude lower than that of oxygen in melilite (1.8×10^{-18} m^2/s at 1000 ℃; Ryerson and McKeegan, 1994). Hence, if CH and CH/CBb CAIs studied here have not undergone melting and O-isotope exchange in impact plume events, the B isotope signatures of these CAIs should be preserved.

However, it is also pointed out that CH and CH/CBb CAIs surrounded by the Al-diopside and forsterite rim tend to show ^{16}O-depleted compositions (Krot et al., 2017). Among the present CAIs, SA301, SD101, and ISC103 have Al-diopside and forsterite rim, suggesting a possibility of their interaction with an impact plume. However, SA 301, which has apparent igneous textures and is surrounded by Al-diopside and forsterite rim (Fig. 3.21), shows the highest $(^{10}Be/^{9}Be)_0$ value of $(4.1 \pm 0.7) \times 10^{-3}$ in the present study, and CAI ISC 103, which is also surrounded by Al-diopside and forsterite rim (Fig. 3.12b), also shows a rather high $(^{10}Be/^{9}Be)_0$ value of $(3.0 \pm 1.7) \times 10^{-3}$. Thus, there seems no systematic correlation between $(^{10}Be/^{9}Be)_0$ values and CAI textures. These observations suggest that variable $(^{10}Be/^{9}Be)_0$ values of CH and CH/CBb CAIs do *not* reflect variations

produced by thermal processing related to an impact plume, but most likely reflect differences in formation timing and/or spallogenic contributions.

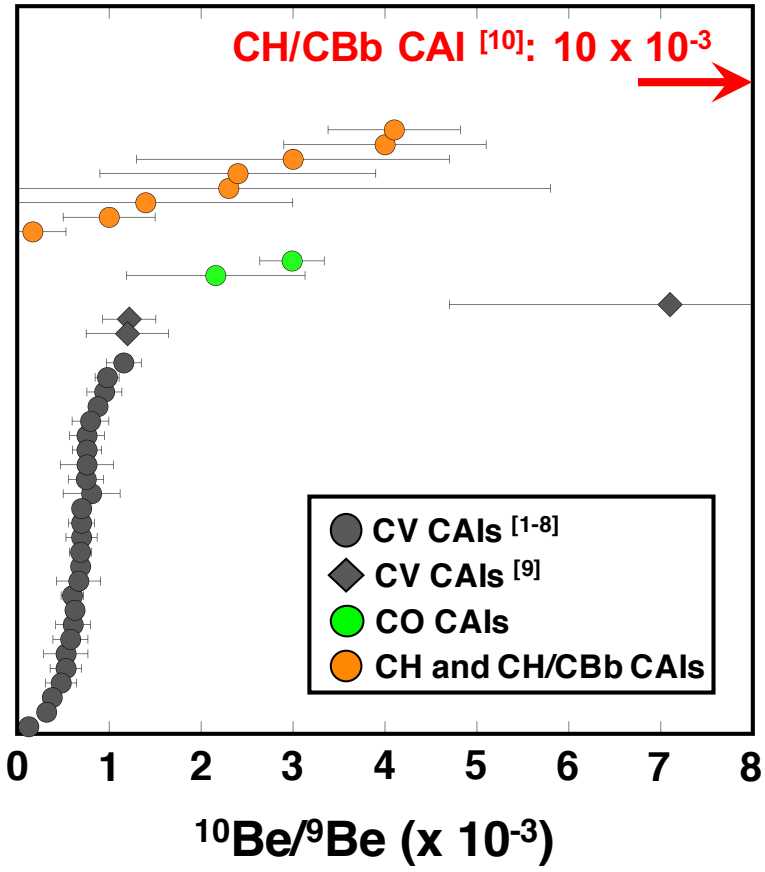

Fig. 3.33. Summary of the inferred initial $^{10}Be/^{9}Be$ ratios of the CAIs in this study and comparison with previous data ([1] McKeegan et al., 2000; [2] Sugiura et al., 2001; [3] MacPherson et al., 2003; [4] Chaussidon et al., 2006; [5] Wielandt et al., 2012; [6] Srinivasan and Chaussidon, 2013; [7] Dunham et al., 2016; [8] Dunham et al., 2017; [9] Sossi et al., 2017; [10] Gounelle et al., 2013).

3.4.2. High and variable $^{10}Be/^{9}Be$ ratios in CO, ungrouped C, CH and CH/CBb CAIs and their implications for the origin of ^{10}Be in the early solar system

As described in chapter 1, the origin of ^{10}Be in the early solar system remain controversial. At present, three models are proposed by previous studies: (1) molecular cloud origin (Desch et al., 2004; Tatischeff et al., 2014), (2) neutrino processes with core-collapse supernovae (Banerjee et al., 2016), and (3) solar cosmic ray irradiation origin (e.g., McKeegan et al., 2000; Gounelle et al., 2001). In this section, I evaluate the models for the origin of ^{10}Be in the early solar system based on the obtained meteoritic data.

Desch et al. (2004) first proposed the molecular cloud origin of ^{10}Be as trapped GCR components by the presolar molecular cloud core. Because the spatial scale of the molecular cloud core is so much larger than that of the solar system, ^{10}Be would be homogeneously distributed in the solar nebula. In this model, the variation of $^{10}Be/^{9}Be$ ratios in CAIs could be interpreted as different formation times of CAIs. If this is the case, it would imply that SA301, which shows the highest $^{10}Be/^{9}Be$ ratio of $(4.1 \pm 0.7) \times 10^{-3}$ in this study, formed 6.9 Myr before the NWA 6991 ($CV3_{ox}$) CAI B4 whose initial $^{10}Be/^{9}Be$ ratio is $(0.13 \pm 0.05) \times 10^{-3}$ (Dunham et al., 2017). The NWA 6991 CAI B4 has an ancient absolute Pb-Pb age of 4567.94 ± 0.31 Ma (Bouvier et al., 2011). Thus, the initial $^{10}Be/^{9}Be$ ratio of SA301 corresponds to the absolute age of $4574.83\ ^{+0.33}_{-0.39}$ Ma. However, considering a lifetime of the YSOs (~10 Myr; see chapter 1) and the formation of CV3 CAIs is thought to have happened during the earliest phases of the proto-solar disk (e.g., Kita et al., 2013), the very early formation of SA301 is unlikely.

Alternatively, if the variation in $^{10}Be/^{9}Be$ ratios of CAIs reflects the isotopic heterogeneity within the protosolar disk, a correlation between the variation in $^{10}Be/^{9}Be$ and isotopic anomalies would be expected. In contrast to normal CAIs, FUN CAIs are characterized by large (up to a few permil) mass-independent isotope anomalies in several

elements (e.g., calcium and titanium: Park et al. (2014) and reference therein), suggesting that FUN CAIs may have formed before isotopic homogenization in the protosolar disk. However, as mentioned in chapter 2, $^{10}Be/^{9}Be$ ratios of CV FUN CAIs are within the range of normal CAIs (see Fig.2.3). The no clear relationship between $^{10}Be/^{9}Be$ ratios and presence or absence of mass-independent isotopic anomalies in Ca and Ti implies that the variation in $^{10}Be/^{9}Be$ ratios of CAIs would not reflect the isotopic heterogeneity within the protosolar disk.

Tatischeff et al. (2014) demonstrated that irradiation of presolar molecular cloud by background GCRs produced a steady-state $^{10}Be/^{9}Be$ ratio of $\leq 1.3 \times 10^{-4}$ at the time of solar system formation, which is significantly lower than the observed $^{10}Be/^{9}Be$ ratios in this study. Tatischeff et al. (2014) also considered irradiation of the presolar molecular cloud by freshly accelerated cosmic rays escaped from an isolated supernova remnant so that the solar system formed with background ^{10}Be at a level of 3×10^{-4}. This is also lower than the observed $^{10}Be/^{9}Be$ ratios in this study. Furthermore, this model invokes rather extreme astrophysical conditions and may not be a realistic situation for the solar system formation.

Recently, Banerjee et al. (2016) showed that ^{10}Be is produced by the neutrino spallation process with low mass core-collapse supernovae. They found that this model can produce ^{10}Be at a level of $^{10}Be/^{9}Be = (5.2\text{-}6.4) \times 10^{-4}$. However, the inferred $^{10}Be/^{9}Be$ ratio by Banerjee et al. (2016) is much lower than most of the inferred $^{10}Be/^{9}Be$ ratios of CAIs observed in this study. Thus, this model is inadequate to explain the observed $^{10}Be/^{9}Be$ ratios in this study.

According to discussions above, the inheritance from the molecular cloud and the neutrino spallation models cannot account for the observed $^{10}Be/^{9}Be$ ratios of CO, CH, and CH/CBb CAIs. Hereafter, I consider a scenario that ^{10}Be was produced by a solar cosmic ray irradiation. McKeegan et al. (2000) first proposed the solar cosmic ray irradiation model for the origin of ^{10}Be in the early solar system. This model can produce

variable ^{10}Be abundances. Although the production rate of ^{10}Be by solar cosmic ray irradiation model depends on irradiation conditions, such as target composition, solar cosmic ray flux, irradiation time, and distance from the proto-sun, it can in principle be possible to explain the ^{10}Be/^{9}Be ratios observed in this study.

Here, I show calculated ^{10}Be production rates by solar cosmic ray irradiation. Irradiation models for the production of elements have been introduced very early by astrophysicists (Fowler et al., 1962). Their principle is extremely simple: Accelerated particles with MeV or higher energies react with ambient matter to produce new isotopes via nuclear reactions. For a nuclear reaction between a cosmic ray and a target producing the ^{10}Be (mostly ^{16}O), the production ratio of ^{10}Be relative to ^{9}Be can be written as

$$\frac{[^{10}\mathrm{Be}]}{[^{9}\mathrm{Be}]} = \frac{[^{16}\mathrm{O}]}{[^{9}\mathrm{Be}]} \frac{\Delta t}{R^2} \sum_i y_i \int \sigma_i(E) \frac{dF}{dE} dE \qquad \dots (1)$$

where Δt is the irradiation time, R is the irradiation distance from the sun, y_i is the relative abundance of cosmic ray species (^{3}He, ^{4}He) relative to proton, $\sigma_i(E)$ is the cross section of considered nuclear reaction, and dF/dE is the proton differential flux, F is the flux, and E is the energy. The proton differential flux can be written as

$$\frac{dF}{dE} = KE^{-\gamma} \qquad \dots (2)$$

where the γ is the spectral slope, which quantifies the relative abundance of high- and low-energy protons. For example, impulsive solar flare events are characterized by a steep energy spectrum with a high γ (=3.5) and high abundances of ^{3}He, whereas gradual flares are described by a shallower spectral index (a low γ) and lower ^{3}He abundances (Lee et al., 1998; Gounelle et al., 2001). As nominal conditions, I use the ratios ^{4}He/proton = 0.1 and ^{3}He/^{4}He = 0.1 that characterize gradual flares (γ = 2.5) from the present-day Sun (Reames et al., 1999) and cross sections (cosmic rays + ^{16}O $\rightarrow$ ^{10}Be) given by Gounelle

et al. (2006). In this calculation, I assumed that a target of irradiation has a chondritic composition (see the next section). I adopt the total proton flux estimated by Lee et al. (1998) based upon the X-ray observations of embedded young solar-type stars (e.g., Kamata et al., 1997; Feigelson et al., 2002a, 2002b), with F_p (E ≥ 10 MeV) = 1.9×10^{10} cm^{-2} s^{-1} (at R = 0.07AU). Assuming these parameters, it is possible to calculate the $^{10}Be/^{9}Be$ ratio as a function of the irradiation time and the irradiation distance from the Sun.

Fig. 3.34 shows a relationship between irradiation-produced $^{10}Be/^{9}Be$ ratios and irradiation time at R = 1 and 0.1 AU. Recently, Desch et al. (2017) simulated the evolution of temperature in the protoplanetary disk. The results demonstrated that inside of about 1 AU, temperatures are high enough, T > 1400 K, to allow CAI formation (Fig. 3.35). Moreover, the high-temperature mineralogy and geochemistry of CAIs suggest that they possibly formed at the inner edge of the disk, R < 0.1 AU (Wood, 2004). Thus, I calculated the $^{10}Be/^{9}Be$ ratios as a function of irradiation time at R = 1 AU and 0.1 AU. Under these conditions, the observed range of $^{10}Be/^{9}Be$ ratios (0.17 to 4.05×10^{-3}) of CAIs can be explained by irradiation times varying from a few years to 90 years (R = 0.1 AU) and 250 to 9,000 years (R = 1 AU). These time scales are broadly consistent with the lifetime of CAI precursors that are very short time interval (< 20,000 years) based on the Al-Mg and U-Pb systematics (Jacobsen et al., 2008; Larsen et al., 2011). In three models described above, therefore, new Be-B data obtained from this study support the solar cosmic ray irradiation model for the origin of ^{10}Be in the early solar system.

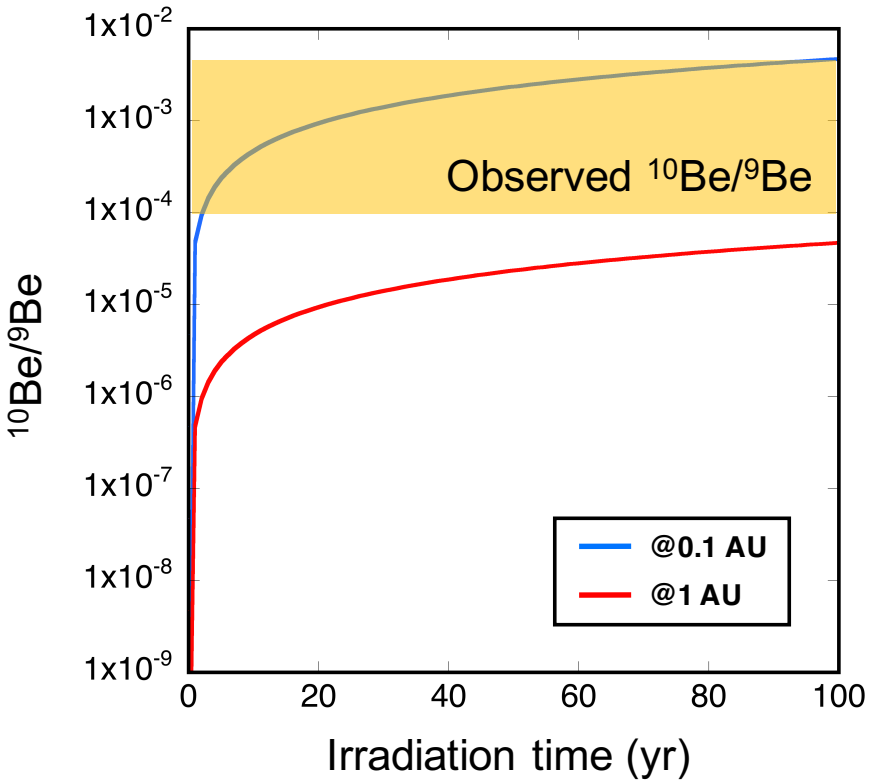

Fig. 3.34. An example of the calculation results of irradiation-produced $^{10}Be/^{9}Be$ ratios as a function of the irradiation distance (R) and irradiation time (Δt). An orange region represents the observed $^{10}Be/^{9}Be$ ratios of CAIs in this study.

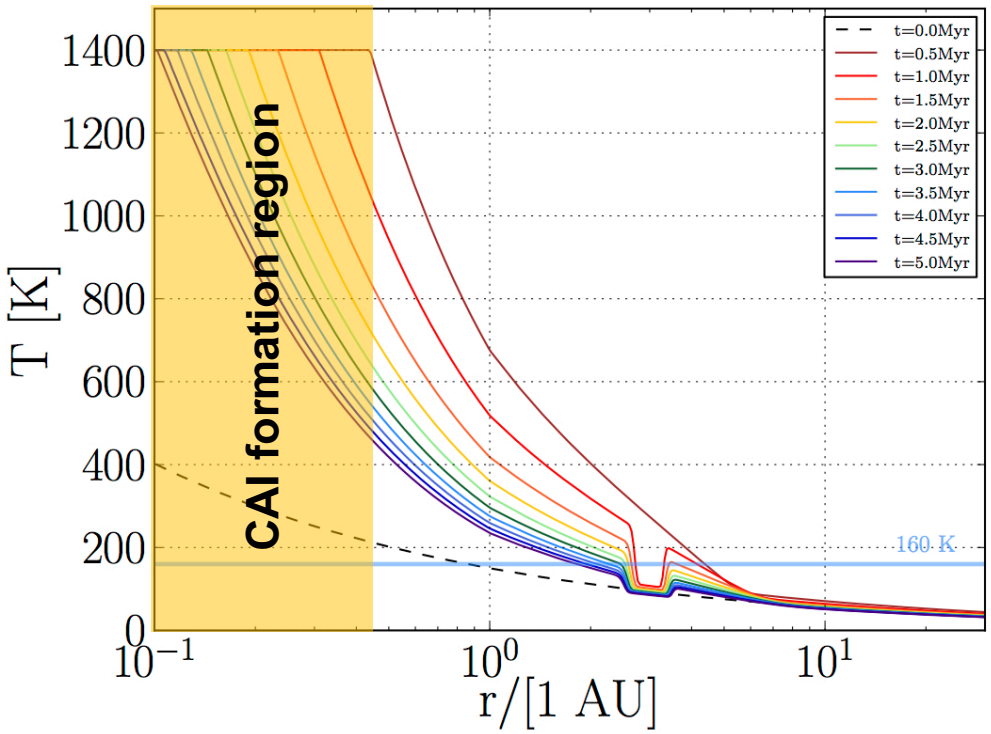

Fig. 3.35. Temperatures at various times in the disk's evolution. The black dashed curve donates a passive disk temperature profile $T = 160\ (r/1\ AU)^{-3/7}$K, for comparison. Colored profiles of maroon, red, to violet show temperature profiles at t = 0.5, 1.0 to 5.0 Myr, respectively. Inside about 1 AU, temperatures are high enough, T > 1400 K, to allow CAI formation. Desch et al. (2017) cap the temperature at 1400 K to account for the fact that at high temperatures the silicates would vaporize, greatly decreasing the opacity. Jupiter opens a gap at 3 AU at 0.6 Myr. After Desch et al. (2017).

3.4.3. Li-Be-B systematics on CO, CH and CH/CBb CAIs and targets of irradiation by cosmic rays

As mentioned in the section 3.4.2, the solar cosmic ray irradiation model is appropriate for the origin of most of ^{10}Be in the early solar system. If this is correct, not only ^{10}Be but also $^{6, 7}$Li and $^{10, 11}$B are produced by the process. Thus, Li and B isotopic compositions would be affected by solar cosmic ray irradiation. The spallation effects for Li and B isotopic compositions are highly dependent on chemical compositions of irradiation targets. In order to deduce irradiation targets, I estimated irradiation effects on ^{7}Li/^{6}Li and ^{10}B/^{11}B using the observed ^{10}Be/^{9}Be ratios and spallation production ratios (Yiou et al., 1968). I assumed that (1) spallation are induced by irradiation by protons with 135 MeV, (2) pre-irradiation ^{7}Li/^{6}Li and ^{10}B/^{11}B of targets are chondritic compositions (^{7}Li/^{6}Li = 12.02, Seitz et al. 2009; ^{10}B/^{11}B = 0.2481, Zhai et al., 1996), and (3) pre-irradiation Li, Be, and B concentrations are the same as those deduced from the NanoSIMS measurements. Note that (3) is not a reasonable assumption because present concentrations are considered to be mixtures of pre-irradiation and spallation products. Thus, pre-irradiation concentrations assumed here are upper limits. In principle, however, targets with less Li and B concentrations would show more Li and B isotopic shifts. In other words, the calculated results represent minimum degrees of isotopic shifts by irradiation. Examples of the calculation results for Li are shown in Fig. 3.36. ^{10}Be/^{9}Be ratios and Li isotopic compositions of CAIs are also shown.

Here, I consider two possible irradiation scenarios: irradiation of CAI themselves and irradiation of solar gas. In the first scenario, there was in situ irradiation of already formed CAI solids near the proto-Sun. Because of high Be/Li and Be/B ratios, ^{7}Li/^{6}Li and ^{10}B/^{11}B of CAIs should be modified immediately. The results of the irradiation calculations are not consistent with the observed isotopic ratios of CO, CH and CH/CBb CAIs (Fig. 3.36). For example, if the CAI solid (Li ~600 ppb, Be ~700 ppb, and B ~10

ppb) was irradiated and ^{10}Be was produced at a level of $^{10}Be/^{9}Be = 3.0 \times 10^{-3}$, the expected $^{7}Li/^{6}Li$ and $^{10}B/^{11}B$ ratios are ~1.8 and ~0.43, respectively. The calculated ratios are significantly different from those of CO, CH, and CH/CBb CAIs.

In the second scenario, proton was irradiated to the solar nebular gas, and CAI or CAI precursors were condensed from the irradiated solar gas. The initial gas composition is taken as the solar composition of Lodders (2009). Solar Be/Li and Be/B ratios are three or four orders of magnitude lower than those of CAI solids, so that isotopic modification by proton irradiation are less effective. The calculated results are consistent with the observed isotopic $^{7}Li/^{6}Li$ and initial $^{10}B/^{11}B$ ratios in this study. Hence, the present results suggest that ^{10}Be was not produced by irradiation of CAI solids, but by irradiation of their precursors, possibly a solar nebula gas.

However, it is possible that the observed chondritic $^{7}Li/^{6}Li$ ratios of CH CAIs are attributed to secondary processes, such as diffusion and mixing processes. The diffusion of Li in melilite, has not been studied. But generally speaking Li diffusion in silicates is expected to be faster than other elements (e.g., Coogan et al., 2005; Zhang et al., 2010). For example, Li and Mg diffusion rates in anorthite were reported as 1.6×10^{-10} m^2/s and 2.7×10^{-18} m^2/s, respectively at 1000 ℃ (Giletti and Shanahan, 1997; LaTourrette and Wasserburg, 1998). If I assume that the Li diffusion rate in melilite is comparable to that of anorthite, Li in a melilite grain (100 μm × 100 μm) could be equilibrated by 130 seconds at 1000℃. Therefore, I cannot rule out this possibility. Mixing processes also produce the chodritic $^{7}Li/^{6}Li$ with high $^{10}Be/^{9}Be$. However, except for CAI Y20-1X1, Li concentrations of melilite in CAIs studied here are ranging from 26 to 71 ppb, which is roughly comparable with those of expected spallogenic Li concentrations (~30 ppb) with $^{10}Be/^{9}Be = \sim 4 \times 10^{-3}$. Thus, if the measured Li concentrations were accompanied by mixing between spallogenic and chondritic components, the Li isotopic compositions should appear to be more spallogenic isotopic compositions. This is inconsistent with our observations. However, if the near totality of the Li budget was exchanged with a

reservoir of the chondritic Li-isotope composition, it is possible to explain both observed low Li concentrations and chondritic Li isotopic compositions.

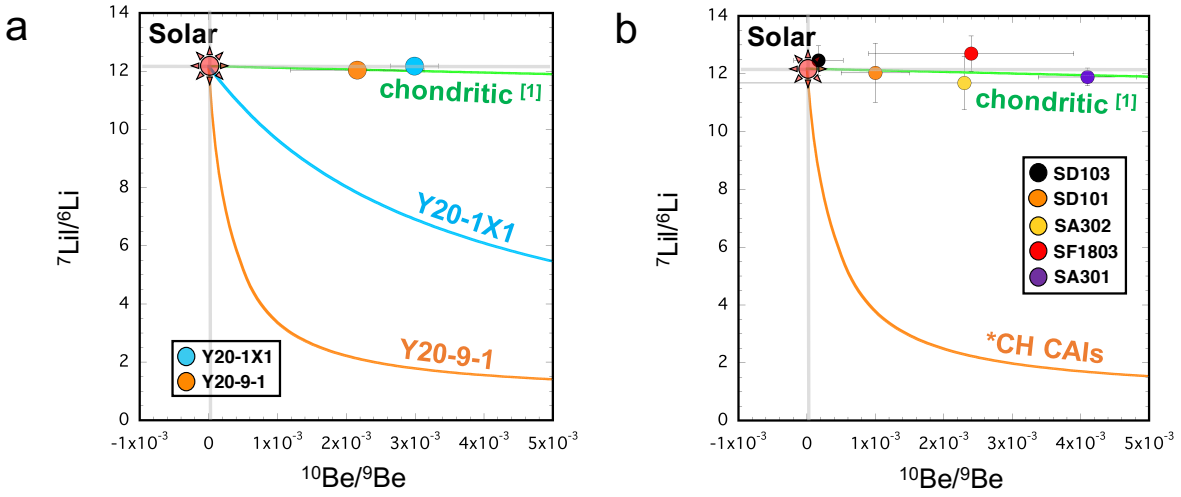

Fig. 3.36. Examples of calculation results of irradiation-produced ^{7}Li/^{6}Li ratios as a function of ^{10}Be/^{9}Be ratios in comparison with the present data. Green curves represent the case of irradiation of the chondritic material (Be/Li = 0.014; [1] Lodders, 2009) (a) In the case of CAIs in the Y81020 (CO3.05) chondrite. (b) In the case of CAIs in the SaU290 (CH3) chondrite. The orange curve is calculated using an average value of Be/Li in CH CAIs.

MacPherson et al. (2003) conducted Li-Be-B isotopic measurements on Type A CAIs in CV chondrites. Figure 3.37 shows the relationship between ^{10}Be/^{9}Be ratios and Li isotopic compositions of CV CAIs measured by MacPherson et al. (2003). The reported isotopic compositions of CV CAIs cannot be explained by irradiation of CAI themselves, which are consistent with the conclusion in this study. However, the Li isotopic compositions of CV CAIs are slightly lower than those to be expected by the case for irradiation of chondritic materials (see Fig. 3.37), suggesting that the target of irradiation for CV CAIs would be slightly fractionated solar gases.

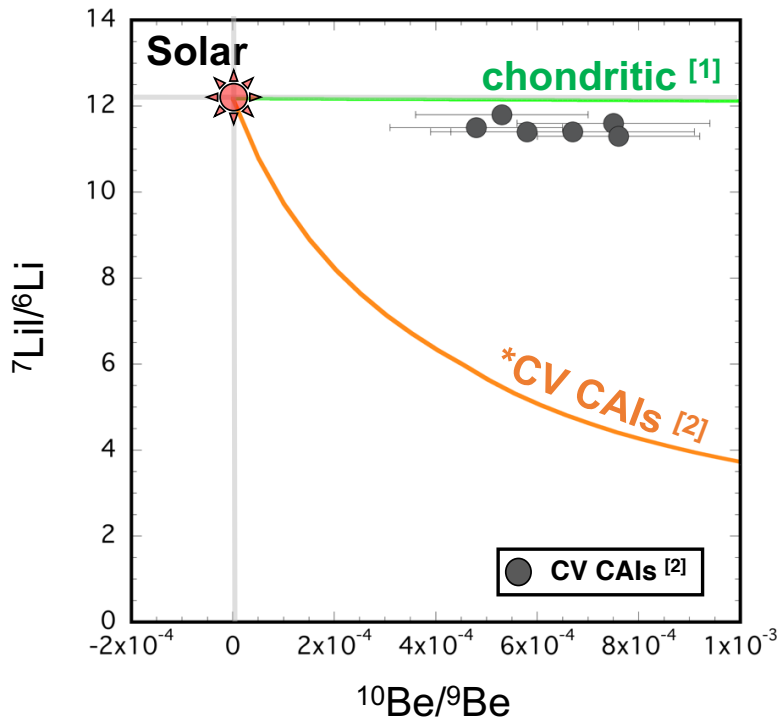

Fig. 3.37. The relationship between irradiation-produced ^{7}Li/^{6}Li ratios as a function of ^{10}Be/^{9}Be ratios in comparison with the data of CV CAIs ([2]: MacPerson et al., 2003). Green curves represent the case of irradiation of the chondritic material (Be/Li = 0.014; [1] Lodders, 2009). The orange curve is calculated using an average value of Be/Li in CV CAIs measured by [2].

Recently, Sossi et al. (2017) reported a co-variation between ^{50}V excesses and ^{10}Be/^{9}Be ratios in CV CAIs. Just as the case for ^{10}Be, ^{50}V is also produced by a cosmic ray spallation process (Fowler, 1962). Thus, the observed co-variation between ^{50}V excesses and ^{10}Be/^{9}Be ratios in CV CAIs implies that excesses of ^{50}V and ^{10}Be were synthesized through irradiation processes. Because the initial ^{10}Be/^{9}Be ratio varies sympathetically with the types of CAIs (fine- vs coarse-grained), the REE patterns (HREE-depleted vs unfractionated), and the ^{50}V excesses (δ ^{50}V ~0 vs negative), Sossi

et al. (2017) suggests that irradiation occurs on not a solar gas, but CAI themselves or their precursors. This conclusion is clearly inconsistent with the above scenario for CO, CH and CH/CBb CAIs. As mentioned above, however, if the irradiation occurs on the CAI themselves, the initial $^{10}B/^{11}B$ ratio must also be modified by spallogenic components. However, the initial $^{10}B/^{11}B$ ratios of all CAIs measured by Sossi et al. (2017) are identical to the chondritic value within uncertainties ($^{10}B/^{11}B$ = 0.2463 ± 0.0022, 0.2450 ± 0.011, and 0.2453 ± 0.0099). This is inconsistent with the scenario of irradiation of CAI themselves. Furthermore, the reported $(^{10}Be/^{9}Be)_0$ values of fine-grained CAIs in Sossi et al. (2017) must be considered with caution. Because of the fine-grained texture of these CAIs, their B isotope data may be significantly affected by contaminations of chondritic (and also terrestrial) boron. In fact, their B concentrations (~500 ppb) are significantly higher than those of coarse-grained CAIs measured by Sossi et al. (2017) (40 ppb) and CAIs in this study (~ 70 ppb). Recently, Liu et al. (2017) reported boron isotopic compositions of a fine-grained CAI in the ALH 77307 (CO3.00) chondrite. They conducted a careful analysis using a CAMECA ims-1290 with a high brightness oxygen primary ion source, which improved a spatial resolution higher than that of NanoSIMS 50. They found elevated, yet uniform within errors, $^{10}B/^{11}B$ ratios (weighted average = 30.2 ± 17.7 ‰, 2σ) independent of $^{9}Be/^{11}B$ ratios. Thus, no ^{10}Be isochron can be inferred from this dataset. The result of Liu et al. (2017) is inconsistent with those of Sossi et al. (2017). Further studies are needed for confirmation of the ^{10}Be abundances in fine-grained CAIs.

^{138}La, which is also produced by the low energy reaction ^{138}Ba (p, n) and, to a lesser extent, by ^{140}Ce spallation. Shen and Lee (2003) first reported La isotopic compositions of seven CAIs in the Allende meteorite. Five out of the seven have well-resolved positive anomalies with an average of 3 ‰, suggesting the existence of irradiation effects. If irradiation occurs on CAI themselves, large excesses in ^{138}La (from +20 to +270 ‰) would be expected for proton fluences necessary to produce ^{10}Be in CV

CAIs (e.g., Burnett et al., 2015), which is not consistent with the degree of observed isotopic anomaly reported in Shen and Lee (2003). Recently, Hidaka and Yoneda (2017) conducted a combined study of La and Sm isotopic measurements of CAIs in the Allende meteorite. Because ^{149}Sm has a large cross section for thermal neutrons, forming a stable isotope ^{150}Sm, search for the isotopic shift of ^{150}Sm/^{149}Sm is useful in interpreting the irradiation history of meteoritic components. CAIs measured by Hidaka and Yoneda (2017) show well-resolved positive anomalies in ^{138}La (from 6 to 9 ‰), which are broadly consistent with the data in Shen and Lee (2003). On the other hand, ^{150}Sm/^{149}Sm ratios of these CAIs do not show isotopic shifts from the chondritic value. If the ^{138}La was produced by irradiation of CAI themselves, the ^{50}Sm/^{149}Sm ratio must also be modified by the neutron capture process. Thus, absence of the isotopic shift in ^{150}Sm/^{149}Sm ratios of Allende CAIs with the excess in ^{138}La can be interpreted as ^{138}La to be produced by irradiation of a solar nebular gas. In this case, spallation-induced neutrons will not significantly lose their energy because of relatively low density of a solar gas. Consequently, excesses in ^{138}La was produced by irradiation with no evidence for the isotopic shift in ^{150}Sm/^{149}Sm ratio. The above scenario is consistent with my conclusion from Li-Be-B systematics in CO and CH CAIs. However, I cannot exclude a possibility that ^{138}La was synthesized by a neutrino process (Woosley et al. 1990). In fact, a correlation between ^{138}La and ^{50}Ti excesses in CAIs was observed by Chen et al. (2015). The correlation suggests that ^{138}La and ^{50}Ti isotopic anomalies was made of mixtures between grains condensed from ejecta of neutron-rich accretion-induced supernovae Ia and the O/Ne-O/C zone of core-collapse supernovae II (Chen et al., 2015). However, if Li-Be-B systematics obtained in the present study are included, irradiation of a solar gas is strongly suggested. Future combined isotope studies of Li-Be-B, V, La, and Sm should disentangle the origin of their isotopic variations in CAIs and targets of irradiation by solar cosmic rays.

3.4.4. Origins of the variations in $^{10}Be/^{9}Be$ and its implication for the evolution of the protosolar disk

The present results and previous studies revealed that the initial $^{10}Be/^{9}Be$ ratios of CAIs are highly variable (10^{-4} to 10^{-2}). In this section, I discuss possible origins of the variations in$^{10}Be/^{9}Be$ ratios of CAIs.

In the section of 3.4.2, I concluded that most of ^{10}Be in CAIs was produced by solar cosmic ray irradiation because this model can explain both high and variable $^{10}Be/^{9}Be$ ratios observed in CAIs. As mentioned above, $^{10}Be/^{9}Be$ ratios depend on target composition, irradiation time, irradiation distance from the proto-sun, and solar cosmic ray flux. Here, I discuss these parameter dependences.

As shown in Equation (1), the ^{10}Be production rate is proportional to the $^{16}O/^{9}Be$ ratio of the target. In section 3.4.2, I consider two possible irradiation scenarios: irradiation of CAI themselves and irradiation of solar gas. In the former case, the average of the $^{16}O/^{9}Be$ atomic ratios of CAI studied here is 3.8×10^{5}. In the latter case, the $^{16}O/^{9}Be$ atomic ratio is 1.9×10^{7} (Lodders et al., 2003), which is higher than the former case by a factor of 50. Thus, if irradiation targets exist both CAI solids and solar gas, it is possible to explain some aspects of the variation in $^{10}Be/^{9}Be$ ratios. For example, fluffy type A CAIs, which are believed to be direct solid condensates from hot solar nebular gas (Grossman 1975), should have higher $^{10}Be/^{9}Be$ than those of CAIs that have experienced solid-state irradiation. More data from such inclusions will be needed to verify this hypothesis.

Irradiation time and distance from the proto-Sun are highly dependent on CAI formation history. At present, the CAI formation mechanism, such as formation location, is not well known. However, several hires of evidence imply that CAIs formed near the proto-Sun. First, oxygen isotopic compositions of CAIs in pristine chondrites are enriched in ^{16}O by approximately 50‰ compared to terrestrial mantle (Ushikubo et al., 2017 and

reference therein) and are similar to those of the Sun inferred from the analyses of solar wind returned by the *Genesis* spacecraft (McKeegan et al. 2011). On the other hand, other planetary materials such as Earth, Mars, and bulk meteorites show ^{16}O-depleted oxygen isotopic compositions (e.g., Scott and Krot, 2014). These oxygen isotopic differences between CAIs and other planetary materials suggest that at least CAIs have formed near the Sun. Second, the mineralogy and major element chemistry of CAIs are generally similar to those for solids in equilibrium with a high-temperature (T > 1400 K) gas of solar composition (e.g., Grossman et al., 2000). These signatures indicate that CAIs formed from a gas of approximately solar composition in the hot innermost region of the proto-solar disk. As mentioned above, Desch et al. (2017) simulated the evolution of temperature in the protoplanetary disk. The results demonstrated that inside about 1 AU, temperatures are high enough, T > 1400 K, to allow CAI formation (Fig. 3.35). If the CAI formation occurred continuously between 0.1 and 1 AU, it may be possible to explain the variation in ^{10}Be/^{9}Be ratios in CAIs (Fig. 3.34).

The cosmic ray flux from the proto-Sun is highly unclear. If the proton flux from the proto-Sun has changed by an order of ~2, it could be possible to explain the variation in ^{10}Be/^{9}Be ratios in CAIs. The energy source of the proto-Sun was the gravitational energy release of the accreting materials, and hence, the activity of the proto-Sun, or the proton flux from the proto-Sun, must be a strong function of the accretion rate. Therefore, episodic accretion events would be a candidate of the cause for the variation in the number flux of protons. During star formation, the rate of accretion of circumstellar disk material onto the pre-main sequence star is not constant. Sharp order-of-magnitude enhancements in the mass accretion rate called “accretion outbursts” have long been known to occur in young stars (Herbig 1977). Historically, two classes of eruptive young stars have been observationally identified. FU Orionis outbursts (FUors) are characterized by bursts in bolometric luminosities of ~500 $L_{\odot}$ with accretion rates up to ~10^{-4} $M_{\odot}$ yr^{-1}, and durations of hundreds of years (Hartmann & Kenyon, 1996), while EX Lupi outbursts (EXors)

show episodic outbursts that are a factor of ~100 weaker both in accretion rate and duration (Herbig, 2007 and reference therein). It is known that X-ray luminosity (L_x) increases with stellar luminosity (L_{star}) in T Tauri stars (Preibisch et al., 2005; Telleschi et al., 2007). Therefore, such episodic accretion events should produce high energetic particle fluxes around the central star. In fact, intensive X-ray luminosities (log *Lx* = 29 ~32 erg s^{-1}) have been detected by *XMN-Newton* and *Chandra* X-ray detection of FUori-type outbursts (Skinner et al., 2009; Liebhart et al., 2014), which is higher by an order of magnitude than normal classical T Tauri stars (log *Lx* = ~29 erg s^{-1}; Liebhart et al., 2014). Although the physical reason why *Lx* increased by about an order of magnitude during outburst is not yet clear, it may be possible to explain the variation in $^{10}Be/^{9}Be$ ratios in CAIs, that is, a higher variation in the mass accretion rate may correspond to a higher variation in the proton flux.

If the variation in $^{10}Be/^{9}Be$ ratios of CAIs reflects those episodic accretion events, $^{10}Be/^{9}Be$ ratios of CH and CH/CB CAIs observed in this study would give important constraints on the evolution of the proto-solar disk. Astronomical observations suggest that FUori-type outbursts are confined to the first few tens of thousands of years (Fig. 3.38), which correspond to class I at the stage of the protoplanetary disk evolution (Schulz, 2012). I propose that high and variable $^{10}Be/^{9}Be$ ratios recorded in CH and CH/CBb CAIs reflect episodic cosmic ray fluxes caused by FUori-type outbursts. On the other hand, relatively low and variable $^{10}Be/^{9}Be$ ratios recorded in CV CAIs may reflect less episodic accretion events, possibly the EXori-type outbursts, which are confined to the evolution stage a few million years after the formation of the proto-solar disk (= class II). Note that CH and CH/CB CAIs show no (or very low) signs of ^{26}Al-derived excess ^{26}Mg, while most of CV CAIs show clear evidence of ^{26}Al-derived excess ^{26}Mg with canonical ratios. Therefore, if the above argument is correct, the injection of ^{26}Al in the solar system should occur between the evolutionary stages class I and class II of the proto-Solar disk. This scenario is in agreement with the arguments by other authors that the ^{26}Al-free CAIs

formed prior to injection and homogenization of ^{26}Al in the early solar system (Sahijpal and Goswami, 1998; Sahijpal et al., 2000; Krot et al., 2008a; see more discussion in Krot et al., 2012a).

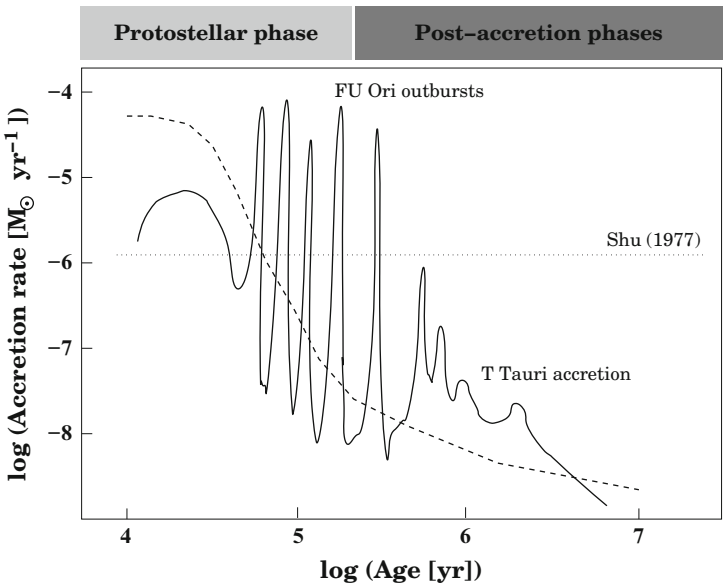

Fig. 3.38. The schematic diagram of the time development of the accretion rates as they appear in various calculations and in relation to astronomical observed phenomena. The dotted straight line resembles the results from standard star formation (Shu, 1977). The hatched curve represents an approximation to the results of the many more realistic calculation (see detailed in Schulz, 2012). The thick line was adapted from Hartmann (1998) and shows additional features such as outbursts of FU Ori type protostars and T Tauri disk accretion (≒ EXors). After Schulz (2012).

In 2006, the *Stardust* spacecraft returned to Earth a precious cargo of comet particles collected during a close fly-by of the Jupiter Family Comet 81P/Wild 2. The examination of the returned particles revealed that Wild 2 contains abundant high-

temperature silicate and oxide minerals, including CAI-like materials (Joswiak et al., 2014 and reference therein). The discovery is interpreted as: high-temperature inner solar system materials formed were subsequently transferred to the Kuiper Belt, and was incorporated into comets (Nakamura et al., 2008; Matzel et al., 2010). Matzel et al. (2010) measured the ^{26}Al-^{26}Mg isotope systematics of the Wild 2 refractory particle, coki, and revealed no evidence of radiogenic ^{26}Mg. As described in the introduction, CH and CH/CBb chondrites show isotopic similarities to cometary materials, which infer that CH and CH/CBb chondrites were accreted at the outer solar system (Van Kooten et al., 2016). In this study, CAIs in CH and CH/CBb chondrites do not show excesses in ^{26}Mg, which is similar to that of the Wild 2 particle coki. The similarity in ^{26}Al-^{26}Mg systematics between CAIs in CH and CH/CBb chondrites and the refractory particle of the Wild2 comet also suggests that accretion regions of CH and CH/CBb chondrites are strongly related to those of comets. If this is the case, large ^{10}B excesses in CH and CH/CBb CAIs observed in this study are direct evidence for the existence of material transportation processes from the inner solar system to cometary forming regions (Nakamura et al., 2008; Matzel et al., 2010). A direct test of this scenario would be to measure the ^{10}Be-^{10}B and ^{26}Al-^{26}Mg isotope systematics of comet refractory particles. My prediction is that the initial ^{10}Be/^{9}Be ratios of ^{26}Al-poor refractory particles in comets would show be higher and more variable than those of ^{26}Al-rich CV CAIs.

Note that, however, CAI Y20-9-1 from Y81020 (CO3.05) chondrite shows a relatively high ^{10}Be/^{9}Be ratio (2.0×10^{-3}) and a nearly canonical ^{26}Al/^{27}Al ratio ($(5.0 \pm 0.8) \times 10^{-5}$). This may suggest the timing of the ^{26}Al injection to the solar system occurred by the formation time of the CAI Y20-9-1, possibly the last stage of FUori outburst events. Alternatively, this may suggest different formation conditions for the CAI Y20-9-1 and CV CAIs. As described in 3.4.3, Sossi et al. (2017) investigated V isotopic compositions and Be-B systematics on CV CAIs. They also measured REE concentrations of these CAIs and mentioned that CAIs with high ^{10}Be/^{9}Be ratios have group II REE patterns. In

this study, CAI Y20-9-1 and Y20-1X1 also show relatively high $^{10}Be/^{9}Be$ ratios (2.0×10^{-3} and 3.0×10^{-3}, respectively) and group II REE patterns. These results suggest that controlling factors of the variation in $^{10}Be/^{9}Be$ ratios are not only the activity of early sun but also CAI formation history (e.g., differences of precursor materials). Future combined studies of REE concentrations and ^{10}Be-^{26}Al systematics of CAIs shed light on origins of the variation in $^{10}Be/^{9}Be$ ratios of CAIs.

3.5. Summary

I have performed Li-Be-B and Al-Mg analyses of CAIs in four carbonaceous chondrites (Yamato 81020 (CO), Yamato 82094I (ungrouped C), SaU290 (CH), and Isheyevo (CH/CBb)) with a NanoSIMS 50. Also, I have conducted REE measurements of the CAIs in the above CO and ungrouped C chondrites.

Most of CAIs in CO, ungrouped C, CH, and CH/CBb chondrites show higher and more variable initial $^{10}Be/^{9}Be$ ratios than those of CV CAIs. These results can be interpreted as evidence that ^{10}Be was produced by solar cosmic ray irradiation. CH and CH/CBb CAIs show no excesses in ^{26}Mg, suggesting early formation of CH and CH/CBb CAIs before the injection of ^{26}Al in the solar system. Lithium isotopic compositions of CAIs are identical to the chondritic composition independent of $^{10}Be/^{9}Be$ ratios, suggesting that ^{10}Be was produced by irradiation of materials having a chondritic Be/O ratio, possibly the solar gas.

The variable $^{10}Be/^{9}Be$ ratios observed in CAIs may reflect the variable cosmic ray fluxes from early active Sun at the different stage of the protosolar disk evolution. If this is correct, the injection time of ^{26}Al into the solar system corresponds to the stage between the class I and class II.

CHAPTER 4: Li-Be-B isotopic compositions of ungrouped C chondrules

In this chapter I report the Li-Be-B isotopic compositions of chondrules in ungrouped C chondrite. I found, for the first time, correlations between excesses ^{10}B and $^{9}Be/^{11}B$ ratios in chondrules, which imply a presence of live ^{10}Be at the time of the chondrule formation. The inferred initial $^{10}Be/^{9}Be$ ratio of the two Y82094 chondrules is on average $(1.92 \pm 0.45) \times 10^{-3}$ (2σ), which is higher than the average value of CV CAIs, but compatible with those of CO (Y81020) and CO-like (Y82094) CAIs. The observation suggests that: (1) ^{10}Be in these chondrules was produced by solar cosmic ray irradiation, (2) chondrules or precursor materials of chondrules should be irradiated by solar cosmic rays near the proto-Sun and transported to the chondrule formation region, and (3) the chondrule formation started very early before significant decay of ^{10}Be (e.g., within <1 Myr of CAI formation), possibly contemporaneously with formation of CAIs.

4.1. Introduction

Chondrules are typically submillimeter-sized spherules that have undergone significant melting, which provide important constraints on the earliest transient heating events that melted solids in the protoplanetary disk (e.g., Rubin, 2000). In unmetamorphosed chondrites, chondrules and refractory inclusions generally have uniform, but different oxygen isotopic compositions (e.g., Kita et al., 2016; Ushikubo et al., 2017). These differences suggest that chondrules and refractory inclusions originated in the isotopically and probably spatially distinct disk regions, ^{16}O-poor planetary-like and ^{16}O-rich solar-like, respectively. In the chapter 3, I concluded that CAIs formed in a disk region that was exposed to irradiation by solar cosmic rays and had high ambient temperature (> 1300 K), i.e., most likely near the proto-Sun. In contrast, chondrules are thought to have formed in relatively cold (< 1000 K) regions in the proto-solar disk (e.g., Alexander and Ebel, 2012). Thus, chondrules may have different chronological and/or spatial information of the protosolar disk evolution.

Here, I measured Li-Be-B isotopic compositions of two chondrules in an ungrouped C3.2 chondrite (Y82094). As mentioned above, chondrules may have information about the protosolar disk evolution different from that of CAIs, which would give information about the distribution of the ^{10}Be in wider regions of the protosolar disk. Hence, the determination of ^{10}Be abundances in chondrules offers a different viewpoint for the origin of ^{10}Be in the early solar system. Searching for ^{10}Be in chondrules has been attempted (e.g., Sugiura, 2001), but chondrules with high enough Be/B to resolve ^{10}B excesses appear to be extremely rare. Sugiura (2001) analyzed anorthite in chondrules from the Y82094 (ungrouped C3.2) chondrite and found a possible correlation between ^{10}B excesses and Be/B ratios, the latter of which was as high as 10. However, due to relatively large errors, the result was not conclusive. Furthermore, it should be noted that Sugiura (2001) have used geological standard samples of basaltic, andesitic, and granitic

compositions for determinations of $^{9}Be/^{11}B$ ratios of anorthite. In principle, accurate $^{9}Be/^{11}B$ measurements require a matrix-matched standard with a known chemical composition (i.e., $^{10}Be/^{9}Be$ atomic ratio). Hence, the result by Sugiura (2001) may have systematic errors in the $^{9}Be/^{11}B$ ratios of anorthite in chondrules. In addition, Sugiura (2001) conducted these Be-B measurements using a conventional small-geometry ion probe (CAMECA ims-6f) with a large primary ion beam (~30 × 30 μm^2), and therefore, some contamination effects derived from terrestrial and/or matrix boron cannot be ruled out.

To overcome these problems, firstly, I synthesized anorthitic glass standards doped with Be and B using the same method for synthesizing melilitic glass standards (described in chapter 2) and examined the possible RSF differences between anorthite and a silica-rich reference standard material (NIST SRM 610). Secondly, a high-spatial-resolution SIMS (CAMECA NanoSIMS 50) was used for determinations of $^{10}B/^{11}B$ and $^{9}Be/^{11}B$ ratios of chondrules. So far, I have succeeded to obtain Be-B systematics for two chondrules in the Y82094 chondrite. These chondrules are typical porphyritic olivine-pyroxene chondrules but have relatively large areas of mesostasis suitable for Be-B analysis (see below in 4.2.2). I have also tried to measure Be-B isotopes for some chondrules in one of the most primitive chondrites Y81020 (CO3.05), but it was not successful due to small sizes of anorthite and mesostasis in the chondrules. According to the newly obtained data of chondrules, I discuss possible origins of the ^{10}Be in the early solar system and its implication for the chondrule formation mechanisms.

4.2. Sample and methods

4.2.1. Production of Be- and B-bearing anorthite glasses and determination of RSFs

I synthesized four glasses with approximately anorthite compositions doped with trace amounts of Be and B with varying Be/B ratios (see Table 4.4). The preparation method is the same as that for melilitic glasses as described in chapter 2. The synthesized glasses (~1,000 × 1,000 μm^2) were embedded in epoxy together with a NIST SRM 610 glass standard and then polished. The sample mount was cleaned with Mill-Q water and ethanol to remove surface contamination. The sample was coated with carbon after drying to prevent surface charge during subsequent electron microprobe and SIMS analyses.

The major element concentrations of the synthetic glasses were determined with a JEOL JXA-8530F Field Emission Electron Probe Micro Analyzer (FE-EPMA) at the University of Tokyo using a 15 kV accelerating voltage, 12 nA beam current, ~1 μm focused beam, and wavelength-dispersive X-ray spectroscopy (WDS). Matrix effects were corrected using the ZAF method.

The ion intensities of Be and B were determined with a NanoSIMS 50 ion probe at the Atmosphere and Ocean Research Institute (AORI) of the University of Tokyo. Analytical conditions are the same as those for melilitic glasses (see chapter 2).

After the NanoSIMS analyses, Be and B concentrations of the synthetic glasses were determined using a LA-ICP-MS. Laser ablation was performed with an in-house laser ablation system (Cyber Probe) combined with a titanium–sapphire (Ti:S) femtosecond laser (IFRIT, Cyber Laser, Japan) and galvano metric fast scanning laser system (Yokoyama et al., 2011). A single quadrupole mass spectrometer (iCAP Qc, Thermo Fisher Scientific, USA) was utilized. Analytical conditions are the same as those for melilitic glasses (see chapter 2).

4.2.2. Y82094 (ungrouped C3.2) chondrules

I studied two type I porphyritic olivine-pyroxene (POP) chondrules in the Y82094 (ungrouped C3.2) carbonaceous chondrite. The mineralogy and major elemental abundances of the CAIs were investigated using the FE-EPMA. EPMA analyses were conducted at 15 KeV with a beam current of 12 nA, and 1 μm focused beam. Elemental abundances were obtained by using a ZAF correction.

Rare earth element (REE) abundances of the chondrules were investigated using the Thermo Fisher Scientific iCAP Qc ICP-MS coupled with a CETAC LSX-213 G2+ Nd:YAG LA system at the Department of Earth and Planetary Science, The University of Tokyo. The operating conditions of the instruments are the same as the measurements for CAIs (see section 3.2).

As described in chapter 3, Y82094 is the ungrouped C3.2 chondrite (Kimura et al., 2014). The meteorite is different from other carbonaceous chondrites in terms of the size of chondrules (Imae and Kojima, 2000; Kimura et al., 2014). Furthermore, Y82094 chondrules contain mesostasis regions larger than those in chondrules in other meteorites. Therefore, it was selected for the present Be-B study.

Chondrules Y94-42C2 and Y94-42C14 consist of Mg-rich olivine (Fo_{98-99}) crystals embedded in fine-grained mesostasis or poikilitically enclosed in large euhedral low-Ca pyroxene (En_{98}) phenocrysts. Poikilitic olivine grains, seated in low-Ca pyroxenes, being anhedral and on average smaller than olivine grains located in chondrule center (see Mg map in Fig. 4.2 and Fig, 4.4), suggest that they suffered dissolution processes prior to pyroxene crystallization (Libourel et al., 2006). These chondrules also contain minor amounts of high-Ca pyroxene ($En_{56}Wo_{43}$), Fe-Ni metal. High-Ca pyroxene is present in mesostasis phase often as phenocrysts (see Fig. 4.1b). Ca-rich pyroxenes contain 6.7-9.2 wt % Al_2O_3, and 1.0-1.2 wt % TiO_2. The mesostasis shows a fine-grained texture (see Fig. 4.1b and c), which cannot be individually measured.

Mesostases in these chondrules have nearly flat REE patterns showing a weak enrichment from HREE to LREE (Fig. 4.5). High-Ca pyroxene shows HREE enrichments and negative europium anomalies and a flattening for the HREE. The negative europium anomalies may indicate that a part of Eu existed as the divalent state (e.g., Jones and Layne, 1997; Jacquet et al., 2012) and was preferentially incorporated in the mesostasis. Major and REE element concentrations are shown in Tables 4.1 and 4.2, respectively. BEIs of Y94-42C2 and Y94-42C14 are shown in Figs. 4.1 and 4.3, respectively. X-ray elemental maps of Y94-42C2 and Y94-42C14 are shown in Figs. 4.2 and 4.4, respectively.

Tabel 4.1. Major element concentrations of chondrules in the Y82094 (ungrouped C3.2) chondrite

Inclusion	Y94-42C2				Y94-42C14		
Mineral	olv	mesostasis	Lpx	Hpx	olv	mesostasis	Hpx
Na_2O	0.07	2.42	0.01	0.00	0.00	2.32	0.02
MgO	56.23	6.42	39.12	18.41	56.62	6.59	17.46
SiO_2	42.12	54.61	59.72	51.50	42.62	54.41	49.81
Al_2O_3	0.51	21.41	0.68	7.36	0.03	22.19	7.04
FeO	0.40	0.60	0.92	0.43	0.86	0.58	0.84
MnO	0.11	0.18	0.02	0.17	0.21	0.22	0.16
K_2O	0.00	0.00	0.01	0.00	0.01	0.01	0.02
CaO	0.44	13.49	0.49	20.52	0.25	13.53	21.73
TiO_2	0.15	0.38	0.14	1.06	0.03	0.27	1.11
V_2O_3	0.05	0.00	0.03	0.05	n.m.**	n.m.**	0.00
Cr_2O_3	0.17	0.46	0.46	1.06	0.26	0.49	0.90
NiO	0.00	0.02	0.00	0.00	0.01	0.03	0.04
Total	100.25	100.00	101.60	100.55	100.91	100.64	99.12
No. of analyses	1	5	1	1	1	10	1
Fo# (or En#)	99		98	55	99		52

** Not measured

Tabel 4.2. Rare earth element concentrations of the Y94-42C7 CAI in the Y82094 (ungrouped C3.2) chondrite

Inclusion	Y94-42C2				Y94-42C14			
Mineral	mesostasis_1		mesostasis_2		mesostasis		Hpx	
	ppm	1SD	ppm	1SD	ppm	1SD	ppm	1SD
La	3.23 ±	0.55	3.38 ±	0.65	3.59 ±	0.74	1.62 ±	0.93
Ce	8.49 ±	1.97	9.20 ±	1.65	9.74 ±	1.61	4.91 ±	2.52
Pr	1.22 ±	0.29	1.24 ±	0.33	1.32 ±	0.30	0.82 ±	0.34
Nd	5.43 ±	1.79	5.89 ±	1.34	6.40 ±	1.63	4.60 ±	1.48
Sm	1.79 ±	1.45	1.81 ±	0.78	2.10 ±	0.81	1.94 ±	0.49
Eu	0.91 ±	0.37	0.88 ±	0.25	0.74 ±	0.35	0.32 ±	0.24
Gd	1.62 ±	0.99	1.84 ±	0.68	2.31 ±	0.88	2.87 ±	0.75
Tb	0.38 ±	0.27	0.32 ±	0.08	0.37 ±	0.15	0.55 ±	0.14
Dy	2.28 ±	0.89	2.68 ±	0.82	2.90 ±	0.77	3.82 ±	0.62
Ho	0.49 ±	0.23	0.52 ±	0.12	0.60 ±	0.25	0.84 ±	0.18
Er	1.39 ±	0.55	1.48 ±	0.52	1.74 ±	0.67	2.58 ±	0.58
Tm	0.31 ±	0.20	0.25 ±	0.10	0.25 ±	0.11	0.39 ±	0.11
Yb	1.97 ±	1.76	1.99 ±	0.99	2.12 ±	0.90	2.53 ±	0.50
Lu	0.23 ±	0.11	0.22 ±	0.11	0.27 ±	0.12	0.36 ±	0.09

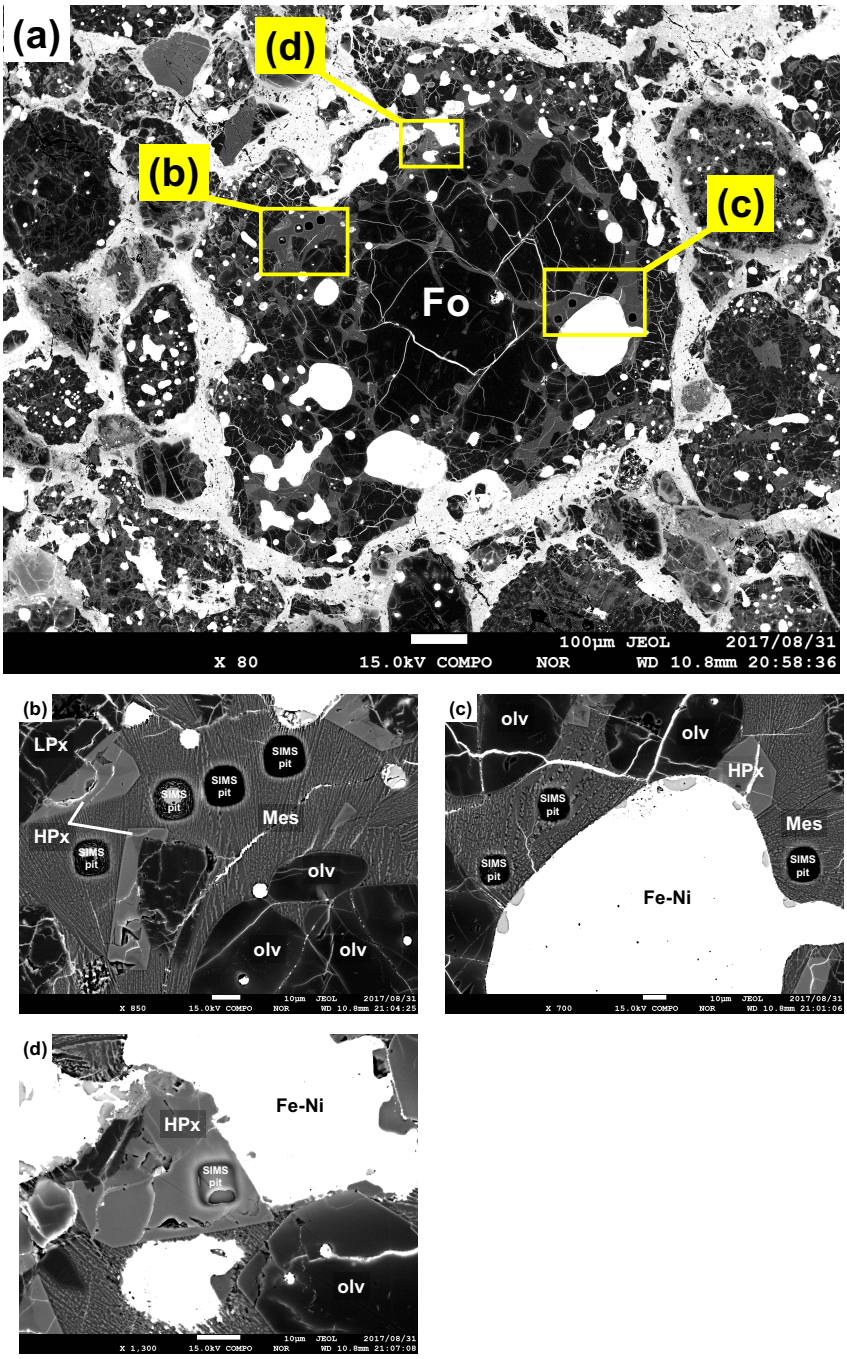

Fig. 4.1. BEIs of the chondrule Y94-42C2 in the Y82094 (ungrouped C3.2) chondrite. It consists of forsteritic olivine, low-Ca pyroxene, high-Ca pyroxene, Fe-Ni metal, and mesostasis. Regions outlined in (a) are shown in detail in (b-d). (b and c) fine-grained mesostasis and phenocrysts of high-Ca pyroxene. (d) high-Ca pyroxene in mesostasis. The Be-B isotopic composition was measured for this pyroxene.

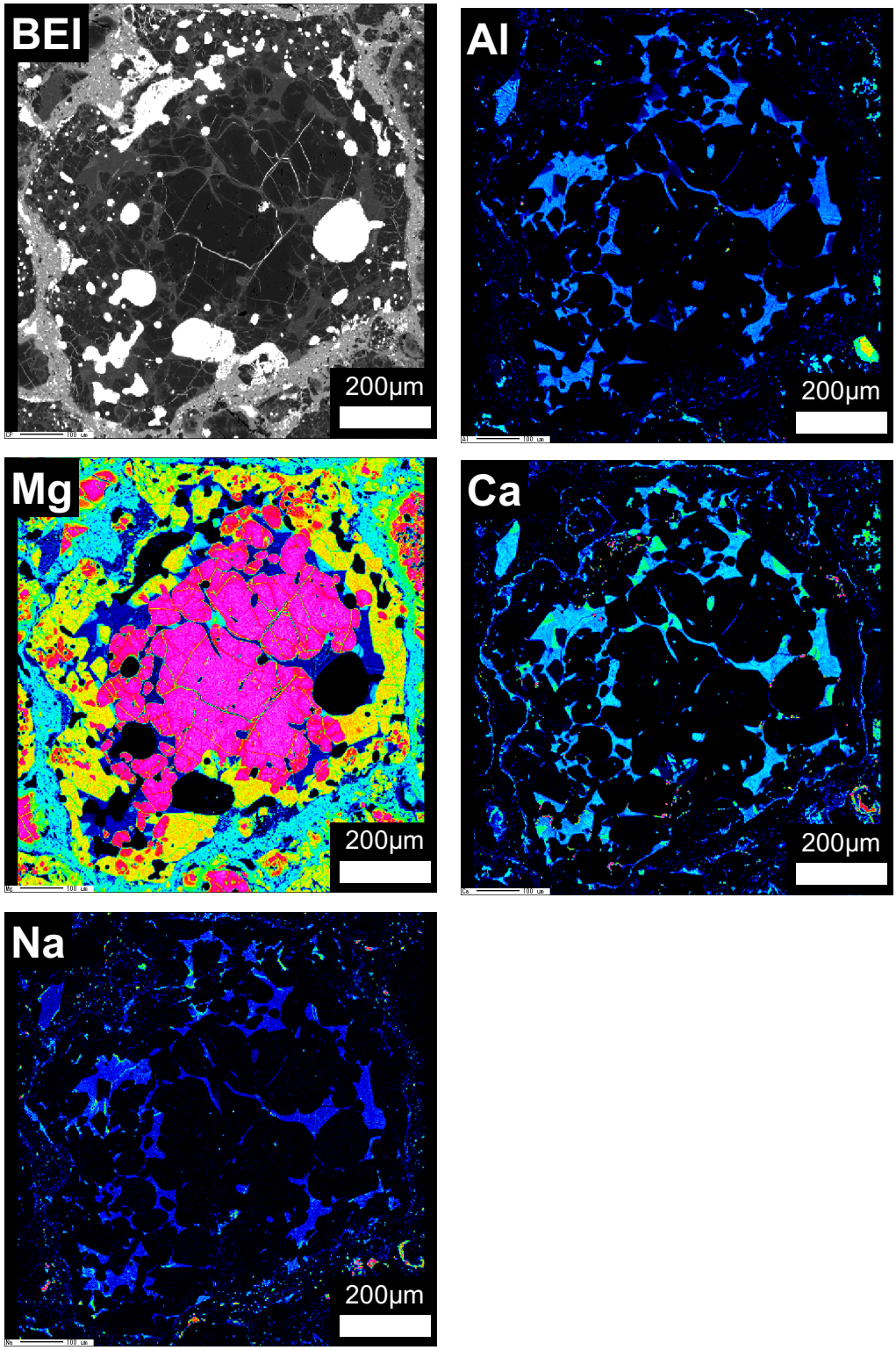

Fig. 4.2. A BEI and X-ray elemental maps in Mg, Ca, Al, Ti, and Na of the chondrule Y94-42C2 in the Y82094 (ungrouped C3.2) chondrite.

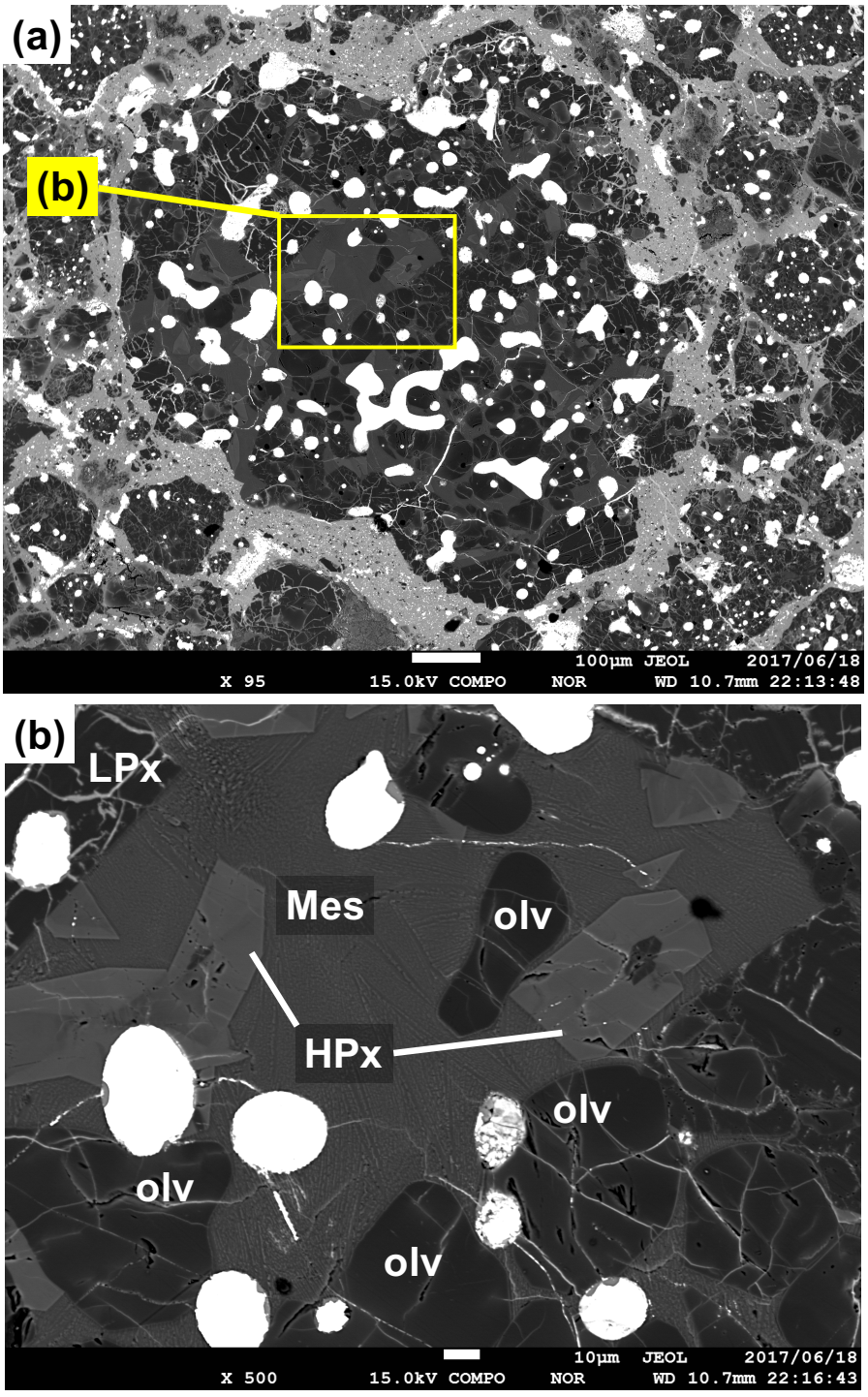

Fig. 4.3. BEIs of the chondrule Y94-42C14 in the Y82094 (ungrouped C3.2) chondrite. It consists of forsteritic olivine, low-Ca pyroxene, high-Ca pyroxene, Fe-Ni metal, and mesostasis. The region outlined in (a) is shown in detail in (b).

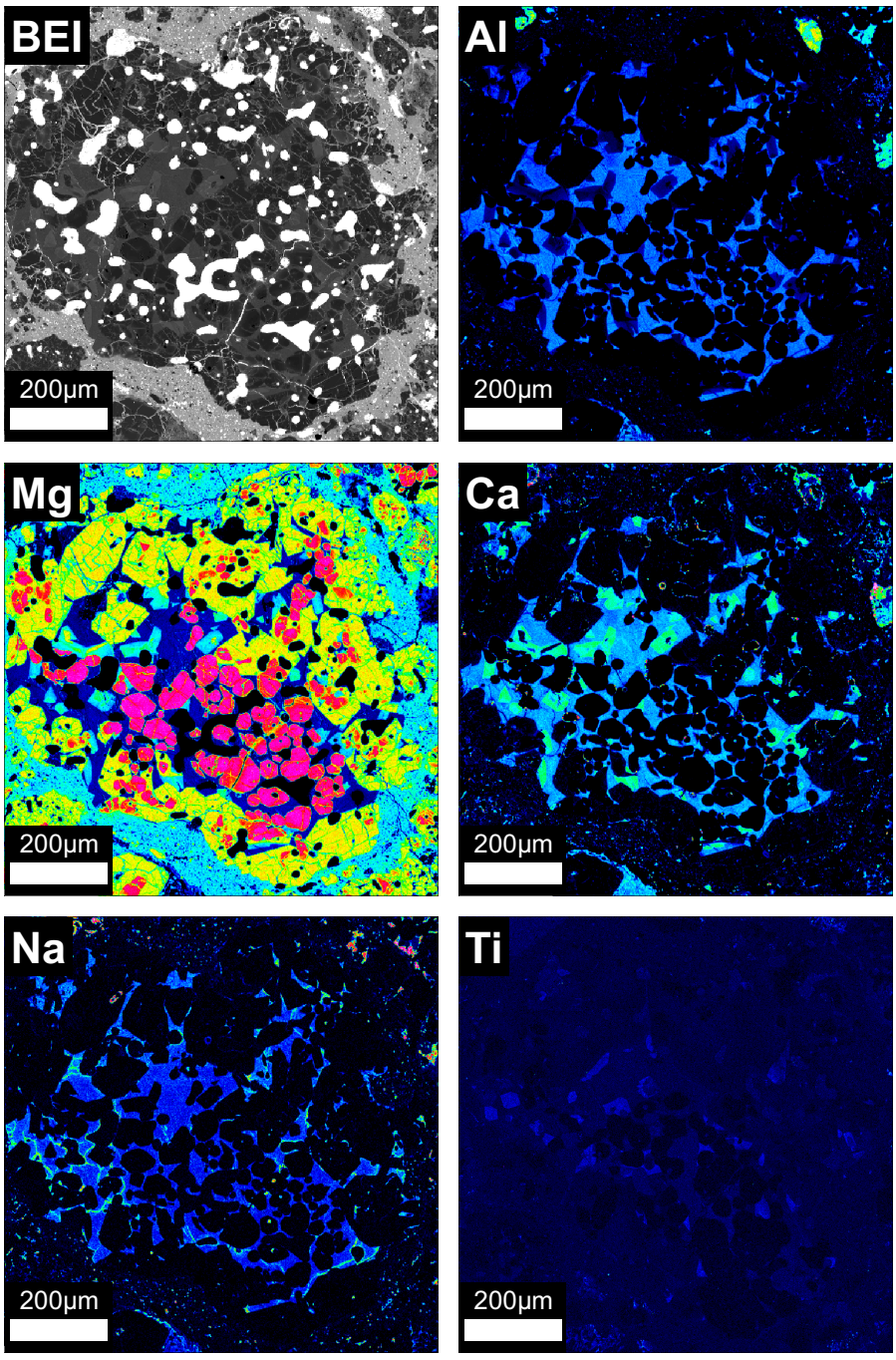

Fig. 4.4. A BEI and X-ray elemental maps in Mg, Ca, Al, Ti, and Na of the chondrule Y94-42C14 in the Y82094 (ungrouped C3.2) chondrite. Poikilitic olivine grains seated in low-Ca pyroxenes, being anhedral and on average smaller than olivine grains located in chondrule center (see Mg map), suggest they suffered dissolution processes prior to pyroxene crystallization (Libourel et al., 2006).

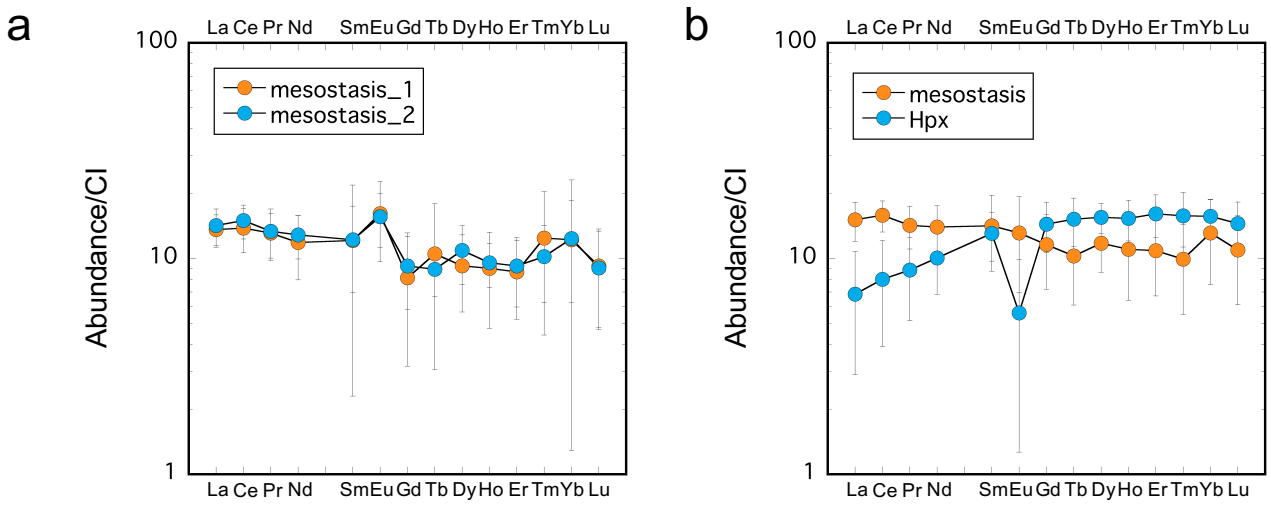

Fig. 4.5. CI-normalized abundances of REEs in chondrules Y94-42C2 (a) and Y94-42C14 (b) in the Y82094 (ungrouped C3.2) chondrite.

4.2.3. Measurement conditions of Li-Be-B isotope analyses

The Be-B isotope measurements of the Y82094 chondrules were performed using a NanoSIMS 50 installed at the AORI, the University of Tokyo. The NanoSIMS measurements were performed in multi-collection mode. An $^{16}O^-$ primary ion beam, ~5 nA intensity and ~10 μm in diameter, was rastered over 10 x 10 μm^2 areas (32 × 32 pixel with a dwell time of 200 μs/pixel). Prior to the measurements, a primary ion beam of ~5 nA was rastered over 15 × 15 μm^2 on the samples to remove surface contamination and to obtain secondary ion images of the samples, which helped to choose measurement spots. Then secondary ions of $^9Be^+$, $^{10}B^+$, $^{11}B^+$, and $^{30}Si^+$ were detected simultaneously with secondary electron multipliers (EMs). Measurements were performed with a mass resolving power (MPR) of 1500 at 1% peak height. Typical intensities of $^9Be^+$ and $^{10}B^+$of the samples were ~70 cps, and ~4 cps, respectively. An electronic beam blanking mode was applied so that only signals from the central 24 × 24 pixel area were collected. This blanking helped to avoid contributions from scattered ions from the surroundings. A dead

time (~44 ns) of the counting system was also corrected. The background of EMs (ranging from 0.01 to 0.05 cps) were checked for each analytical spot after each measurement and corrected for each measurement. The instrumental mass fractionation effects were also corrected using NIST 610 standard ($^{10}B/^{11}B$ = 0.2469: Kasemann et al. 2001).

After the Be-B isotope measurements, Li isotope measurements were performed using the same secondary ion optics of the Be-B isotope measurements. An $^{16}O^-$ primary ion beam, ~1 nA intensity and ~5 μm in diameter, was rastered over 10 x 10 μm^2 areas (32 × 32 pixel with a dwell time of 200 μs/pixel). Prior to the measurements, a primary ion beam of ~1 nA was rastered over 10 × 10 μm^2 on the samples to remove surface contamination. Secondary ions of $^6Li^+$, $^7Li^+$, and $^{30}Si^+$ were detected simultaneously with EMs. Intensities of $^6Li^+$ and $^{30}Si^+$ of the samples were ~50 cps and 1.4 × 10^5 cps, respectively. The background ranged from 0.007 to 0.03 cps. The instrumental mass fractionation effects were corrected using the NIST 612 glass ($^7Li/^6Li$ = 12.553; Kasemann et al., 2005). The Li concentrations of olivine and pyroxene in chondrules were estimated by comparison with the NIST 612 glass ([Li] = 40.2 ppm; Jochum et al., 2011).

4.3. Results

4.3.1. Synthetic anorthitic glasses

The concentrations of major elements in the anorthitic glasses are listed in Table 4.3. The Be and B concentrations in these glasses obtained from LA-ICP-MS analyses are also listed in Table 4.3.

The $^{9}Be/^{11}B$ atomic ratios (calculated from the Be and B concentrations in Table 4.3), $^{9}Be^{+}/^{11}B^{+}$ ion intensity ratios measured with the NanoSIMS, and corresponding Be/B RSFs calculated for individual glasses are listed in Table 4.4. Figure 4.6a shows the $^{9}Be^{+}/^{11}B^{+}$ intensity ratios as a function of atomic $^{9}Be/^{11}B$ ratios. The $^{9}Be^{+}/^{11}B^{+}$ intensity ratios and atomic $^{9}Be/^{11}B$ ratios of the synthesized glasses show a fair correlation. Relatively large errors in the elemental ratios (Be/B and B/Si, Figs. 4.6a and 4.6c) for some samples may suggest some heterogeneities in the glasses (see discussion in 4.4.1). The average value of Be/B RSF is 2.77 ± 0.93 (2σ). I also determined the Bee/B RSF for NIST SRM 610 under the same analytical conditions and obtained the RSF is 2.56 ± 0.11 (2 SD). The present results demonstrate that the Bee/B RSF of the synthetic anorthitic glasses is identical to that of NIST SRM 610, within uncertainties.

I also determined the RSFs of $^{9}Be/^{30}Si$ and $^{11}B/^{30}Si$ for anorthitic glasses and NIST 610. The Bee/Si and B/Si RSFs obtained for anorthitic glasses are slightly higher than or almost comparable to those of the NIST 610 glass (see Fig. 4.6b and 4.6c). The $^{9}Be/^{30}Si$ and $^{11}B/^{30}Si$ atomic ratios (calculated from the Be, B, and SiO_2 concentrations in Table 4.3), $^{9}Be^{+}/^{30}Si^{+}$ and $^{11}B^{+}/^{30}Si^{+}$ ion intensity ratios measured with the NanoSIMS, and corresponding Be/Si and B/Si RSFs calculated for individual glasses are listed in Table 4.5 and 4.6, respectively.

Table 4.3. Major element compositions, and Be and B concentrations in synthetic anorthitic glasses and NIST 610 glass

Sample	MgO	2SD	Al_2O_3	2SD	SiO_2	2SD	CaO	2SD	Na_2O	total	No. of analyses
					wt %						
AG1-2	0.28	± 0.04	42.53	± 6.56	37.66	± 6.26	19.38	± 0.82	-	99.84	20
AG1-5	0.11	± 0.04	43.04	± 1.82	36.84	± 1.57	19.20	± 0.72	-	99.18	20
AG1-7	1.07	± 0.11	42.23	± 2.17	37.48	± 2.15	19.09	± 0.93	-	99.87	20
AG1-9	0.11	± 0.04	42.53	± 1.24	37.24	± 1.08	19.50	± 1.08	-	99.38	20
NIST 610 [*1]	0.0057		1.98		69.4		11.59		13.6		

Sample	Be (ppm)	2SD	B (ppm)	2SD	No. of analyses
AG1-2	1318.1	± 207.7	46.2	± 17.3	7
AG1-5	2174.1	± 44.8	28.5	± 2.2	7
AG1-7	201.7	± 6.0	47.5	± 12.3	6
AG1-9	2166.7	± 97.9	24.7	± 7.8	5
NIST 610 [*1]	476		350		

[*1] Major elements, Be, and B concentrations from Jochum et al. (2011).

Table 4.4. Be/B atomic and ion intensity ratios, and the calculated relative sensitivity factors

Sample	$^{9}Be/^{11}B$ atomic ratios (atomic ratio) [*2]	No. of Analyses	$^{9}Be^{+}/^{11}B^{+}$ (ion intensity ratio) [*3]	No. of Analyses	RSF [*1]
AG1-2	44.0 ± 12	7	9.0 ± 9.0	3	2.27 ± 0.67
AG1-5	114.0 ± 8	7	345.0 ± 15.3	2	3.02 ± 0.26
AG1-7	6.0 ± 1	6	21.1 ± 1.0	3	2.50 ± 0.79
AG1-9	134.0 ± 42	5	335.2 ± 17.9	3	3.29 ± 0.77
Average					***2.77 ± 0.93***
NIST 610	2.03		5.0 ± 0.2	9	2.56 ± 0.11

[*1] relative sensitivity factor: $(^{9}Be^{+}/^{11}B^{+})_{NanoSIMS}$ $/(^{9}Be/^{11}B)_{atomic}$. Errors are 2 σ. [*2] calculated from Be and B concentrations in Table

[*2] calculated from Be and B concentrations in Table 1 assuming terrestrial isotopic ratios. Errors are 2 σ.

[*3] Errors are 2 Standard Deviation (2SD). If 2SD errors are smaller than the reproducibility of NIST 610 (2SD), the latter was adopted.

Table 4.5. Be/Si atomic and ion intensity ratios, and the calculated relative sensitivity factors

Sample	$^{9}Be/^{30}Si$ (atomic ratio) [*2]	$^{9}Be^{+}/^{30}Si^{+}$ (ion intensity ratio) [*3]	$^{9}Be/^{30}Si$ RSF [*1]
AG1-2	0.669 ± 0.148	0.427 ± 0.029	0.64 ± 0.15
AG1-5	1.091 ± 0.051	0.782 ± 0.053	0.72 ± 0.06
AG1-7	0.103 ± 0.006	0.066 ± 0.004	0.64 ± 0.06
AG1-9	1.100 ± 0.059	0.753 ± 0.051	0.68 ± 0.06
Average			***0.67 0.08***
NIST 610	0.148	0.085 ± 0.006	0.59 ± 0.04

Table 4.6. B/Si atomic and ion intensity ratios, and the calculated relative sensitivity factors

Sample	$^{11}B/^{30}Si$ (atomic ratio) [*2]	$^{11}B^{+}/^{30}Si^{+}$ (ion intensity ratio) [*3]	$^{11}B/^{30}Si$ RSF [*1]
AG1-2	0.0157 ± 0.0063	0.0091 ± 0.0008	0.58 ± 0.24
AG1-5	0.0095 ± 0.0008	0.0048 ± 0.0001	0.50 ± 0.05
AG1-7	0.0162 ± 0.0043	0.0066 ± 0.0005	0.41 ± 0.11
AG1-9	0.0084 ± 0.0027	0.0047 ± 0.0001	0.56 ± 0.18
Average			***0.51 0.16***
NIST 610	0.0727	0.0357 ± 0.0011	0.49 ± 0.01

[*1] relative sensitivity factor: $(^{9}Be^{+}$ (or $^{11}B^{+})/^{30}Si^{+})_{NanoSIMS}/(^{9}Be$ (or $^{11}B)/^{30}Si)_{atomic}$. Errors are 2 σ.
Note that RSFs are not absolute values because relative sensitivities between the EMs used for Be and Si (B and Si) were not checked.

[*2] calculated from SiO_2, Be, and B concentrations in Table 1 assuming terrestrial isotopic ratios. Errors are 2 σ.

[*3] Errors are 2 Standard Deviation (2SD).

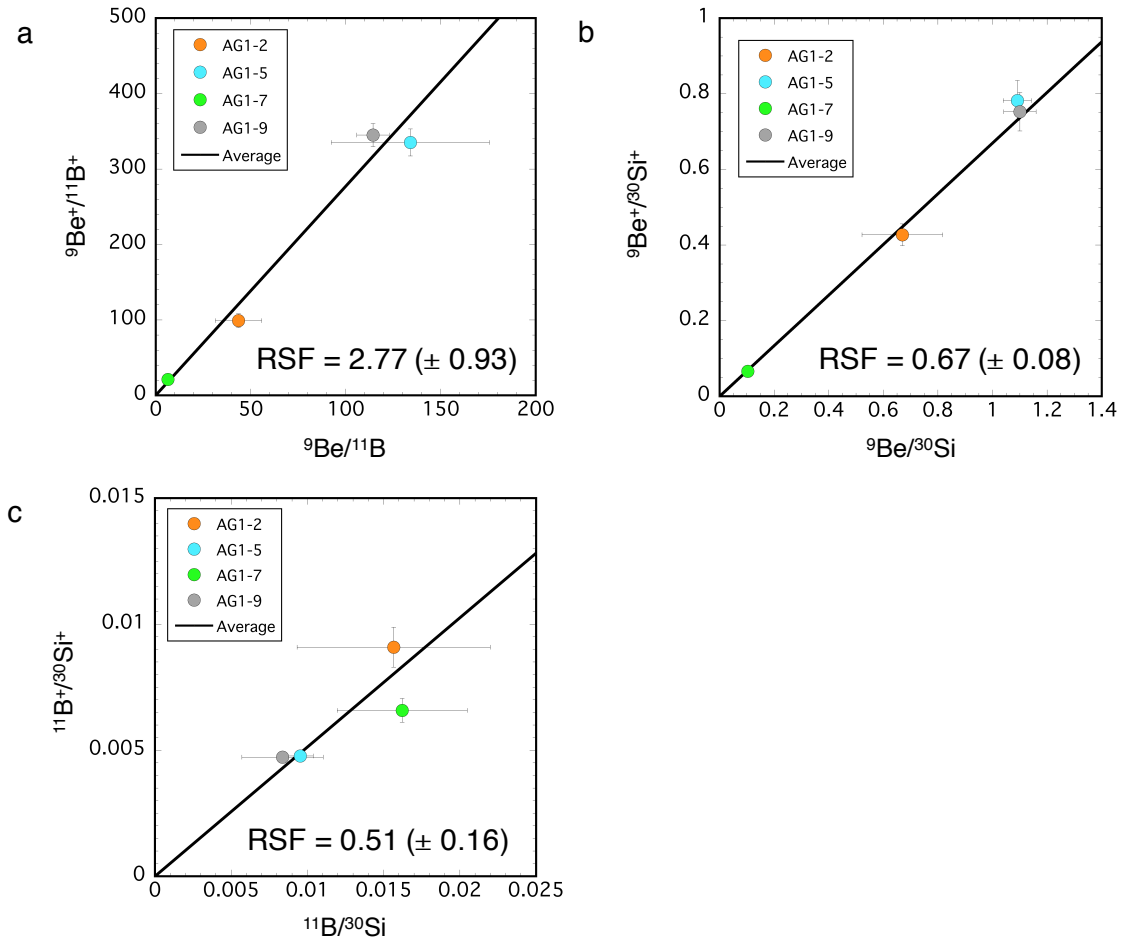

Fig. 4.6. Ion intensity ratios as a function of atomic ratios determined on four synthetic anorthitic glasses. The error bars represent 2 standard deviations (SD) evaluated from repeated measurements of individual glasses (see discussion 4.4.1 for relatively large errors of some data points). The slopes of the lines show the simple mean values of the calculated relative sensitivity factors of four glasses. (a) $^{9}Be^{+}/^{11}B^{+}$ ratios as a function of Be/B atomic ratios. The sensitivity difference between the electron multipliers (EMs) for $^{9}Be^{+}$ and $^{11}B^{+}$ was corrected. (b) $^{9}Be^{+}/^{30}Si^{+}$ ratios as a function of Be/Si atomic ratios determined for four synthetic anorthitic glasses. (c) $^{11}B^{+}/^{30}Si^{+}$ ratios as a function of B/Si atomic ratios determined for four synthetic anorthitic glasses. Note that RSFs of (b) and (c) are not absolute values because sensitivity differences between EMs for $^{9}Be^{+}$ (or $^{11}B^{+}$) and $^{30}Si^{+}$ were not corrected.

4.3.2. Y82094 (ungrouped C3.2) chondrules

I studied the Be-B systems of two chondrules (Y94-42C2 and Y94-42C14) in the Y82094 chondrite. In addition, I also measured Li isotopic compositions of the Y94-42C2 chondrule. The results of the isotope analyses are presented in Tables 4.7 and 4.8.

Sugiura (2001) conducted only one Be-B measurement for each chondrule. In this study, taking advantage of the high spatial resolution of the NanoSIMS, I performed replicate analyses for different spots on single chondrules with a total of 9 measurements for Y94-42C2, and 7 measurements for Y94-42C14. Mesostases in the Y94-42C2 show ^{10}B excesses up to ~ 95 ‰ which correlate weakly with the $^{9}Be/^{11}B$, indicating the in-situ decay of ^{10}Be (Fig. 4.7a). On the other hand, high-Ca pyroxene do not show an excess in ^{10}B with $^{9}Be/^{11}B = 0.03$. The initial $^{10}Be/^{9}Be$ ratio, $(^{10}Be/^{9}Be)_0$, was determined from the slope of an isochron. The $(^{10}Be/^{9}Be)_0$ value was determined to be $(2.6 \pm 2.4) \times 10^{-3}$ for Y94-42C2 (error is 2σ). The initial $^{10}B/^{11}B$ ratio, determined from the intercept of the isochron, was found to be 0.245 ± 0.015 (error is 2σ). Mesostases in the Y94-42C14 also show ^{10}B excesses up to ~ 120‰, but do not show a fair correlation with $^{9}Be/^{11}B$ within limited ranges in $^{9}Be/^{11}B$ (Fig. 4.7b). The initial $^{10}Be/^{9}Be$ ratio and the initial $^{10}B/^{11}B$ ratio were determined to be $(1.1 \pm 3.8) \times 10^{-3}$ and 0.253 ± 0.029, respectively, for Y94-42C2 (errors are 2σ). Figure 4.7c shows an isochron diagram for combined data of Y94-42C2 and Y94-42C14. The bulk isochron for the two chondrules yields $(^{10}Be/^{9}Be)_0 = (1.6 \pm 1.5) \times 10^{-3}$ with an intercept $(^{10}B/^{11}B) = 0.250 \pm 0.011$.

$^{7}Li/^{6}Li$ ratios of olivine and mesostasis in Y94-42C2 are 12.30 ± 0.17 and 12.35 ± 0.26, respectively and these values are similar to the chondritic $^{7}Li/^{6}Li$ ratio ($^{7}Li/^{6}Li$ = 12.06: Seitz et al. 2007).

Table. 4.7 Be-B isotope data of the chondrules in the Y82094 chondrites

Sample name	Analysis spots	mineral	Be (ppb)	B (ppb)	$^{9}Be/^{11}B$	error (2σ)	$^{10}B/^{11}B$	error (2σ)
Y94-42C2	42C2an_1	mesostasis	334	57	9.0	0.2	0.269	0.018
	42C2an_2	mesostasis	408	112	5.5	0.1	0.253	0.020
	42C2_1	mesostasis	-*	-*	6.2	0.3	0.261	0.011
	42C2_2	mesostasis	-*	-*	7.9	0.4	0.267	0.016
	42C2_3	mesostasis	-*	-*	6.2	0.3	0.271	0.017
	42C2_4	mesostasis	388	53	-**	-**	-**	-**
	42C2_5	Hpx	4	204	0.0	0.0	0.246	0.017
	42C2_6	mesostasis	-*	-*	6.8	0.3	0.260	0.013
	42C2_7	mesostasis	-*	-*	5.6	0.3	0.259	0.009
Y94-42C14	42C14an_1	mesostasis	385	66	8.8	0.1	0.269	0.018
	42C14an_2	mesostasis	402	67	8.0	0.2	0.260	0.017
	42C14_1	mesostasis	-*	-*	9.0	0.4	0.260	0.014
	42C14_2	mesostasis	-*	-*	7.9	0.4	0.277	0.012
	42C14_5	mesostasis	435	72	9.2	0.4	0.258	0.013
	42C14_6	mesostasis	-*	-*	9.4	0.4	0.260	0.011
	42C14_9	mesostasis	-*	-*	4.6	0.2	0.256	0.008

-* ^{30}Si is not measured

-** In order to determine Be and B concentrations, only Be/Si and B/Si raitos were measured using low current beam.

Table. 4.8 Li isotope data of the Y94-42C in the Y82094 chondrite

Sample name	Analysis spots	mineral	Li (ppb)	$^{7}Li/^{6}Li$	error (2σ)
Y94-42C2	42C2_1	olivine	876	12.30	0.17
	42C2_2	mesostasis	262	12.35	0.26

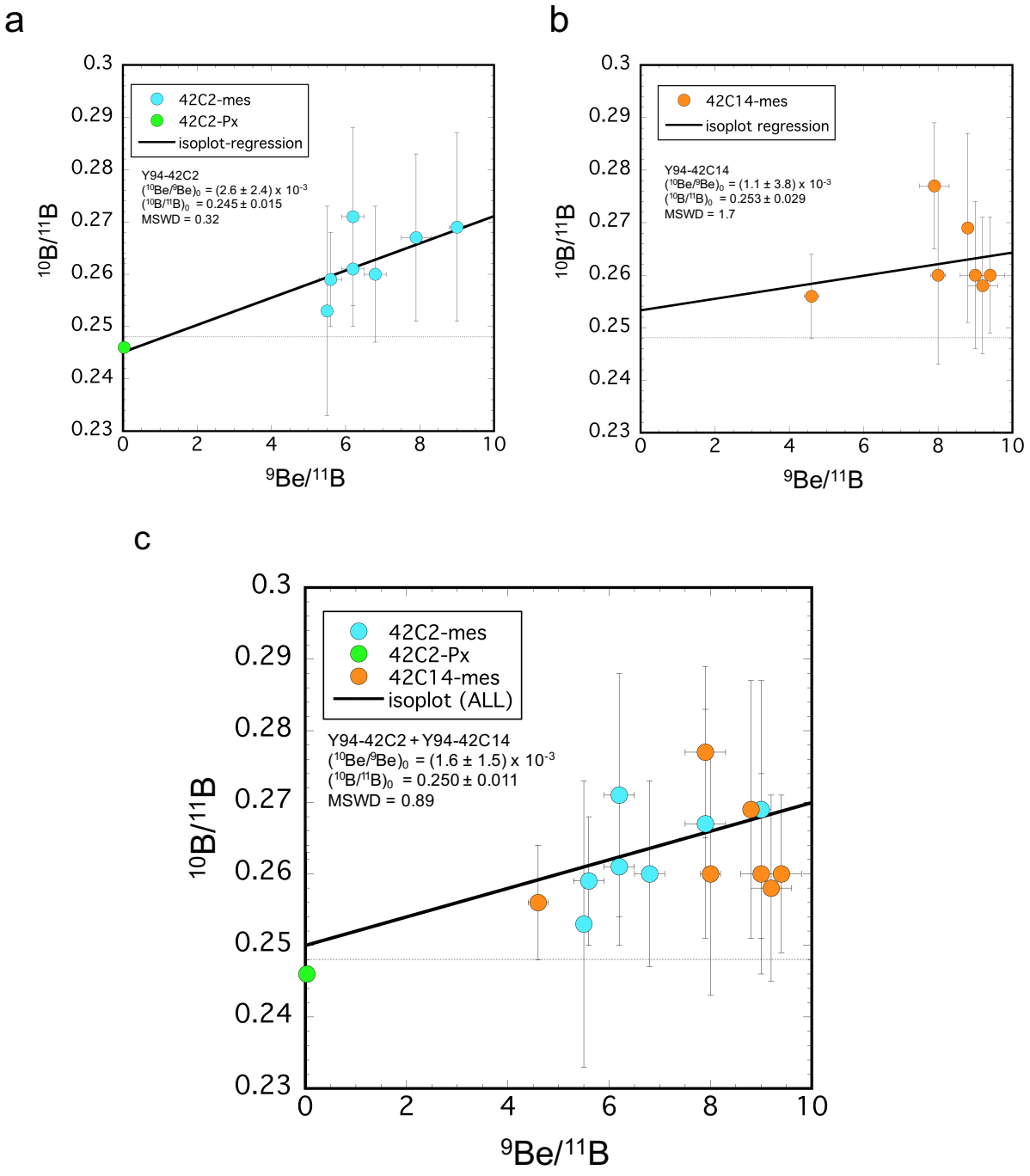

Fig. 4.7. Be-B isochron diagrams for chondrules in the Y82094 chondrite: (a) chondrule Y94-42C2 and (b) chondrule Y94-42C14. (c) A combined plot of (a) and (b). Error bars (± 2σ) on both $^{10}B/^{11}B$ and $^{9}Be/^{11}B$ include both an external reproducibility and an internal precision.

4.4. Discussion

4.4.1. Comparison of RSFs between anorthitic glasses and silica-rich glasses

Here I show the similarity in Be/B RSFs between synthetic anorthitic glasses (2.77 ± 0.93: 2 SD) and NIST 610 glass (2.56 ± 0.11: 2 SD), which implies that matrix effects do not significantly affect the relative ionization efficiencies of Be and B. The conclusion agrees well with the case for synthetic melilitic glasses (see chapter 2).

It should be noted, however, that the RSF for anorthitic glasses show a large error (~34%: 2 SD), which is significantly larger than that for melilitic glasses (~11%: 2 SD). This might have resulted from a heterogeneous incorporation of B (and Be) in anorthitic glasses. In fact, B/Si ratios determined by LA-ICP-MS show large errors (see Fig. 4.6c). Moreover, EPMA observations also suggest that anorthitic glasses are more heterogeneous than melilitic glasses (see Table 4.3). In fact, the anorthite glass AG1-2, which shows the most heterogeneous composition (see Table 4.3), includes numerous ~ μm sized inclusions, but such inclusions were not found in melilite glasses (see Figs. 4.8b and 4.8c). It should also be noted that the analyzed phases of chondrules in this study are not anorthite, but mesostases. However, mesostases in the two chondrules have Al-, Si-, and Ca-rich compositions (see Table.4.1), which are similar to those of anorthitic glasses synthesized in this study. Furthermore, chemical compositions of anorthite are broadly consistent with those of melilite glasses (i.e., Al-, Si-, and Ca-rich). Since the present results demonstrate that there are no significant differences in RSFs between

anorthitic, melilitic, and NIST 610 glass standards. I decided to use the RSF of NIST 610 (2.56 ± 0.11: 2 SD) to obtain the $^{9}Be/^{11}B$ ratios for chondrules.

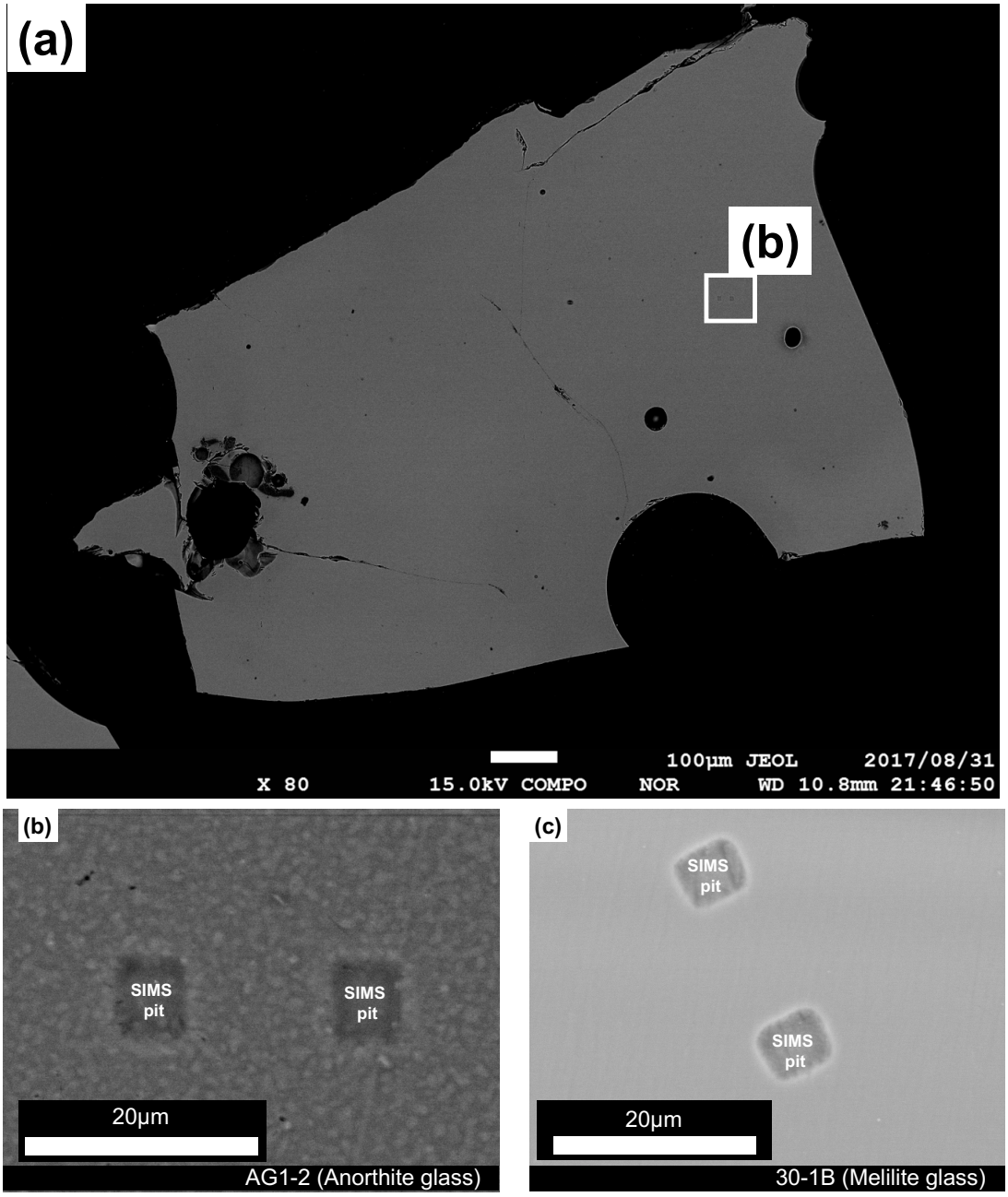

Fig. 4.8. BEIs of an anorthitic glass (a-b) and an melilitic glass (c). (a) The anorthitic glass AG1-2. A region outlined in (a) is shown in detail in (b). (c) A high magnification BEI of the melilitic glass 30-1B for comparison.

4.4.2. Li-Be-B systematics on chondrules in the Y 82094 (ungrouped C) chondrite and its implications for the origin of ^{10}Be in the early solar system

Resolved excesses in ^{10}B were observed in two chondrules with ^{9}Be/^{11}B of ~ 4 to 10. Here, I discuss possible origins of excesses in ^{10}B in chondrules and its implications for the origin of ^{10}Be in the early solar system.

In the previous study, in most cases where chondrules have low Be/B ratios (<< 1), one can study the intrinsic ^{10}B/^{11}B variations in chondrules. Chaussidon and Robert (1995, 1998) demonstrated that chondrules from various chondritic meteorites exhibit a large heterogeneity in δ^{11}B, ranging from -40‰ to +40‰. Moreover, the variations were found to be positively correlated with B/Si ratios. They interpreted the observation to show the presence of ^{11}B-rich grains that were produced by spallation reactions of low energy cosmic rays with hydrogen in the protosolar molecular cloud. In their model, boron in chondrules represents a mixture of galactic cosmic ray (high energy) spallation boron (^{11}B/^{10}B = 2.5) and low energy spallation boron (^{11}B/^{10}B = 3.5-11; e.g., Ramaty et al., 1996) and isotopic heterogeneities resulted from the mixing of these two components in variable proportions. Thus, the observed excesses in ^{10}B in this study could also be attributed to the mixing between low and high B isotopic components. However, two lines of evidence argue against this mechanism. First, a similar study of chondrules by Hoppe et al. (2001) demonstrated results in clear contrast to those in Chaussidon and Robert (1995, 1998). Hoppe et al. (2001) measured boron isotopic compositions in sixteen chondrules with porphyritic, barred, and radial types, and host meteorite include carbonaceous, ordinary, and enstatite chondrites. They found no significant variation in δ^{10}B outside their experimental errors of a few permil, and their boron isotopic compositions agree with those reported for bulk chondrites. They also stressed that δ^{10}B of chondrules are independent of the boron abundances in chondrules despite as much as

2 orders of magnitude lower than those analyzed by Chaussidon and Robert (1995, 1998). Therefore, it is unclear whether or not the ^{11}B-rich grains existed in the early solar system. Furthermore, I observed only positive δ^{10}B but not negative δ^{10}B, which is different from the observation of both positive and negative variations reported in Chaussidon and Robert (1995, 1998). Considering the positive δ^{10}B with high ^{9}Be/^{11}B, the excesses in ^{10}B observed in this study were attributed to the decay of ^{10}Be.

In this study, I measured B isotopic compositions of mesostases and one high-Ca pyroxene in chondrules. The former show excesses in ^{10}B (δ^{10}B ~120‰) with relatively high ^{9}Be/^{11}B ratios (> 4), but the latter shows no excess in ^{10}B (δ^{10}B = -6‰) with a low ^{9}Be/^{11}B ratio (= 0.03). The boron isotopic compositions of bulk chondrites (Zhai et al., 1996) and chondrules with low ^{9}Be/^{11}B ratios (Hoppe et al., 2001; high-Ca pyroxene data obtained in this study) suggest that there are no indications for large intrinsic heterogeneities in B isotopic compositions in the solar system. Thus, I may assume that the initial B isotopic compositions of chondrules is also nearly chondritic value (^{10}B/^{11}B = 0.2481). If this is the case, I can define model isochrons for Y82094 chondrules and obtain model initial ^{10}Be/^{9}Be ratios. The inferred model initial ^{10}Be/^{9}Be ratios of Y94-42C2 and Y94-42C14 are $(2.17 \pm 0.74) \times 10^{-3}$ and (1.76 ± 0.57), respectively (errors are 2σ), which are slightly higher than those of CAIs in CV chondrites ($< 1.2 \times 10^{-3}$; see chapter 1 and 3).

The ^{10}Be/^{9}Be ratios recorded in Y82094 chondrules provide important implications for the evolution of the protosolar disk. First, the distribution of ^{10}Be in the early solar system is not only restricted to formation regions and/or formation time of CAIs, but also those of chondrules. Considering that chondrules are the dominant component of most chondrites (up to ~80% by volume; Scott and Krot 2014), ^{10}Be would be distributed more extensively in the protosolar disk than previously thought. Additionally, as discussed previously in chapter 3, the high and variable ^{10}Be/^{9}Be ratios ($\sim 4 \times 10^{-3}$) recorded in CO, CH, and CH/CBb CAIs strongly suggest that ^{10}Be was

produced by solar cosmic ray irradiation near the proto-Sun. In the case of Y82094 chondrules, the inferred model initial $^{10}Be/^{9}Be$ ratios (1.76×10^{-3} and 2.17×10^{-3}) are also higher than those predicted by a molecular cloud origin ($\sim 0.3 \times 10^{-3}$: Desch et al., 2004; Tatischeff et al., 2014) and by a neutrino spallation processes origin with core-collapse supernovae ($\sim 0.8 \times 10^{-3}$: Banerjee et al., 2016). Thus, the present results also support the solar cosmic ray irradiation model for the origin of ^{10}Be (e.g., McKeegan et al., 2000). If ^{10}Be was produced by solar cosmic ray irradiation, not only ^{10}Be but also $^{6,7}Li$ and $^{10,11}B$ are produced by the processes. Thus, Li and B isotopic compositions would be affected by solar cosmic ray irradiation. The spallation effects for Li and B isotopic compositions are highly depend on chemical compositions of irradiation targets. I estimated the irradiation effects on $^{7}Li/^{6}Li$ and $^{10}B/^{11}B$ for the Y94-42C2 chondrule under the same irradiation conditions in section 3.4.3. Considering Be/Li and Be/B ratios of mesostases in this chondrule (Be/Li ~1.1, Be/B ~3.9, respectively), the expected $^{7}Li/^{6}Li$ and $^{10}B/^{11}B$ ratios with $^{10}Be/^{9}Be = 2.17 \times 10^{-3}$ are ~6.8 and ~0.35, respectively. The calculated ratios are significantly different from the observed $^{7}Li/^{6}Li$ and initial $^{10}B/^{11}B$ ratios (12.3 ± 0.17 and 0.245 ± 0.025, respectively) in this chondrule. The inconsistency between calculated ratios and the observed ratios can be solved by the following scenarios. First, proton was irradiated to the solar nebular gas and chondrule precursors were condensed from the irradiated solar gas. In this case, Li and B isotopic modification by proton irradiation are less effective. For example, if the solar composition gas (Be/Li ~ 0.012 and Be/B ~ 0.034) was irradiated and ^{10}Be was produced at a level of $^{10}Be/^{9}Be = 2.17 \times 10^{-3}$, the expected $^{7}Li/^{6}Li$ and $^{10}B/^{11}B$ ratios are ~ 12 and ~0.250, respectively. The calculated results are consistent with the observed isotopic $^{7}Li/^{6}Li$ and initial $^{10}B/^{11}B$ ratios in this study. Therefore, the present results suggest that ^{10}Be was not produced by irradiation of chondrule solids, but by irradiation of their precursors possibly a solar nebula gas. Second, the spallogenic signatures have been erased by the chondrule forming event(s). In fact, the preferential distribution of pyroxene at chondrule margins (see Mg maps in Fig. 4.2

and 4.4) can be interpreted as interaction of chondrule melt with a SiO-rich gas during chondrule formation (Libourel et al., 2006; Souli et al., 2017). Therefore, chondrule precursors might have experienced isotopic modification by the gas-melt interaction. If this is the case, the spallogenic Li and B isotopic compositions of irradiated precursor material should be diluted by reacted SiO-rich gas. Although I cannot completely exclude this scenario, it should be noted that at least some precursor materials should contain live ^{10}Be at the time of chondrule formation.

4.4.3. Implications for the chondrule formation process

Although analytical errors are large, the resolved excesses in ^{10}B, significant at the 2σ level, can be considered as evidence for the presence of live ^{10}Be at the time of chondrule formation. Here, based on the finding, I discuss the possible scenario for the chondrule formation.

Recent high precision isotopic analyses revealed that chondrules in various types of chondrites have distinct isotopic signatures in some elements, such as O, Mg, Ti, and Cr (Kita et al., 2016; Van Kooten et al., 2016; Olsen et al., 2016; Gerber et al., 2017), indicating that each chondrite group sampled materials in a specific region of the protosolar disk. For example, oxygen isotopic compositions of chondrules are generally ^{16}O-depleted (~5%) relative to CAIs (e.g., Scott and Krot, 2014), indicating that chondrules formed from different regions where CAIs originated. Additionally, chondrule sizes and chemical compositions also suggest that chondrules in various types of chondrites formed at distinct regions in the protosolar disk (e.g., Jones et al., 2012). These characteristics suggest that chondrules have not formed in the CAI forming region (possibly near the proto-Sun) but various regions in the protosolar disk. Thus, it is unlikely that proton was irradiated to the Y82094 chondrule themselves near the proto-

Sun. Here I propose that ^{10}Be in chondrules was inherited from irradiated precursor materials. If this is the case, the irradiated materials were transported from near the proto-Sun to each chondrule forming region and were processed for the chondrule formation. As described above, the inferred model initial ^{10}Be/^{9}Be ratios are $(2.17 \pm 0.74) \times 10^{-3}$ and (1.76 ± 0.57), which are slightly higher than those of CAIs in CV chondrites ($< 1.2 \times 10^{-3}$), indicating that if the precursor materials have experienced solar cosmic ray irradiation under similar conditions of CAIs, the irradiated precursor materials should be processed for the chondrule formation very early before the significant decay of ^{10}Be. The rapid formation scenario for chondrules is consistent with U-corrected Pb-Pb absolute ages of chondrules, which demonstrated that chondrule formation started contemporaneously with CV CAIs at 4567.3 ± 0.16 Ma (Connelly et al., 2012; Bollard et al., 2017).

Note, however, that the initial ^{10}Be/^{9}Be ratio of chondrules discussed here is inferred from model isochron (see section 4.4.2). The internal ^{10}Be/^{9}Be ratios of Y94-42C2 and 42C14 are $(2.6 \pm 2.4) \times 10^{-3}$ and $(1.1 \pm 3.8) \times 10^{-3}$, respectively, which include significant errors. Thus, it is not possible to accurately compare the value with the initial ^{10}Be/^{9}Be ratios of CAIs. Further high precision Be-B measurements of various types of chondrules are required to provide more robust constraints on the chondrule formation history in the protosolar disk.

4.5. Summary

I synthesized Be- and B-bearing anorthitic glasses and investigated the Be/B RSFs of these glasses using a NanoSIMS 50 and a LA-ICP-MS. Although some heterogeneity may exist in boron concentrations in synthesized glasses, I found that the Be/B RSFs of anorthitic glasses are identical to that for NIST 610 silica-rich glass within uncertainties. As mentioned in chapter 2, the present results also demonstrated that matrix does not significantly affect the relative ionization efficiencies of Be and B.

Also, I have performed the Li-Be-B analyses of the two chondrules in the Y82094 (ungrouped C3.2) chondrite with the NanoSIMS 50. The mesostases in the Y82094 chondrules show excesses in ^{10}B with $^{9}Be/^{11}B$ of ~4 to 10, indicating the presence of live ^{10}Be at the time of the chondrule formation. The inferred model initial $^{10}Be/^{9}Be$ ratios are $(2.17 \pm 0.74) \times 10^{-3}$ and $(1.76 \pm 0.57) \times 10^{-3}$, which are higher than those of CAIs in CV chondrites ($< 1.2 \times 10^{-3}$). This result can be interpreted as further evidence that ^{10}Be was produced by solar cosmic ray irradiation. Initial $^{10}B/^{11}B$ ratio and Li isotopic ratios of the chondrules are similar to the chondritic compositions, suggesting that ^{10}Be was produced by irradiation of a solar nebular gas (i.e., precursor materials of chondrules). These conclusions are broadly consistent with those from pristine CAIs in CO and CH chondrites. The high $^{10}Be/^{9}Be$ ratio observed in chondrules indicates that Y82094 chondrules might have formed very early before significant decay of ^{10}Be, nearly contemporaneous formation of CAIs.

CHAPTER 5: Concluding remarks

During my Ph.D. course, I studied the origin of ^{10}Be and irradiation processes in the early solar system on the basis of Li-Be-B and Al-Mg isotopic compositions of CAIs and chondrules in carbonaceous chondrites.

I investigated the 'matrix effect' for the determination of Be/B ratios of melilite and anorthite. I showed that the relative sensitivity factors of Be and B for melilite (and anorthite with relatively large uncertainties at present) in SIMS are comparable to that of NIST SRM 610 silica-rich glass, which has been often used in previous studies as a standard. The present results confirm that the observed variations in ^{10}Be/^{9}Be ratios for CAIs in CV chondrites are real and that the origin of ^{10}Be is most likely attributed to irradiation by early active Sun. It is also inferred that the ^{10}Be/^{9}Be ratios of *F*ractionation and *U*nidentified *N*uclear effect (FUN) CV CAIs are not significantly lower than those for normal (non-FUN) CV CAIs, suggesting their similar formation conditions.

I performed Li-Be-B and Al-Mg isotopic measurements on CAIs in Y81020 (CO3.05), Y82094 (ungrouped C3.2), SaU290 (CH3), and Isheyevo (CH/CBb) chondrites. I found that the inferred ^{10}Be/^{9}Be ratios range from ^{10}Be/^{9}Be = 1.7 x 10^{-4} to 40.5 × 10^{-4}, which are much higher and more variable than previously thought. These results strongly suggest that ^{10}Be was produced by solar cosmic ray irradiation. In addition, it is also found that Li isotopic compositions of these CAIs are nearly chondritic irrespective of their ^{10}Be/^{9}Be ratios. The present results can be explained if the targets of cosmic ray irradiation are the chondritic composition; in other words, targets are most likely not CAI themselves, but their precursors of solar gases.

Furthermore, in order to further investigate the distribution of ^{10}Be in the protosolar disk, I performed Li-Be-B isotopic measurements for chondrules in the Y82094 (ungrouped C3.2) chondrite. I found that excesses in ^{10}B, significant at the 2σ

level, are positively correlated with the $^{9}Be/^{11}B$ ratios in chondrules, which indicates the presence of live ^{10}Be at the time of the chondrule formation. Evidence for incorporation of ^{10}Be in chondrules is the first confirmation of a widespread distribution of ^{10}Be in the protosolar disk. The inferred initial $^{10}Be/^{9}Be$ ratio is $(1.92 \pm 0.45) \times 10^{-3}$ (2σ), which is higher than those of CAIs in CV chondrites ($< 1.2 \times 10^{-3}$). Such a high value can be interpreted as further evidence that ^{10}Be was produced by solar cosmic ray irradiation. The observed initial $^{10}B/^{11}B$ and $^{7}Li/^{6}Li$ ratios of the chondrules are similar to the chondritic compositions, suggesting that ^{10}Be was produced by irradiation of a solar nebular gas. These conclusions are broadly consistent with those from pristine CAIs in CO and CH chondrites. The high $^{10}Be/^{9}Be$ ratios observed in chondrules indicate that Y82094 chondrules might have formed very early, possibly contemporaneous to formation of CAIs.

These new findings were attained by high-spatial and high-accurate Be-B measurements on early solar system solids in various types of primitive meteorites. It was achieved by technical improvements including the production of synthetic Be- and B-doped glass standards and developments of the protocol of Li-Be-B isotopic measurements using the NanoSIMS 50.

As mentioned above, most of CAIs in CH and CH/CBb chondrites show higher and more variable initial $^{10}Be/^{9}Be$ ratios than those of CV CAIs. According to these observations, I propose that CH and CH/CB CAIs have formed at the episodic accretion stage in the evolution of the protosolar disk (= Class I). On the other hand, CV CAIs may represent the samples that have formed at less episodic accretion stage (= class II) (Fig. 5.1).

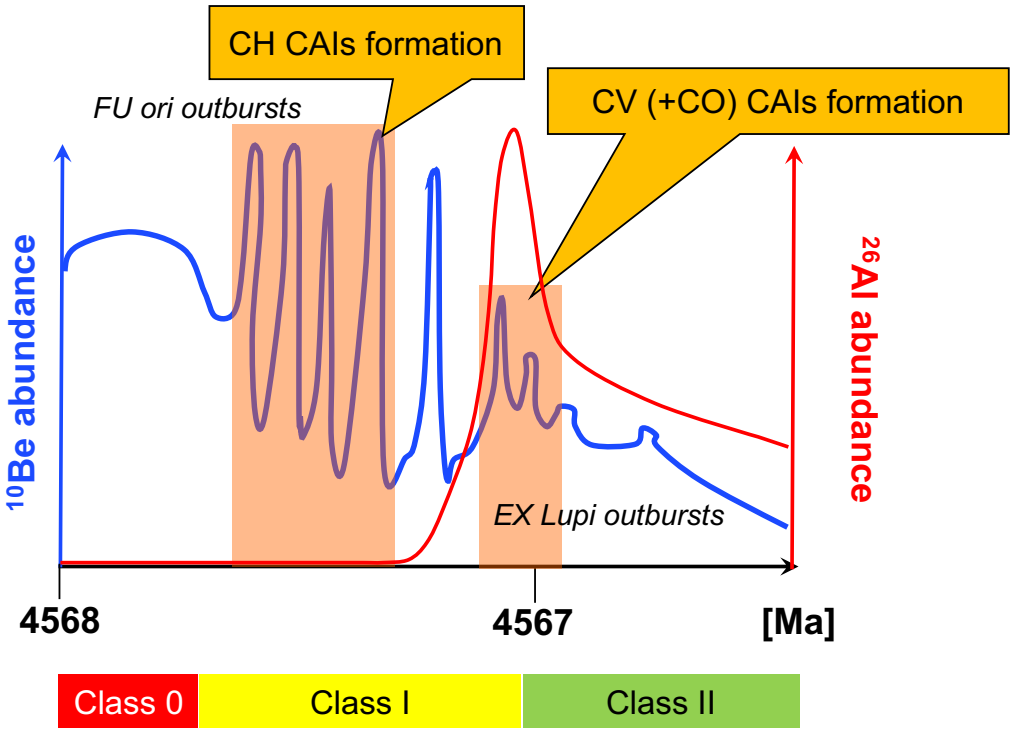

Fig. 5.1. The schematic diagram of the time development of the ^{10}Be and ^{26}Al abundances in the proto-solar disk. I assumed that ^{10}Be abundances correspond to the number flux of proton, which reflects variable accretion rates in association with the evolution of the protoplanetary disk. If the observed variations in ^{10}Be/^{9}Be correspond to the variation in the number flux of proton, CH CAIs have formed at the class I at the stage of the proto-solar disk evolution and CV (and CO) CAIs have formed at the later stage (class II). If this is correct, the injection and/or homogenization of ^{26}Al in the proto-solar disk should have occurred between the class I and class II at the evolution of the proto-solar disk. Modified after Schulz (2012).

REFERENCES

Aoyama, T., Tashiro, H. and Suzuki, K. (1999) Diffusion of boron, phosphorus, arsenic, and antimony in thermally grown silicon dioxide. *J. Electrochem. Soc.* **146**, 1879-1883.

Alexander, C. M. O'D. and Ebel, D. S. (2012) Questions, questions: Can the contradictions between the petrologic, isotopic, thermodynamic, and astrophysical constraints on chondrule formation be resolved? *Meteorit. Planet. Sci.* **47**, 1157-1175.

Andersen, C. A. and Hinthorne, J. R. (1973) Thermodynamic approach to the quantitative interpretation of sputtered ion mass spectra. Anal. Chem. **45**, 1421-1438.

Amelin, Y., Kaltenbach, A., Iizuka, T., Stirling, C. H., Ireland, T. R., Petaev, M. and Jacobsen, S. B. (2010) U-Pb chronology of the solar system's oldest solids with variable $^{238}U/^{235}U$. *Earth Planet. Sci. Lett.* **300**, 343-350.

Arnould, M., Goriely, S. and Meynet, G. (2006) The production of short-lived radionuclides by new non-rotating and rotating Wolf-Rayet model stars. *A&A*, **453**, 653-659.

Asphaug, E., Jutzi, M. and Movshovitz, N. (2011) Chondrule formation during planetesimal accretion. *Earth Planet. Sci. Lett.* **308**, 369-379.

Banerjee, P., Qian, Y.-Z., Heger, A. and Haxton, W. C. (2016) Evidence from stable isotopes and ^{10}Be for solar system formation triggered by a low-mass supernova. *Nat. Commun.* **7**, 13639.

Bischoff, A., Palme, H., Schultz, L., Weber, D., Weber, H. W. and Spettel, B. (1993) Acfer 182 and paired samples, an iron-rich carbonaceous chondrite: Similarities with ALH85085 and relationship to CR chondrites. *Geochim. Cosmochim. Acta* **57**, 2631-2648.

Blander, M., Pelton, A. D., Jung, I.-H., and Weber, R. (2004) Non-equilibrium concepts lead to a unified explanation of the formation of chondrules and chondrites. *Meteorit. Planet. Sci.* **39**:1897–1910.

Bollard, J., Connelly, J. N., Whitehouse, J., Pringle, E. A., Bonal, L., Jørgensen, J. K., Nordlund, Å., Moynier, F., and Bizzarro, M. (2017) Early formation of planetary building blocks inferred from Pb isotopic ages of chondrules. *Sci. Adv.* **3**, e1700407.

Bonal, L., Huss, G. R., Krot, A. N., Nagashima, K., Ishii, H. A., and Bradley J. P. (2010) Highly ^{15}N-enriched chondritic clasts in the CB/CH-like meteorite Isheyevo. *Geochim. Cosmochim. Acta* **74**, 6590-2609.

Boss, A. P. and Ciesla, F. J. (2014) The solar nebula. *In Meteorites and Cosmochemical Processes, Vol. 1: Treatise on Geochemistry 2nd edition*, Elsevier, Oxford, pp. 37-53.

Bouvier, A., Brennecka, G. A. and Wadhwa, M. (2011) Absolute Chronology of the First Solids in the Solar System. *Formation of the first solids in the solar system.* #1639.

Briani, G., Gounelle, M., Marrocchi, Y., Mostefaoui, S., Leroux, H. and Quirico, E. (2009) Pristine extraterrestrial material with unprecedented nitrogen isotopic variation. *Proc. Nat. Acad. Sci.* USA **106**, 10522-10527.

Burnett, D. S., Liu, M.-C., Paque, J. M., McKeegan, K. D. and Beckett, J. R. (2015) Testing solar proton irradiation models for ^{10}Be: correlation with ^{138}La (abstract). *Lunar Panet. Sci.* **46**. #1394.

Catanzaro, E. J., Murphy, T. J., Garner, E. L. and Shields, W. R. (1966) Absolute isotopic abundance ratios and atomic weight of magnesium. *J.Natl. Bur. Stand.* **70A**, 453.

Chaussidon, M. and Robert, F. (1995) Nucleosynthesis of ^{11}B-rich boron in the pre-solar cloud recorded in meteoritic chondrules. *Nature.* **374**, 337-339.

Chaussidon, M. and Robert, F. (1998) ^{7}Li/^{6}Li and ^{11}B/^{10}B variations in chondrules from the Semarkona unequilibrated chondrite. *Earth Planet. Sci. Lett.* **164**, 577-589.

Chaussidon, M., Robert, F. and McKeegan, K. D. (2006) Li and B isotopic variations in

an Allende CAI: Evidence for the in situ decay of short-lived ^{10}Be and for the possible presence of the short-lived nuclide ^{7}Be in the early solar system. *Geochim. Cosmochim. Acta* **70**, 224-245.

Chen, H.-W., Lee, T., Lee, D.-C. and Chen, J.-C. (2015) Correlation of ^{48}Ca, ^{50}Ti, and ^{138}La heterogeneity in the Allende refractory inclusions. *Astrophys. J.* **806**, L21 (4pp).

Connelly, J. N., Bizzarro, M., Krot, A. N., Nordlund, A., Wielandt, D. and Ivanova, M. A. (2012) The absolute chronology and thermal processing of solids in the solar protoplanetary disk. *Science* **338**, 651-655.

Davis, A. M. and McKeegan, K. D. (2014) Short-lived radionuclides and early solar system chronology. *In Meteorites and Cosmochemical Processes, Vol. 1: Treatise on Geochemistry 2nd edition*. Elsevier, Oxford, pp. 361–395.

Desch, S. J., Connolly, H. C., Jr. and Srinivasan, G. (2004) An interstellar origin for the beryllium 10 in calcium-rich, aluminum-rich inclusions. *Astrophys. J.* **602**, 528-542.

Desch, S. J., Ciesla, F. J., Hood, L. L. and Nakamoto, T. (2005) Heating of chondritic materials in solar nebula shocks. *Chondrites and the Protoplanetary Disk, ASP Conf. Ser.341,* pp. 849-872.

Desch, S. J., Kalyaan, A. and Alexander, C. M. O'D. (2017) The effect of Jupiter's Formation on the distribution of Refractory Elements and Inclusions in Meteorites. *arXiv:*1710.03809.

Dunham, E., Wadhwa, M., Simon, S. and Grossman, L. (2016) Beryllium-boron systematics of refractory inclusions in CR2 and CV3 chondrites: evidence for ^{10}Be heterogeneity (abstract). *Meteorit. Planet. Sci.* **79**. #6222.

Dunham, E., Wadhwa, M. and Desch, S. J. (2017) Beryllium-boron systematics of two distinctive CAIs from CV3 chondrites: the relatively pristine CAI B4 from NWA 6991 and the FUN CAI CMS-1 from Allende (abstract). *Lunar Panet. Sci.* **48**.

#1507.

Ebel, D. S. and Grossman, L. (2000) Condensation in dust-enriched systems. *Geochim. Cosmochim. Acta* **64**, 339-366.

Evans, N. J. II, Dunham, M. M., Jørgensen, J. K., Enoch, M. L., Merín, B., van Dishoeck, E. F., Alcalá, J. M., Myers, P. C., Stapelfeldt, K. R., Huard, T. L., Allen, L. E., Harvey, P. M., van Kempen, T., Blake, G. A., Koerner, D. W., Mundy, L. G., Padgett, D. L., and Sargent, A. I. (2009) The Spitzer c2d Legacy Results: Star Formation Rates and Efficiencies; Evolution and Lifetimes. *Astrophys. J.* **181**, 321-350.

Fahey, A. J., Goswami, J. N., McKeegan, K. D. and Zinner, E. (1987) ^{26}Al, ^{244}Pu, ^{50}Ti, REE, and trace element abundances in hibonite grains from CM and CV meteorites. *Geochim. Cosmochim. Acta* **51**, 329-350.

Feigelson, E. D. and Montmerle, T. (1999) High-energy processes in young stellar objects. *Annu. Rev. Astron. Astrophys.* **37**, 363-408

Feigelson, E. D., Garmire, P. and Pravdo, S. H. (2002a) Magnetic flaring in the pre-main-sequence Sun and implications for the early solar system. *Astrophys. J.* **572**, 335-349.

Feigelson, E. D., Broos, P., Gaffney III, J. A. and Garmire, G. (2002b) X-ray-emitting young stars in the orion nebula. *Astrophys. J.* **574**, 258-292.

Fowler, W. A., Greenstein, J. L., and Holyle, F. (1962) Nucleosynthesis during the early history of the solar system. *Geophys. J. R. Astron. Soc*., **6**, 148-220.

Fujiya, W., Sugiura, N., Hotta, H., Ichimura, K. and Sano, Y. (2012) Evidence for the late formation of hydrous asteroids from young meteoritic carbonates. *Nat. Commun.* **3**, 627.

Fukuda, K., Fujiya, W., Hiyagon, H., Makino, Y., Sugiura, N., Takahata, N., Hirata, T. and Sano, Y. (2018) Beryllium-boron relative sensitivity factors for melilitic glasses measured with a NanoSIMS ion microprobe. *Geochem. J.* **52**, (8pp).

Füri, E. and Marty, B. (2015) Nitrogen isotope variations in the Solar System. *Nat. Geosci,*

8, 515–522.

Gerber, S., Christoph, B., Budde, G., Metzler, K. and Kleine, T. (2017) Mixing and Transport of Dust in the Early Solar Nebula as Inferred from Titanium Isotope Variations among Chondrules. *Astrophys. J.* **841**, L17 (7pp).

Giletti, B. J. and Shanahan, T. M. (1997) Alkali diffusion in plagioclase feldspar. *Chem. Geol.* **139**, 3-20.

Gounelle, M., Shu, F. H., Shang, H., Glassgold, A. E., Rehm, K. E. and Lee, T. (2001) Extinct radioactivities and protosolar cosmic rays: Self-shielding and light elements. *Astrophys. J.* **548**, 1051-1070.

Gounelle, M., Shu, F. H., Shang, H., Glassgold, A. E., Rehm, K. E. and Lee, T. (2006) The irradiation origin of beryllium radioisotopes and other short-lived radionuclides. *Astrophys. J.* **640**, 1163-1170.

Gounelle, M., Chaussidon, M. and Rollion-Bard, C. (2013) Variable and extreme irradiation conditions in the early solar system inferred from the initial abundance of ^{10}Be in Isheyevo CAIs. *Astrophys. J.* **763**, L33 (5pp).

Greshake, A., Bischoff, A. and Putnis, A. (1998) Transmission electron microscope study of compact Type A calcium- aluminum-rich inclusions from CV3 chondrites: Clues to their origin. *Astrophys. J.* **33**, 75-87.

Grossman, L. (1975) Petrography and mineral chemistry of Ca-rich inclusions in the Allende meteorite. *Geochim. Cosmochim. Acta* **39**, 433-454.

Grossman, L., Ebel, D. S., Simon, S. B., Davis, A. M., Richter, F. M. and Parsad, M. (2000) Major element chemical and isotopic compositions of refractory inclusions in C3 chondrites: The separate roles of condensation and evaporation. *Geochim. Cosmochim. Acta* **64**, 2879-2894.

Grossman, L. and Brearley, A. J. (2005) The onset of metamorphism in ordinary and carbonaceous chondrites. *Meteorit. Planet. Sci.* **40**, 87-122.

Gurenko, A. A., Veksler, I. V., Meixner, A., Thomas, R., Dorfman, A. M. and Dingwell.

D. B. (2005) Matrix effect and partitioning of boron isotopes between immiscible Si-rich and B-rich liquids in the Si-Al-B-Ca-Na-O system: A SIMS study of glasses quenched from centrifuge experiments. *Chem. Geol.* **222**, 268-280.

Han, J. and Brearley, A. J. (2017) Microstructures and formation history of melilite-rich calcium–aluminum-rich inclusions from the ALHA77307 CO3.0 chondrite. *Geochim. Cosmochim. Acta* **201**, 136-154.

Hartmann, L. and Kenyon, S. (1996) The FU orionis phenomenon. *Astrophys. J.* **34**, 207-240.

Hartmann, L. (1998) Accretion processes in star formation. *Cambridge Astrophysics series,* **32**, Cambridge University Press.

Herbig, G. H. (1977) Eruptive phenomena in early stellar evolution. *Astrophys. J.* **217**, 629-715.

Herbig, G. H. (2007) EX LUPI: History and spectroscopy. *Astrophys. J.* **133**, 2679-2683.

Hidaka, H. and Yoneda, S. (2017) Isotopic evidence for intensive activity of young Sun from REE isotopic compositions in CAIs (abstract). *Goldschmidt conference,* **27**.

Hiyagon, H., Hashimoto, A., Kimura, M. and Ushikubo, T. (2003) First discovery of an ultra-refractory nodule in an Allende fine-grained inclusion (abstract). *Lunar Panet. Sci.* **34**. #1552.

Hiyagon, H., Yamakawa, A., Ushikubo, T., Lin, Y. and Kimura, M. (2011) Fractionation of rare earth elements in refractory inclusions from the Ningquiang meteorite: Origin of positive anomalies in Ce, Eu, and Yb. *Geochim. Cosmochim. Acta* **75**, 3358-3384.

Huss, G. R., Meyer, B. S., Srinivasan, G., Goswami, J. N., Sahijpal, S. (2009) Stellar sources of the short-lived radionuclides in the early solar system. *Geochim. Cosmochim. Acta* **73**, 4922-4945.

Hoppe, P., Goswami, J. N., Krähenbühl, U. and Marti, K. (2001) Boron in chondrules. *Meteorit. Planet. Sci.* **36**, 1331-1343.

Imae, N. and Kojima, H. (2000) Sulfide textures of a unique CO3-chondrite (Y-82094) and its petrogenesis. *Antarctic Meteorite Research* **13**, 55–64.

Imai, N., Terashima, S., Itoh, S., and Ando, A. (1995) Compilation of analytical data for minor and trace elements in seventeen GSJ geochemical reference samples, "igneous rock series". *Geostandard Newslett.* **19**, 135-213.

Ireland, T. R. (1988) Correlated morphological, chemical, and isotopic characteristics of hibonites from the Murchison carbonaceous chondrite. *Geochim. Cosmochim. Acta* **52**, 2827-2839.

Ito, M. and Messenger, S. (2016) Rare earth element measurements and mapping of minerals in the Allende CAI, 7R19-1, by NanoSIMS ion microprobe. *Meteorit. Planet. Sci.* **51**, 818-832.

Ivanova, M. A., Kononkova, N. N., Krot, A. N., Greenwood, R. C., Franchi, I. A., Verchovsky, A. B., Trieloff, M., Korochantseva, E. V. and Brandstätter, F. (2008) The Isheyevo meteorite: Mineralogy, petrology, bulk chemistry, oxygen, nitrogen, carbon isotopic compositions, and ^{40}Ar-^{39}Ar ages. *Meteorit. Planet. Sci.* **43**, 915-940.

Jacob, D, E. (2006) High sensitivity analysis of trace element-poor geological reference glasses by Laser Ablation-Inductively Coupled Plasma-Mass Spectrometry (LA-ICP-MS). *Geostand. Geoanal. Res.* **30**, 221-235.

Jacobsen, B., Yin, Q. –Z., Moynier, F., Amelin, Y., Krot, A. N., Nagashima, K., Hutcheon, I. D. and Palme, H. (2008) ^{26}Al–^{26}Mg and ^{207}Pb–^{206}Pb systematics of Allende CAIs: Canonical solar initial ^{26}Al/^{27}Al ratio reinstated. *Earth Planet. Sci. Lett.* **272**, 353-364.

Jacquet, E., Alard, O. and Gounelle, M. (2012) Chondrule trace element geochemistry at the mineral scale. *Meteorit. Planet. Sci.* **47**, 1695-1714.

Jochum, K, P., Willbold, M., Raczek, I., Stoll, B. and Herwig, K. (2005) Chemical characterization of the USGS reference glasses GSA-1G, GSC-1G, GSD-1G, GSE-

1G, BCR-2G, BHVO-2G and BIR-1G using EPMA, ID-TIMS, ID-ICP-MS and LA-ICP-MS. *Geostand. Geoanal. Res.* **29**, 285-302.

Jochum, K, P., Weis, U., Stoll, B., Kuzmin, D., Yang, Q., Raczek, I., Jacob, D, E., Stracke, A., Birbaum, K., Frick, D, A., Günther, D. and Enzweiler, J. (2011) Determination of reference values for NIST SRM 610-617 glasses following ISO guidelines. *Geostand. Geoanal. Res.* **35**, 397-429.

Johnson, B. C., Minton, D. A, Melosh, H. J. and Zuber, M. T. (2015) Impact jetting as the origin of chondrules

Jones, R. H. and Layne, G. D. (1997) Minor and trace element partitioning between pyroxene and melt in rapidly cooled chondrules. *Am. Mineral.* **82** 534–545.

Jones R. H. (2012) Petrographic constraints on the diversity of chondrule reservoirs in the protoplanetary disk. *Meteorit. Planet. Sci.* **47**, 1176-1190.

Joswiak, D. J., Nakashima, D., Brownlee, D. E., Matrajt, G., Ushikubo, T., Kita, N. T., Messenger, S. and Ito, M. (2014) Terminal particle from Stardust track 130: Probable Al-rich chondrule fragment from comet Wild 2. *Geochim. Cosmochim. Acta* **144**, 277-298.

Kamata, Y., Koyama, K., Tsuboi, Y. and Yamauchi, S. (1997) X-Ray Analysis of the ρ Ophiuchi Dark Cloud with ASCA: Source Identification, X-Ray Spectra, and Temporal Variability. *Publ. Astron. Soc. Japan.* **49**, 461-470.

Kasemann S., Meixner A., Rocholl A., Vennemann T., Rosner M., Schmitt A. K. and Wiedenbeck M. (2001) Boron and oxygen isotope composition of certified reference materials NIST SRM 610/612 and reference materials JB-2 and JR-2. *Geostan. Newslett. J. Geostan. Geoanal.* **25**, 405–416.

Kasemann S. A., Jeffcoate, A. B. and Elliott, T. (2005) Lithium isotope composition of basalt glass reference material. *Anal. Chem.* **77**, 5251-5257.

Kimura, M., Goresy, A. E., Palme, H. and Zinner, E. (1992) Ca-, Al-rich inclusions in the unique chondrite ALH85085: Petrology, chemistry, and isotopic compositions.

Geochim. Cosmochim. Acta **57**, 2329-2359.

Kimura, M., Grossman, J. N. and Weisberg, M. K. (2008) Fe-Ni metal in primitive chondrites: Indicators of classification and metamorphic conditions for ordinary and CO chondrites. *Meteorit. Planet. Sci.* **43**, 1181-1177.

Kimura, M., Barrat, J. A., Weisberg, M. K., Imae, N., Yamaguchi, A. and Kohima, H. (2014) Petrology and bulk chemistry of Yamato-82094, a new type of carbonaceous chondrite. *Meteorit. Planet. Sci.* **49**, 346-357.

Kita, N. and Ushikubo, T. (2012) Evolution of protoplanetary disk inferred from ^{26}Al chronology of individual chondrules. *Meteorit. Planet. Sci.* **47**, 1108-1119.

Kita, N., Yin, Q. –Z., MacPherson, J. G., Ushikubo, T, Jacobsen, B., Nagashima, K., Kurahashi, E., Krot, A. N. and Jacobesen, S. B. (2013) ^{26}Al-^{26}Mg isotope systematics of the first solids in the early solar system. *Meteorit. Planet. Sci.* **48**, 1383–1400.

Kita, N., Tenner, T. J., Ushikubo, T., Hertwig, A., Chaumard, N., Defouilloy, C., Nakashima, D., Rudraswami, N. G., Weisberg, M. K., Kimura, M., Nagahara, H. and Bischoff, A. (2016) Chondrule oxygen isotope systematics among different chondrite groups: Variety of isotope reservoirs in the protoplanetary disk. *Meteorit. Planet. Sci.* **79**. #6378.

Kööp, L., Davis, A. M., Nakashima, D., Park, C., Krot, A. N., Nagashima, K., Tenner, T. J., Heck, P. R. and Kita, N. (2016) A link between oxygen, calcium and titanium isotopes in ^{26}Al-poor hibonite-rich CAIs from Murchison and implications for the heterogeneity of dust reservoirs in the solar nebula. *Geochim. Cosmochim. Acta* **189**, 70-95.

Kööp, L., Nakashima, D., Heck, P, R., Kita, N. T., Tenner, T. J., Krot, A. N., Nagashima, K., Park, C., and Davis, A. M. (2018) A multielement isotopic study of refractory FUN and F CAIs: Mass-dependent and mass independent isotope effects. *Geochim. Cosmochim. Acta* **221**, 296-317.

Korschinek, G., Bergmaier, A., Faestermann, T., Gerstmann, U. C., Knie, K., Rugel, G., Wallner, A., Dillmann, I., Dollinger, G., Lierse von Gostomski, Ch., Kossert, K., Maiti, M., Poutivtsev, M. and Remmert, A. (2010) A new value for the half-life of ^{10}Be by Heavy-Ion Elastic Recoil Detection and liquid scintillation counting. *Nucl. Instrum. Methods Phys. Res. B* **268**, 187-191.

Krot, A. N., Scott, E. R. D. and Zolensky, M. E. (1995) Mineral and chemical modification of components in CV3 chondrites: Nebular or asteroidal processing? *Meteoritics*, **30**, 748-775.

Krot, A. N., Meibom, A., Weisberg, M. K. and Keil, K. (2002) The CR chondrite clan: Implications for early solar system processes. *Meteorit. Planet. Sci.* **37**, 1451-1490.

Krot, A. N., Fagan, T. J., Keli, K., McKeegan, K. D., Sahijpal, S., Hutcheon, I., Petaev, M. I., and Yurimoto, H. (2004) Ca, Al-rich inclusions, amoeboid olivine aggregates, and Al-rich chondrules from the unique carbonaceous chondrite Acfer 094: I. Mineralogy and petrology. *Geochim. Cosmochim. Acta* **68**, 2167-2184.

Krot, A. N., Amelin, Y., Cassen, P. and Meibom, A. (2005) Young chondrules in CB chondrites from a giant impact in the early Solar System. *Nature* **436**, 989–992.

Krot, A. N., Nagashima, K., Bizzarro, M., Huss, G. R., Davis, A. M., Meyer, B. S. and Ulyanov, A. A. (2008a) Multiple Generations of Refractory Inclusions in the Metal-Rich Carbonaceous Chondrites Acfer 182/214 and Isheyevo. *Astrophys. J.* **672**, 713-721.

Krot, A. N., Ulyanov, A. A. and Ivanova, M. A. (2008b) Refractory inclusions in the CH/CB-like carbonaceous chondrite Isheyevo: I. Mineralogy and petrography. *Meteorit. Planet. Sci.* **43**, 1531-1550.

Krot, A. N., Amelin, Y., Bland, P., Ciesla, F. J., Connelly, J., Davis, A. M., Huss, G. R., Hutcheon, I. D., Makide, K., Nagashima, K., Nyquist, L. E., Russell, S. S., Scott, E. R. D., Thrane, K., Yurimoto, H. and Yin, Q.-Z. (2009) Origin and chronology of chondritic components: A review. *Geochim. Cosmochim. Acta* **73**, 4963-4997.

Krot, A. N., Nagashima, K., Yoshitake, M. and Yurimoto, H. (2010) Oxygen isotopic compositions of chondrules from the metal-rich chondrites Isheyevo (CH/CB_b), MAC 02675 (CB_b) and QUE 94627 (CB_b). *Geochim. Cosmochim. Acta* **74**, 2190-2211.

Krot, A. N., Makide, K., Nagashima, Huss, G. R., Ogliore, R. C., Ciesla, F. J., Yang, L., Hellebrand, E. and Gaidos, E. (2012a) Heterogeneous distribution of ^{26}Al at the birth of the solar system: Evidence from refractory grains and inclusions. *Meteorit. Planet. Sci.* **47**, 1948-1979.

Krot, A. N., Nagashima, K. and Petaev, M. I. (2012b) Isotopically uniform, ^{16}O-depleted calcium, aluminum-rich inclusions in CH and CB carbonaceous chondrites. *Geochim. Cosmochim. Acta* **83**, 159-178.

Krot, A. N., Nagashima, K., Wasserburg, G. J., Huss, G. R., Papanastassiou, D., Davis, A. M., Hutcheon, I. D. and Bizzarro, M. (2014) Calcium-aluminum-rich inclusions with fractionation and unknown nuclear effects (FUN CAIs): I. Mineralogy, petrology, and oxygen isotopic compositions. *Geochim. Cosmochim. Acta* **145**, 206-247.

Krot, A. N., Nagashima, K., van Kooten, E. M. M. and Bizzarro, M. (2017) High-temperature rims around calcium–aluminum-rich inclusions from the CR, CB and CH carbonaceous chondrites. *Geochim. Cosmochim. Acta* **201**, 155-184.

Larsen, K. K., Trinquier, A., Paton, C., Schiller, M., Qielandt, D., Ivanova, M. A., Connelly, J. N., Nordlund, Å., Krot, A. N. and Bizzarro, M. (2011) Evidence for Magnesium Isotope Heterogeneity in the Solar Protoplanetary Disk. *Astrophys. J.* **735**, L37 (7pp).

LaTourrettea, T. and Wasserbug, G. J. (1998) Mg diffusion in anorthite: Implications for the formation of early solar system planetesimals. *Earth Planet. Sci. Lett.* **158**, 91-108.

Lauretta, D. S. and Lodders, K. (1997) The cosmochemical behavior of beryllium and

boron. *Earth Planet. Sci. Lett.* **146**, 315-327.

Lee, T., Shu, F. H., Shang, H., Glassgold, A. E. and Rehm, K. E. (1998) Protostellar cosmic rays and extinct radioactivities in meteorites. *Astrophys. J.* **506**, 898-912.

Libourel, G., Krot, A. N. and Tissandier, L. (2006) Role of gas-melt interaction during chondrule formation. *Earth Planet. Sci. Lett.* **251**, 232-240.

Liebhart, A., Güdel, M., Skinner, S. L. and Green, J. (2014) X-ray emission from an FU Orionis star in early outburst: HBC 722. *A&A*. **570**, L11.

Liu, M.-C., McKeegan, K. D., Goswami, J. N., Marhas, K. K., Sahijpal, S., Ireland, T. R. and Davis, A. M. (2009) Isotopic records in CM hibonites: Implications for timescales of mixing of isotope reservoirs in the solar nebula. *Geochim. Cosmochim. Acta* **73**, 5051-5079.

Liu, M.-C., Nittler, L. R., Alexander, C. M. O. and Lee, T. (2010) Lithium-beryllium-boron isotopic compositions in meteoritic hibonite: implications for origin of ^{10}Be and early solar system irradiation. *Astrophys. J.* **719**, L99-L103.

Liu, M.-C., Han, J. and Brearley, A. (2017) The boron isotopic ratios of a fine-grained inclusion from the Allan Hills 77307 chondrite (CO3.0) (abstract). *Meteorit. Planet. Sci.* **80**. #6291.

Liu, M.-C. and Chaussidon, M. (2018) The cosmochemistry of boron isotopes. Advances in isotope geochemistry. Springer, Germany, pp. 273-289.

Lodders, K. (2003) Solar system abundances and condensation temperatures of the elements. *Astrophys. J.* **591**, 1220-1247.

Lodders, K. and Palme, H. (2009) Solar system elemental abundance in 2009 (abstract). *Meteorit. Planet. Sci.* **72**. #5154.

MacPherson, G. J., Huss, G. R. and Davis, A. M. (2003) Extinct ^{10}Be in type A Calcium-Aluminum-rich inclusions from CV chondrites. *Geochim. Cosmochim. Acta* **67**, 3165-3179.

MacPherson, G. J. Calcium-Aluminum-rich inclusions in chondritic meteorites. (2014)

In Meteorites and Cosmochemical Processes, Vol. 1: Treatise on Geochemistry 2nd edition. Elsevier, Oxford, pp. 139-179.

McKeegan, K. D., Chaussidon, M. and Robert, F. (2000) Incorporation of short-lived ^{10}Be in a Calcium-Aluminum-rich inclusion from the Allende meteorite. *Science* **289**, 1334-1337.

Matzel, J. E. P., Ishii, H. A., Joswiak, D., Hutcheon, I. D., Bradley, J. P., Brownlee, D., Weber, P. K., Teslich, N., Matrajt, G., McKeegan, K. D. and MacPherson, G. J. (2010) Constraints on the formation age of cometary material from the NASA stardust mission. *Science* **328**, 483-486.

McKeegan, K. D., Kallio, A. P. A., Heber, V. S., Jarzebinski, G., Mao, P. H., Coath, C. D., Kunihiro, T., Wiens, R. C., Nordholt, J. E., Moses Jr, R. W., Reisenfeld, D. B., Jurexicz, A. J. G., and Burnett, D. S. (2011) The Oxygen Isotopic Composition of the Sun Inferred from Captured Solar Wind. *Science* **332**, 1528-1532.

Murty, S. V. S., Mahajan, R. R. and Bartoschewitz, R. (2007) Nitrogen in Sayh al Uhaymir 290 (abstract). *Meteorit. Planet. Sci.* **70**. #5012.

Nagashima, K., Krot, A. N. and Komatsu, M. (2017) ^{26}Al–^{26}Mg systematics in chondrules from Kaba and Yamato 980145 CV3 carbonaceous chondrites. *Geochim. Cosmochim. Acta* **201**, 303-319.

Nakamura, T., Noguchi, T., Tsuchiyama, A., Ushikubo, T., Kita, N. T., Valley, J. W., Zolensky, M. E., Kakazu, Y., Sakamoto, K., Mashio, E., Uesugi, K. and Nakano, T. (2008) Chondrulelike Objects in Short-Period Comet 81P/Wild 2. *Science* **321**, 1664-1667.

Nishiizumi, K. (2004) Preparation of ^{26}Al AMS standards. *Nucl. Instrum. Methods. Phys. Res. B.* **223-224**, 388-392.

Olsen, M. B., Wielandt, D., Schiller, M., van Kooten, E. M. M. E. and Bizzarro, M. (2016) Magnesium and 54Cr isotope compositions of carbonaceous chondrite chondrules Insights into early disk processes. *Geochim. Cosmochim. Acta* **191**, 118-138.

Park, C., Nagashima, K., Krot, A. N., Huss, G. R., Davis, A. M. and Bizzaro, M. (2017) Calcium-aluminum-rich inclusions with fractionation and unidentified nuclear effects (FUN CAIs): II. Heterogeneities of magnesium isotopes and ^{26}Al in the early solar system inferred from in situ high-precision magnesium-isotope measurements. *Geochim. Cosmochim. Acta* **201**, 6-24.

Preibisch, T., Kim, Y. -C., Favata, F., Feigelson, E. D., Flaccomio, E., Getman, K., Micela, G., Sciortino, S., Stassun, K., Stelzer, B. and Zinnecker, H. (2005) The origin of T Tauri x-ray emission: New insights from the chandra orion ultradeep project. *Astrophys. J.* **160**, 401-422.

Ramaty, R., Kozlovsky, B. and Lingenfelter, R. E. (1996) Light isotopes, extinct radioisotopes, and gamma-ray lines from low-energy cosmic-ray interactions. *Astrophys. J.* **456**, 525-540.

Reames, D. V. (1999) Particle acceleration at the Sun and in the heliosphere. *Space Sci. Rev*. **90**, 413–491.

Reed, S. J. B. (1983) Secondary-ion yields of rare earths. Int. J. Mass Spectrom. Ion Processes. **54**, 31-40.

Rubin, A. Petrologic, geochemical and experimental constraints on models of chondrule formation. (2000) *Earth. Sci. Rev.* **50**, 3-27.

Russell, S. S., Huss, G. R., Fahey, A. J., Greenwood, R. C., Hutchison, R. and Wasserburg, G. J. (1998) An isotopic and petrologic study of calcium-aluminum-rich inclusions from CO3 meteorites. *Geochim. Cosmochim. Acta* **62**, 689-714.

Ryerson, F. and McKeegan, K. (1994) Determination of oxygen self-diffusion in åkermanite, anorthite, diopside, and spinel: Implications for oxygen isotopic anomalies and the thermal histories of Ca-Al-rich inclusions. *Geochim. Cosmochim. Acta* **58**, 3713-3734.

Sano, Y., Terada, K. and Fukuoka, T. (2002) High mass resolution ion microprobe analysis of rare earth elements in silicate glass, apatite and zircon: lack of matrix

dependency. *Chem. Geol.* **184**, 217-230.

Sahijpal, S. and Goswami, J. N. (1998) Refractory phases in primitive meteorites devoid of ^{26}Al and ^{41}Ca: Representative samples of first solar system solids? *Astrophys. J.* **509**, L137-L140.

Sahijpal, S., Goswami, J. N. and Davis, A. M. (2000) Mg, Ti and Ca isotopic compositions and refractory trace element abundances in hibonite from CM and CV meteorites: Implications for early solar system processes. *Geochim. Cosmochim. Acta* **64**, 1989–2005**.**

Scott, E. R. D., Keil, K., and Stöffler, D. (1992) Shock metamorphism of carbonaceous chondrites. *Geochim. Cosmochim. Acta* **56**, 4281–4293**.**

Scott, E. R. D. and Krot, A. N. (2014) Chondrites and their components. *In Meteorites and Cosmochemical Processes, Vol. 1: Treatise on Geochemistry 2nd edition*. Elsevier, Oxford, pp. 65-137.

Schiller, M., Connelly, J. N. Glad, A. C., Mikouchi, T. and Bizzarro, M. (2015) Early accretion of protoplanets inferred from a reduced inner solar system ^{26}Al inventory. *Earth Planet. Sci. Lett.* **420**, 45-54.

Schulz, N. S. (2012) The formation and Early Evolution of Stars. *From dust to Stars and planets 2nd edition*, Astronomy and Astrophysics library, Springer, Germany.

Seitz, H. -M, Brey, G. P., Zipfel, J., Ott, U., Weyer, S., Durali, S. and Weinbruch, S. (2007) Lithium isotope composition of ordinary and carbonaceous chondrites, and differentiated planetary bodies: Bulk solar system and solar reservoirs. *Earth Planet. Sci. Lett.* **260**, 582-596.

Shen, J. J.-S. and Lee, T. (2003) ^{138}La anomaly in the early solar system. *Astrophys. J.* **596**, L109-L112.

Shu, F. H. (1977) Self-similar collapse of isothermal spheres and star formation. *Astrophys. J.* **214**, 488-497.

Shu, F. H., Shang, H., Glassgold, A. E. and Lee, T. (1997) X-rays and fluctuating x-Winds

from protostars. *Science* **277**, 1475-1479.

Skinner, S. L., Sokal, K. R., Güdel, M. and Briggs, K. R. (2009) X-ray emission from the FU orionis star V1735 cygni. *Astrophys. J.* **696**, 766-774.

Simon, S. B., Davis, A. M. and Grossman, L. (1999) Origin of compact type A refractory inclusions from CV3 carbonaceous chondrites. *Geochim. Cosmochim. Acta* **63**, 1233-1248.

Simon, S. B., Davis, A. M., Grossman, L. and McKeegan, K. D. (2002) A hibonite-corundum inclusion from Murchison: A first-generation condensate from the solar nebula. *Meteorit. Planet. Sci.* **37**, 533-548.

Simon, S. B. and Grossman, L. (2015) Refractory inclusions in the pristine carbonaceous chondrites DOM 08004 and DOM 08006. *Meteorit. Planet. Sci.* **50**, 1032-1049.

Sossi, P. A., Moynier, F., Chaussidon, M., Villeneuve, J., Kato, C. and Gounelle, M. (2017) Early solar system irradiation quantified by linked vanadium and beryllium isotope variations in meteorites. *Nat. Astron.* **1**, 0055.

Soulie, C., Libourel, G. and Tissandier, L. (2017) Olivine dissolution in molten silicates: An experimental study with application to chondrule formation. *Meteorit. Planet. Sci.* **52**, 225-250.

Srinivasan, G., Goswami, J. N. and Bhandari, N. (1999) ^{26}Al in eucrite Piplia Kalan: Plausible heat source and formation chronology. *Science* **284**, 1348-1350.

Srinivasan, G. and Chaussidon, M. (2013) Constraints on ^{10}Be and ^{41}Ca distribution in the early solar system from ^{26}Al and ^{10}Be studies of Efremovka CAIs. *Earth Planet. Sci. Lett.* **374**, 11-23.

Steele, R. C. J., Heber, V. S., McKeegan, K. D. (2017) Matrix effects on the relative sensitivity factors for manganese and chromium during ion microprobe analysis of carbonate: Implications for early Solar System chronology. *Geochim. Cosmochim. Acta* **201**, 245-259.

Sugiura, N., Shuzou, Y. and Ulyanov, A. (2001) Beryllium-boron and aluminum-

magnesium chronology of calcium-aluminum-rich inclusions in CV chondrites. *Meteorit. Planet. Sci.* **36**, 1397-1408.

Sugiura, N. (2001) Boron isotopic compositions in chondrules: Anorthite-rich chondrules in the Yamato 82094 (abstract). *Lunar Panet. Sci.* **32**. #1277.

Sugiura, N., Ichimura, K., Fujiya, W. and Takahata, N. (2010) Mn/Cr relative sensitivity factors for synthetic calcium carbonate measured with a NanoSIMS ion microprobe. *Geochem. J.* **44**, 11-16.

Tatischeff, V., Duprat, J. and de Séréville, N. (2014) Light-element nucleosynthesis in a molecular cloud interacting with a supernova remnant and the origin of beryllium-10 in the protosolar nebula. *Astrophys. J.* **796**, 124 (20pp).

Telleschi, A., Güdel, M., Briggs, K. R. and Palla, F. (2007) X-ray emission from T Tauri stars and the role of accretion: inferences from the XMM-Newton extended survey of the Taurus molecular cloud. *A&A*. **468**, 425-442.

Tenner, T. J., Nakashima, D., Ushikubo, T., Kita, N. T. and Weisberg, M. K. (2015) Oxygen isotope ratios of FeO-poor chondrules in CR3 chondrites: Influence of dust enrichment and H_2O during chondrule formation. *Geochim. Cosmochim. Acta* **148**, 228-250.

Ushikubo, T., Tenner, T. J., Hiyagon, H. and Kita, N. T. (2017) A long duration of the ^{16}O-rich reservoir in the solar nebula, as recorded in fine-grained refractory inclusions from the least metamorphosed carbonaceous chondrites. *Geochim. Cosmochim. Acta* **201**, 103-122.

Van Kooten, E. M. M. E., Wielandt, D., Schiller, M., Nagashima, K., Thomen, A., Larsen, K. K., Olsen, M. B., Nordlund, Å., Krot, A. N. and Bizzarro, M. (2016) Isotopic evidence for primordial molecular cloud material in metal-rich carbonaceous chondrites. *PNAS.* **113**, 2011-2016.

Wasserburg, G. J., Busso, M., Gallino, R. and Nollett, K. M. (2006) Short-lived nuclei in the early solar system: Possible AGB sources. *Nuclear Physics*. **777**, 5-69.

Weber, D., Zinner, E. and Bischoff, A. (1995) Trace element abundances and magnesium, calcium, and titanium isotopic compositions of grossite-containing inclusions from the carbonaceous chondrite Acfer 182. *Geochim. Cosmochim. Acta* **59**, 803-823.

Wielandt, D., Nagashima, K., Krot, A. N. and Huss, G. R. (2012) Evidence for multiple sources of ^{10}Be in the early solar system. *Astrophys. J.* **748**, L25 (7pp).

Winston, E., Megeath, S. T., Wolk, S. J., Hernandez, J., Gutermuth, R., Muzerolle, J, Hora, J. L., Cover, K., Allen, L. E., Spitzbart, B., Peterson, D., Myers, P. and Fazio, G. G. (2009) A spectroscopic study of young stellar objects in the serpens cloud core and NGC 1333. *Astrophys. J.* **137**, 4777-4794.

Wood, J. A. (2004) Formation of chondritic refractory inclusions: the astrophysical setting. *Geochim. Cosmochim. Acta* **68**, 4007-4021.

Woosley, S. E., Hartmann, D. H., Hoffman, R. D. and Haxton, W. C. (1990) The ν-process. *Astrophys. J.* **356**, 272-301.

Yanai, K. and Kojima, H. (1987) *Petrographic catalog of the Antarctic meteorites*. Tokyo: NIPR.

Yiou, F., Baril, M., de Citres, D., Fontes, P., Gradsztajn, E. and Bernas, R. (1968) Mass-spectrometric measurement of lithium, beryllium, and boron isotopes produced in ^{16}O by high-energy protons, and some astrophysical implications. *Physical Review* **166**, 968-974.

Yokoyama, T. D., Suzuki, T., Kon, Y. and Hirata, T. (2011) Determinations of rare earth element abundance and U-Pb age of zircon using multispot laser ablation-inductively coupled plasma mass spectrometry. *Anal. Chem.* **83**, 8892-8899.

Zhai, M., Nakamura, E., Shaw, D. M. and Nakano, T. (1996) Boron isotope ratios in meteorites and lunar rocks. *Geochim. Cosmochim. Acta* **23**, 4877-4881.

Zhang, A. and Hsu, W. (2009) Refractory inclusions and aluminum-rich chondrules in Sayh al Uhaymir 290 CH chondrite: Petrography and mineralogy. *Meteorit. Planet. Sci.* **44**, 787-804.

Zhang, Y., Ni, H. and Chen, Y. (2010) Diffusion data in silicate melts. *Rev. Mineral & Geochem* **72**, 311-408.